THE UNIVERSITY OF CHICAGO

LARGE-SCALE SYNTHESIS OF TWO-DIMENSIONAL POLYMERS AND THEIR MEMBRANE APPLICATIONS

A DISSERTATION SUBMITTED TO
THE FACULTY OF THE DIVISION OF THE PHYSICAL SCIENCES
IN CANDIDACY FOR THE DEGREE OF
DOCTOR OF PHILOSOPHY

DEPARTMENT OF CHEMISTRY

BY
BAORUI CHENG

CHICAGO, ILLINOIS
AUGUST 2023

To my family and friends

Table of Contents

LIST OF FIGURES

LIST OF TABLES

ACKNOWLEDGEMENTS

Even in my wildest dreams, I could never have imagined achieving a Ph.D. without the unwavering support and invaluable guidance from all those who have generously helped me along my journey for graduate school. Frist and foremost, I would like to thank my advisor Prof. Jiwoong Park. Jiwoong has been a great mentor of me for not only research but also all aspects of life. His passion for science and relentless pursuit of fundamentals have always been an inspiration for me. I truly appreciate his open mind and willingness to try new things. Without his support and guidance, none of my accomplishments in the past six years would be possible.

Graduate school can sometimes be incredibly challenging and stressful for many, but thanks to Dr. Yu Zhong, mine journey was mostly filled with joy and excitement. As my mentor, Yu has taught me the correct way for research as well as the right mentality at times of difficulty. His encouragements always come just when I need them, and his patience never runs out. Yu has also been a great friend outside the lab. I can’t remember how many times I complained to him or how many gossips we shared together. I will always be grateful for your mentorship and friendship.

The Park group has been a fun place for me since the day I joined, and everyone I had the honor to work with were friendly, fun, and extremely talented. To the Movie Night Crew, Fauzia, Kim, Josh, and Michelle, you are my first friends in the US to share “juicy” stories. Our movies, games and adventures were the few colorful moments in my boring grad school life. Thank you for bringing joy to my Chicago time! To Hui, thank you for all the help during my job seeking processes, and more importantly, thank you for the Mahjong set! To Ce and Hanyu, thank you for all the cooking you have done for me and Dan. To Chibeom, Joonki, Jae-Ung and Andy, you were there when I first joined group, and I thank you for all the support and help you offered to the then most junior member in the group, primarily in the form of accepting me to your postdoc lunch parties. To Andrew, Tomojit, Jong Hoon, and Jaehyung, I owe you all a huge thank you because of all the time you wasted on our random conversations (that's why Andrew is here with all the postdocs). To the rest of the group that I had the honor to overlap with, Kan-Heng, Saien, Preeti, Myungjae, Mengyu, Gustavo, Dong Hyup, Hyojin, Jingyuan, Yuanke, Zehra, and Jack, a heartfelt thank you goes to you all for the time and numerous events we shared together.

I would like to thank Prof. John Anderson and Prof. Chong Liu for serving as my dissertation committee members. I am sincerely grateful for your time commitment and insightful suggestions and comments to this dissertation. In addition, I would like to send my sincere gratitude to my collaborators: Prof. John Anderson, Prof. David Muller, Prof. Steven Sibener, and Prof. Suriyanarayanan Vaikuntanathan. It's been a great honor to be able to work with those talented and revered scientists, and I have learnt a lot from them.

Lastly, I would like to thank my family and friends for their support and companion. Ananth and Ram, my soccer pals, thank you for dragging me out of lab and trying to keep my body and mind in a healthy condition. Bo and Xiangyu, it was a wonderful experience to reunite in the US after high school. I was extremely lucky to have your companion in this completely strange place. To my parents, there is no way I can thank you enough for everything you have done for me. Even though we are separated by 13 time zones amidst the pandemic, your understanding and support still help me move forward every single day. To my beloved wife, Dan, without your companion, I would have no chance completing this journey alone. It is never easy for two people to crowd in a studio living on sub-minimum wage, but you have only brought laughter and happiness to our life. Thank you for travelling across the world to my companion, and for accompanying me through all the ups and downs in life.

ABSTRACT

Two-dimensional polymers (2DPs) are a class of two-dimensional (2D) materials that combine atomic thinness and molecular functionality. Like all 2D materials, 2DPs have an anisotropic structure where molecular moieties are connected by chemical bonds in-plane but loosely bounded out-of-plane through van der Waals (vdW) forces, allowing 2DPs to be isolated as ultrathin monolayers. What distinguishes 2DPs from their inorganic counterparts are the molecular lattice constituents, which give rise to almost infinite varieties of 2DPs. Particularly, molecular lattice constituents often lead to an intrinsic porosity in 2DPs, making them ideal candidate for membrane-related applications. In this dissertation, we will investigate the large-scale synthesis of 2DPs and explore their application as a membrane for osmotic power generation. First, we will introduce an interfacial synthesis method for monolayer 2DPs up to inch-scale. This method is compatible with various 2DPs structures and chemistries. We will use this method to generate homogeneous monolayer 2DPs and investigate their structural and chemical properties. Using this approach, we will also demonstrate the capability of generating hybrid vdW heterostructures, from which large-scale electrical device arrays can be fabricated. Second, we will use our ultrathin nanoporous 2DPs as a permselective membrane for osmotic power generation. The chemical and structural versatility of 2DPs allow for a rational bottom-up design of a covalently linked 2DP membrane with proper pore size and functionalization that fall in the “Goldilocks” zone for osmotic power generation. The mechanics of short-range interaction-based permselectivity in our membrane is investigated using molecular dynamics simulations, and the unique mechanism is leveraged for ion-specific transport and gateable osmotic power generation. In the end, we propose several new directions for further improving the synthesis of 2DPs and expanding their applications.

Chapter 1: Introduction and Overview

1.1 2D Materials and Their "Organifization"

In this dissertation, we investigate the large-scale synthesis and applications of two-dimensional (2D) materials, particularly the organic ones. Since the discovery of graphene[1], the first 2D material that consists of a single layer of hexagonal carbon lattice exfoliated from graphite nearly two decades ago, a multitude of researchers have devoted their entire careers to the study of 2D materials. To date, over a few dozen different 2D materials have been identified, with countless others still awaiting isolation or synthesis[2,3]. What began as a playground for physicists to explore exotic low-dimensional physics soon captured the attention of materials scientists and chemists, who began exploring various techniques for synthesizing 2D materials from the bottom up[4]. Among these techniques, chemical vapor deposition (CVD) emerged as the most prominent, enabling the growth of high-quality, large-area 2D materials that have a range of potential applications[5,6].

It did not take long for scientists to realize that the dangling bond-free surfaces of 2D materials make them ideal for materials integration without the constraint of lattice matching[7]. As different 2D layers are held together through van der Waals (vdW) forces, their heterostructures are referred to as vdW heterostructures. With a library of 2D materials covering insulators, metals, and semiconductors, and their extraordinary electronic properties, making atomically thin circuitry has been the holy grail of the 2D field for very long time and will continue to be so. As a result, much progress has been made in the integration of 2D materials, allowing for the fabrication of vdW heterostructures and lateral junctions with clean interfaces at large scales and with precise control over translational and rotational degrees of freedom[8–10]. Automatic integration systems have even been developed to streamline the process[8,11]. Recently, the moiré physics from vdW heterostructures has added another exciting aspect to 2D materials research[12], attracting again a multitude of researchers to devote their entire careers to studying the exotic physics in the 2D world.

Despite the many achievements and milestones in the field of 2D materials, our discussion so far has been limited to inorganic materials. The power of organic synthesis and the diversity of organic materials are evident in every aspect of modern society, with two of the most noticeable being modern medicine and plastics. In fact, even before the discovery of graphene, scientists were able to assemble a monolayer of organic molecules on metal surfaces[13], which could arguably be considered 2D materials before graphene. After the advent of graphene, the question

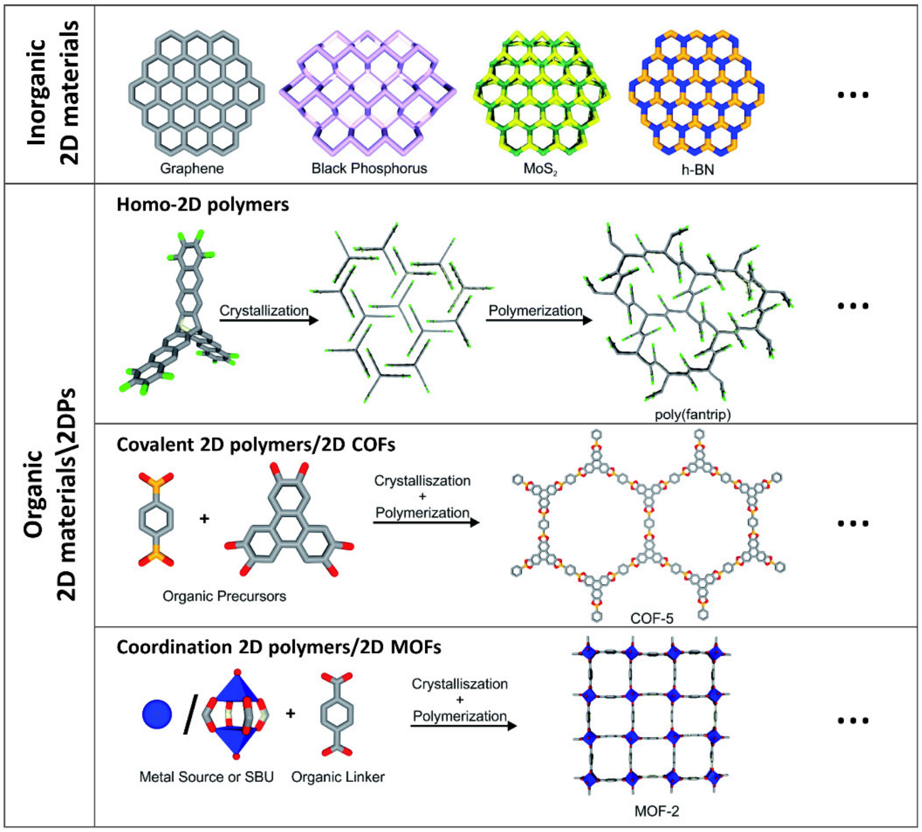

Figure 1.1 Different categories and types of 2D materials. Reproduced from Ref. 16.

for chemists was whether organic 2D materials could be synthesized and isolated in a similar manner to graphene, which is easily manipulable and does not require an ultra-high vacuum chamber. The answer was yes, and since the discovery of graphene, more organic 2D materials have been identified than inorganic ones[14,15], bringing great structural diversity and functionality to 2D materials research (Fig. 1.1)[16].

The rapid development of organic 2D materials benefited from the well-established reticular chemistry, which offers a wide range of molecular building blocks and linking strategies to create predetermined ordered frameworks[17–19] (Fig. 1.2). It is no surprise that with the proper geometry of molecular building blocks and suitable linkage, ordered 2D frameworks, also now known as 2D polymers (2DPs), can be synthesized through reticular chemistry[17,20]. Compared to

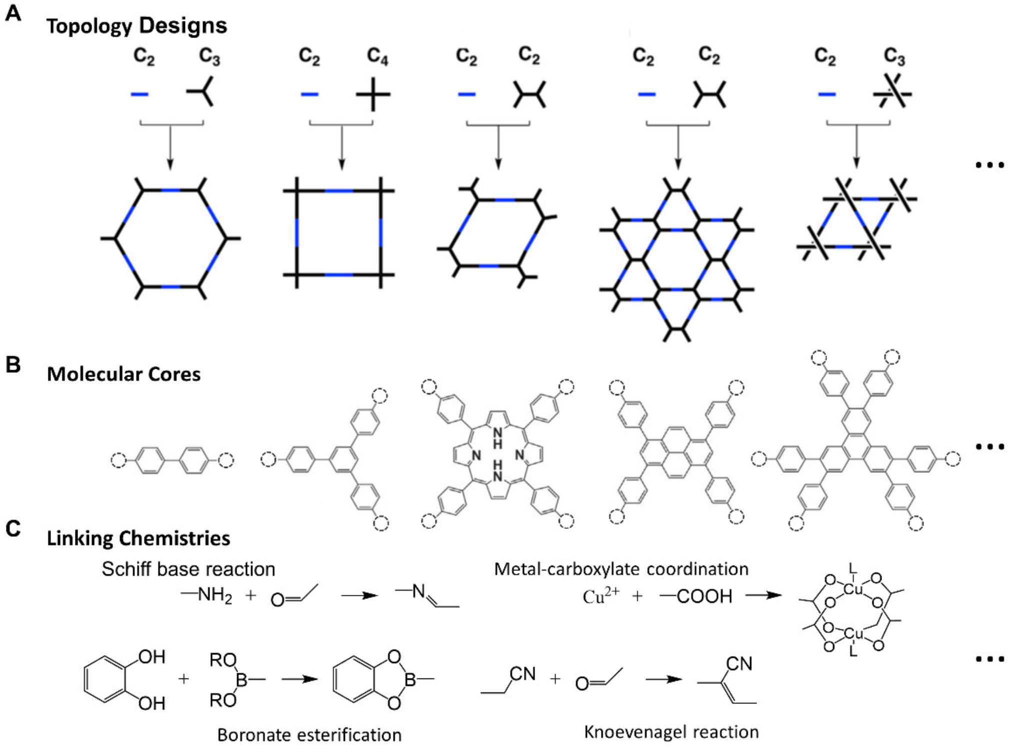

Figure 1.2 Reticular chemistry of organic 2d materials. **(A)** Topology designs of organic 2D materials. Reproduced from Ref. 18. **(B)** Examples of molecular building blocks for organic 2D materials with various molecular symmetries. **(C)** Examples of linkage chemistries for organic 2D materials synthesis.

inorganic ones, the composition and structure of organic 2D materials, especially 2D polymers, can be designed and controlled with greater versatility by combining various molecular precursors and linking chemistries. This level of control enables the realization of desired functions through molecular design for specific applications. Additionally, changing the lattice constituents from atoms to molecules results in a much larger lattice size, which allows for intrinsic porosity. This porosity opens up new opportunities in membrane-related applications such as gas separation and water desalination[21–26].

1.2 Functions and Applications of Organic 2D materials

Given the inspiration provided by their inorganic counterparts, it is not surprising that the early applications of organic 2D materials focused on their electronic properties[27–31]. In fact, the development of organic electronics significantly predates the discovery of 2D materials, with the hope of the solution-processable organic materials being a much more accessible alternative to the inorganic ones, and potentially with more versatile functionalities that can be tailored to specific applications[32,33]. More recently, improved synthetic techniques have led to increased interest in membrane applications of 2DPs[21,25]. With their 2D thinness and tunable nanoporous structures, 2DPs allow for superior permeation and on-demand membrane design compared to traditional inorganic and polymeric membranes[21,24,34]. As a result, 2DP-based membranes have shown great promises for various separation processes[22,25,34] as well as energy conversion and storage[16,35].

When organic materials are reduced to 2D, many of their interesting properties remain intact, but their conductivity usually decreases significantly as the planar arrangement of molecular moieties prohibits electron hopping through the $\pi - \pi$ stacking [28–30,36]. With the conventional

$\pi - \pi$ hopping no longer accessible, researchers turned to increasing electron delocalization within the 2D layer. To achieve this goal, many different strategies were devised, such as adopting highly conjugated monomers[27], optimizing linkage chemistry to maximize orbital overlapping[30], and utilizing host-guest interactions[37]. Within a decade, the design principles for high-conductivity 2DPs were established, resulting in the reporting of 2DPs with conductivity as high as 2500 S/cm^2 [38]. In addition, metallic transport and superconductivity were also realized in 2DPs, completing the picture of conductive 2DPs[38–40].

The electrical conductivity in 2DPs has then laid the foundation for many other applications, including electrocatalysis, chemical sensing, and energy storage[29,35,41]. Moreover, the versatile nature of 2DPs also allow them to be used to modulate the conducting behavior of other materials, providing molecular versatility to otherwise inert materials[42–45]. By combining molecular design with conductivity, the versatility of organic chemistry and easy accessibility of electricity can be leveraged to create customizable electronic devices for various applications.

However, it is important to note that in the context of conductivity-focused research, the morphology of the materials being studied is usually not 2D (i.e. few-layers and monolayers). Instead, powder, nanocrystals, and thick films ($\sim\mu m$) are often used[27,31,46]. Until very recently, the unique 2D nature of 2DPs was not fully exploited for their applications, largely due to the limited synthetic approaches for producing monolayer or few-layer 2DPs[14,47]. Nonetheless, with recent progress in 2DP synthesis, the potential of structurally diverse and chemically versatile 2D membranes is garnering attention, and their intrinsic porosity is particularly intriguing for many researchers[22,24–26].

Compared to bulk 3D porous materials, porous 2DPs possess atomic-level thickness, which allows for fast diffusion of species through the pores, enabling rapid and efficient interaction with the environment. In combination with the chemical versatility of reticular chemistry, this property creates numerous new opportunities. For example, when catalytic moieties are integrated into the structure, 2DPs can serve as excellent heterogeneous catalysts due to the completely exposed surface and easy access to the catalytic center[48].

As large-scale synthesis of 2DPs became available[47,49–53], these ultrathin porous materials have demonstrated great potential for membrane-related applications. For instance, precise design of the geometry, size, and functionality of nanopores in a 2DP membrane enables efficient and on-demand separation of similar and dissimilar molecules, and even ions[21,54]. With proper functionality and pore size, 2DP membrane may significantly boost the performance of molecular separation, water desalination and osmotic power generation.

With the advancements in monolayer/few-layer 2DP synthesis, it is now possible to integrate 2DPs with other inorganic 2D materials via vdW integration[42,55,56]. This integration allows the creation of hybrid vdW heterostructures, where the chemical versatility of 2DPs can be combined with the robustness and conductivity of inorganic 2D materials. 2DPs can sensitize the heterostructures and make them responsive to specific stimulants, such as chemicals, light, and heat[43,57,58]. Moreover, 2DPs can also potentially act as a surface modification to better interface inorganic 2D materials with various processes[59].

The on-demand chemical design and structural diversity of 2DPs provide unique properties and enable applications that are not accessible by other materials. When combined with the ultimate 2D thinness, the possibilities with 2DPs are unparalleled.

1.3 Challenges and Progresses in 2DP Synthesis

The synthesis of 2DPs differs significantly from that of the inorganic 2D materials. Following the isolation of graphene through graphite exfoliation, the production of large-scale monolayer graphene was achieved via chemical vapor deposition (CVD) on copper surfaces[60]. As additional inorganic 2D materials were identified, CVD remained the preferred and most effective method for their bottom-up synthesis, particularly at large scale[4–6,60].

In general, CVD relies on the heterogeneous nucleation and reaction of constituent atoms at the interface of a gas and a solid substrate. This process typically involves the decomposition of either gaseous or solid precursors to produce constituent atoms, which then react at the substrate surface to form the desired material. The thermal stability of inorganic 2D materials and decomposition of precursors into atomic constituents allow a large thermal budget for this type of synthesis, which is one of the key factors that makes CVD such an effective method for the synthesis of inorganic materials.

The synthesis of organic 2D materials, or 2DPs, however, is drastically different. To form a lattice of molecules and clusters, the integrity of the individual lattice constituent must be preserved, limiting the allowed temperature for synthesis. For most carbon-based organic molecules, the decomposition temperature is around 300 °C. In addition, 2DP structures, especially those with large intrinsic porosity, have a much lower bond density than their inorganic counterparts and are generally less thermally stable[61,62]. Therefore, synthesis of 2DPs must be done at relatively low temperature to maintain the integrity of constituent molecules/clusters and the synthesized 2DPs.

On top of the low thermal budget, 2DPs suffer from a lower anisotropy for in-plane and out-of-plane bonding. The out-of-plane $\pi - \pi$ stacking is usually strong enough to compete with the in-plane coordination or reversible covalent bonds, which can sometimes lead to preferential out-of-plane crystal growth[36,63–65]. Furthermore, the intrinsic porosity and rotatable bonds make 2DPs “soft”, rendering them more prone to interpenetration, bending and lattice frustration. All of these factors can lead to amorphousness and even break the 2D structure. As a result, growing 2DPs, especially in a monolayer, is an extremely challenging task.

Early synthetic efforts towards 2DPs were primarily focused on the identification of planar monomers that give rise to 2D layered structures and the linkage chemistries that generate robust bonding and facilitate electron transport[18,28,29,35]. Hydro/solvo-thermal methods and conventional solution synthesis have been the major approaches for these types of synthesis. The monomers typically consist of large, rigid, conjugated molecules of fused aromatic rings (Fig. 1.2). Proper selection of transition metal centers and organic linkers is crucial to ensure the formation of the desired 2D lattice and modulator molecules are often used to facilitate the 2D structure as well as improve the crystallinity[63–65]. While solution-based methods have been successful in generating powders and single crystals of layered 2DPs, they often fall short in generating strict monolayer of 2DPs without further exfoliation/processing (e.g. ultrasonication and mechanical exfoliation).

Significant progress has been made in the synthesis of monolayer/few-layer 2DPs with interfacial synthesis[14,66,67]. The intrinsic 2D nature of interfaces/surfaces provides an ideal guiding template for 2DP synthesis. Before the concept of 2DP was coined, monolayers of organic molecules were deposited on atomically flat metal terraces in ultra-high vacuum chambers, marking the early attempts of interfacial synthesis of 2DPs[13]. As the research of 2DPs gaining momentum, various interfacial methods have been developed, covering all the binary combination of gas, liquid, and solid, as well as immiscible liquid-liquid interfaces. Among those methods, Langmuir-Blodgett deposition that utilizes an air-water interface has attracted the most interests[49,52,53]. This method can generate large-scale monolayers of molecules from a sub-monolayer spreading by compressing the molecules at the air-water interface with a pair of barriers while closely monitoring the change in surface tension. However, the mechanical compression inevitably induces wrinkles and cracks[66,68,69], even though global surface tension is being monitored in real-time. Moreover, the reaction conditions accessible to a Langmuir-Blodgett deposition are limited to around room temperature to maintain a stable air-water interface, leading to limited linkage options and often poor crystallinity.

1.4 Dissertation Outline

In this dissertation, we will present our approaches towards the synthesis and application of 2DPs. In Chapter 2, we review the fundamental design and chemistry of 2DP synthesis and introduce several well-established synthetic techniques for 2DPs. After that, we briefly discuss the developing techniques that show potentials for future improvements. In Chapter 3, we present our unique method, namely laminar assembly polymerization (LAP), for wafer-scale monolayer 2DPs synthesis. The mechanics of this method are studied in detail with experimental support, and thorough characterization of the synthesized wafer-scale 2DPs are presented. In Chapter 4, fabrication of vdW heterostructures of 2DP/MoS_2 is demonstrated. Our transfer-based integration method enables programmable superlattices and non-perturbative device fabrication with them. We then move on to more application-related topics in Chapter 5, where we detail the design and synthesis of a 2D nanoporous membrane for osmotic power generation. The power generation experiment is conducted with a microfluidic membrane device, and the power generation performance is benchmarked with previous materials. We then use molecular dynamics simulation to understand the short-range interaction dominated ion selectivity in Chapter 6 and demonstrate the unique ion-specific selectivity and gated osmotic power generation. Finally in Chapter 7, we conclude this dissertation with a discussion on our ongoing efforts and future plans with 2DP synthesis and applications.

1.5 References

1. Novoselov, K. S. *et al.* Electric field in atomically thin carbon films. *Science* **306**, 666–669 (2004).
2. Ryu, B., Wang, L., Pu, H., Chan, M. K. Y. & Chen, J. Understanding, discovery, and synthesis of 2D materials enabled by machine learning. *Chem. Soc. Rev.* **51**, 1899–1925 (2022).
3. Mounet, N. *et al.* Two-dimensional materials from high-throughput computational exfoliation of experimentally known compounds. *Nat. Nanotechnol.* **13**, 246–252 (2018).
4. Lin, Z. *et al.* 2D materials advances: From large scale synthesis and controlled heterostructures to improved characterization techniques, defects and applications. *2D Mater.* **3**, 042001 (2016).
5. Kang, K. *et al.* High-mobility three-atom-thick semiconducting films with wafer-scale homogeneity. *Nature* **520**, 656–660 (2015).
6. Cai, Z., Liu, B., Zou, X. & Cheng, H. M. Chemical Vapor Deposition Growth and Applications of Two-Dimensional Materials and Their Heterostructures. *Chem. Rev.* **118**, 6091–6133 (2018).
7. Geim, A. K. & Grigorieva, I. V. Van der Waals heterostructures. *Nature* **499**, 419–425 (2013).
8. Mannix, A. J. *et al.* Robotic four-dimensional pixel assembly of van der Waals solids. *Nat. Nanotechnol.* **17**, 361–366 (2022).
9. Kang, K. *et al.* Layer-by-layer assembly of two-dimensional materials into wafer-scale heterostructures. *Nature* **550**, 229–233 (2017).
10. Castellanos-Gomez, A. *et al.* Van der Waals heterostructures. *Nat. Rev. Methods Prim.* **2**, 1–19 (2022).
11. Masubuchi, S. *et al.* Autonomous robotic searching and assembly of two-dimensional crystals to build van der Waals superlattices. *Nat. Commun.* **9**, 1–12 (2018).
12. Mak, K. F. & Shan, J. Semiconductor moiré materials. *Nat. Nanotechnol.* **17**, 686–695

(2022).

13. Forrest, S. R., Burrows, P. E., Haskal, E. I. & So, F. F. Ultrahigh-vacuum quasiepitaxial growth of model Van Der Waals thin films. II. Experiment. *Phys. Rev. B* **49**, 11309–11321 (1994).

14. Evans, A. M. *et al.* Two-Dimensional Polymers and Polymerizations. *Chem. Rev.* **122**, 442–564 (2022).

15. Wang, W. & Schlüter, A. D. Synthetic 2D Polymers: A Critical Perspective and a Look into the Future. *Macromol. Rapid Commun.* **40**, 1800719 (2019).

16. Schneemann, A. *et al.* 2D framework materials for energy applications. *Chemical Science* vol. 12 1600–1619 (2021).

17. Colson, J. W. & Dichtel, W. R. Rationally synthesized two-dimensional polymers. *Nat. Chem.* **5**, 453–465 (2013).

18. He, T., Geng, K. & Jiang, D. All sp2 carbon covalent organic frameworks. *Trends Chem.* **3**, 431–444 (2021).

19. Ockwig, N. W., Delgado-Friedrichs, O., O'Keeffe, M. & Yaghi, O. M. Reticular chemistry: Occurrence and taxonomy of nets and grammar for the design of frameworks. *Acc. Chem. Res.* **38**, 176–182 (2005).

20. Sakamoto, J., Van Heijst, J., Lukin, O. & Schlüter, A. D. Two-dimensional polymers: Just a dream of synthetic chemists? *Angew. Chemie - Int. Ed.* **48**, 1030–1069 (2009).

21. Liu, G., Jin, W. & Xu, N. Two-Dimensional-Material Membranes: A New Family of High-Performance Separation Membranes. *Angew. Chemie Int. Ed.* **55**, 13384–13397 (2016).

22. Yuan, S. *et al.* Covalent organic frameworks for membrane separation. *Chem. Soc. Rev.* **48**, 2665–2681 (2019).

23. Horike, S., Umeyama, D. & Kitagawa, S. Ion conductivity and transport by porous coordination polymers and metal-organic frameworks. *Acc. Chem. Res.* **46**, 2376–2384 (2013).

24. Peng, Y., Yang, W., Peng, Y. & Yang, W. S. 2D Metal-Organic Framework Materials for Membrane-Based Separation. *Adv. Mater. Interfaces* **7**, 1901514 (2020).

25. Knebel, A. & Caro, J. Metal–organic frameworks and covalent organic frameworks as disruptive membrane materials for energy-efficient gas separation. *Nat. Nanotechnol.* **17**, 911–923 (2022).

26. Ying, Y. *et al.* Ultrathin Covalent Organic Framework Membranes via a Multi-Interfacial Engineering Strategy for Gas Separation. *Adv. Mater.* **34**, 2104946 (2022).

27. Sheberla, D. *et al.* High electrical conductivity in Ni3(2,3,6,7,10,11-hexaiminotriphenylene)2, a semiconducting metal-organic graphene analogue. *J. Am. Chem. Soc.* **136**, 8859–8862 (2014).

28. Chen, T. *et al.* Dimensionality Modulates Electrical Conductivity in Compositionally Constant One-, Two-, and Three-Dimensional Frameworks. *J. Am. Chem. Soc.* **144**, 5583–5593 (2022).

29. Xie, L. S., Skorupskii, G. & Dincă, M. Electrically Conductive Metal-Organic Frameworks. *Chem. Rev.* **120**, 8536–8580 (2020).

30. Sun, L., Campbell, M. G. & Dincə, M. Electrically Conductive Porous Metal–Organic Frameworks. *Angew. Chemie Int. Ed.* **55**, 3566–3579 (2016).

31. Talin, A. A. *et al.* Tunable electrical conductivity in metal-organic framework thin-film devices. *Science* **343**, 66–69 (2014).

32. Kelley, T. W. *et al.* Recent progress in organic electronics: Materials, devices, and processes. *Chem. Mater.* **16**, 4413–4422 (2004).

33. Wang, K., Yang, M. & Luo, J. *Spintronics: Materials, Devices, and Applications*. *Spintronics: Materials, Devices, and Applications* (2022). doi:10.1002/9781119698968.

34. Castro-Muñoz, R., Agrawal, K. V. & Coronas, J. Ultrathin permselective membranes: the latent way for efficient gas separation. *RSC Adv* **10**, 12653–12670 (2020).

35. Xiao, P. & Xu, Y. Recent progress in two-dimensional polymers for energy storage and conversion: design, synthesis, and applications. *J. Mater. Chem. A.* **6**, 21676–21695 (2018).

36. Day, R. W. *et al.* Single Crystals of Electrically Conductive Two-Dimensional Metal-Organic Frameworks: Structural and Electrical Transport Properties. *ACS Cent. Sci.* **5**, 1959–1964 (2019).

37. Strauss, I. *et al.* Metal-Organic Framework Co-MOF-74-Based Host-Guest Composites for Resistive Gas Sensing. *ACS App. Mate. Interfaces.* **11**, 14175–14181 (2019).

38. Huang, X. *et al.* Superconductivity in a Copper(II)-Based Coordination Polymer with Perfect Kagome Structure. *Angew. Chem., Int. Ed.* **130**, 152–156 (2018).

39. Xie, J. *et al.* Intrinsic glassy-metallic transport in an amorphous coordination polymer. *Nature* **611**, 479–484 (2022).

40. Takenaka, T. *et al.* Strongly correlated superconductivity in a copper-based metal-organic framework with a perfect kagome lattice. *Sci. Adv.* **7**, eabf3996 (2021).

41. Stavila, V., Talin, A. A. & Allendorf, M. D. MOF-based electronic and opto-electronic devices. *Chem. Soc. Rev.* **43**, 5994–6010 (2014).

42. Xu, X. *et al.* Van der Waals organic/inorganic heterostructures in the two-dimensional limit. *Chem* **7**, 2989–3026 (2021).

43. Balch, H. B. *et al.* Electronically Coupled 2D Polymer/MoS2Heterostructures. *J. Am. Chem. Soc.* **142**, 21131–21139 (2020).

44. Liu, K. *et al.* A Two-Dimensional Polyimide-Graphene Heterostructure with Ultra-fast

Interlayer Charge Transfer. *Angew. Chem., Int. Ed.* **60**, 13859–13864 (2021).

45. Rashid, R. B. *et al.* A Semiconducting Two-Dimensional Polymer as an Organic Electrochemical Transistor Active Layer. *Adv. Mater.* **34**, 2110703 (2022).
46. Huang, X. *et al.* A two-dimensional π-d conjugated coordination polymer with extremely high electrical conductivity and ambipolar transport behaviour. *Nat. Commun.* **6**, 1–8 (2015).
47. Feng, X. & Schlüter, A. D. Towards Macroscopic Crystalline 2D Polymers. *Angew. Chem., Int. Ed.* **57**, 13748–13763 (2018).
48. Cao, L. *et al.* Self-Supporting Metal–Organic Layers as Single-Site Solid Catalysts. *Angew. Chem., Int. Ed.* **55**, 4962–4966 (2016).
49. Payamyar, P., King, B. T., Öttinger, H. C. & Schlüter, A. D. Two-dimensional polymers: Concepts and perspectives. *Chem. Commun.* **52**, 18–34 (2016).
50. Bauer, T. *et al.* Synthesis of free-standing, monolayered organometallic sheets at the air/water interface. *Angew. Chem., Int. Ed.* **50**, 7879–7884 (2011).
51. Bhola, R. *et al.* A Two-Dimensional Polymer from the Anthracene Dimer and Triptycene Motifs. *J. Am. Chem. Soc.* **135**, 14134–14141 (2013).
52. Servalli, M. & Schlüter, A. D. Synthetic Two-Dimensional Polymers. *Annu. Rev. Mater. Res.* **47**, 361–389 (2017).
53. Wang, W. & Schlüter, A. D. Synthetic 2D Polymers: A Critical Perspective and a Look into the Future. *Macromol. Rapid Commun.* **40**, 1800719 (2019).
54. Cheng, B., Zhong, Y., Qiu, Y., Vaikuntanathan, S. & Park, J. Giant Gateable Osmotic Power Generation from a Goldilocks Two-Dimensional Polymer. *J. Am. Chem. Soc.* **145**, 5261–5269 (2023).
55. Zhong, Y. *et al.* Wafer-scale synthesis of monolayer two-dimensional porphyrin polymers for hybrid superlattices. *Science* **366**, 1379–1384 (2019).
56. Gobbi, M., Orgiu, E. & Samorì, P. When 2D Materials Meet Molecules: Opportunities and Challenges of Hybrid Organic/Inorganic van der Waals Heterostructures. *Adv. Mater.* **30**, 1706103 (2018).
57. Wang, Q. *et al.* Photo-Enhanced Chemo-Transistor Platform for Ultrasensitive Assay of Small Molecules. *J. Am. Chem. Soc.* **145**, 10035–10044 (2022).
58. Campbell, M. G., Liu, S. F., Swager, T. M. & Dincə, M. Chemiresistive Sensor Arrays from Conductive 2D Metal-Organic Frameworks. *J. Am. Chem. Soc.* **137**, 13780–13783 (2015).
59. Li, W. *et al.* Uniform and ultrathin high-κ gate dielectrics for two-dimensional electronic devices. *Nat. Electron.* **2**, 563–571 (2019).
60. Li, X. *et al.* Large-area synthesis of high-quality and uniform graphene films on copper

foils. *Science* **324**, 1312–1314 (2009).

61. Howarth, A. J. *et al.* Chemical, thermal and mechanical stabilities of metal-organic frameworks. *Nat. Rev. Mater.* **1**, 1–15 (2016).

62. Feng, X., Ding, X. & Jiang, D. Covalent organic frameworks. *Chem. Soc. Rev.* **41**, 6010–6022 (2012).

63. Dou, J. H. *et al.* Atomically precise single-crystal structures of electrically conducting 2D metal–organic frameworks. *Nat. Mater.* **20**, 222–228 (2021).

64. Ma, T. *et al.* Single-crystal x-ray diffraction structures of covalent organic frameworks. *Science* **361**, 48–52 (2018).

65. Evans, A. M. *et al.* Seeded growth of single-crystal two-dimensional covalent organic frameworks. *Science* **361**, 52–57 (2018).

66. Dong, R., Zhang, T. & Feng, X. Interface-Assisted Synthesis of 2D Materials: Trend and Challenges. *Chem. Rev.* **118**, 6189–6325 (2018).

67. Zhang, F., Fan, J. bing & Wang, S. Interfacial Polymerization: From Chemistry to Functional Materials. *Angew. Chem., Int. Ed.* **59**, 21840–21856 (2020).

68. Dong, R. *et al.* Large-Area, Free-Standing, Two-Dimensional Supramolecular Polymer Single-Layer Sheets for Highly Efficient Electrocatalytic Hydrogen Evolution. *Angew. Chem., Int. Ed.* **54**, 12058–12063 (2015).

69. Sahabudeen, H. *et al.* Wafer-sized multifunctional polyimine-based two-dimensional conjugated polymers with high mechanical stiffness. *Nat. Commun.* **7**, 13461 (2016).

Chapter 2: Developments in 2DP Synthesis

2.1 Introduction

Materials synthesis is a perpetual topic in chemistry. It is a complex and dynamic process that requires both knowledge and skill. However, it can be eventually boiled down to two fundamental aspects: the selection of appropriate reactants and the optimization of reaction conditions. These two aspects have been essential throughout the history of materials synthesis, from ancient alchemy to modern synthesis, and 2DP synthesis is no exception.

The starting reactants usually determine whether a material can be made and what minimum reaction conditions must be applied. In 2DP synthesis, the monomer also directly determines the final lattice structure, as it is formed by individual monomers. Therefore, in 2DP synthesis, the proper design of monomers is vital for the preferential formation of a 2D lattice. The preparation of the right monomer is at the intersection of organic and inorganic chemistry, which requires a good understanding of the structure-property relationship, sophisticated synthetic skills, and chemical intuition from years of experience.

However, getting the proper monomer is hardly halfway toward a successful synthesis of 2DPs. With the proper monomer, one also needs to optimize the conditions to generate high quality materials. The reaction condition is a broad term covering temperature, solvents, catalysts, modulators, etc., making it almost an infinite parameter space. To synthesize high-quality materials with controlled morphology, crystallinity, and phase, one must choose just the right conditions from this dauntingly large parameter space, making this task nearly impossible for an individual to achieve alone. Instead, it requires a collective effort from the community, with researchers collaborating to share knowledge, techniques, and resources.

In the early days of 2DP synthesis, the focus was to find the proper monomer and linkage chemistry that generate a 2D layered structure[1]. Major efforts were dedicated to the identification of planar monomers and planar bonding motifs (Fig. 1.2). However, the synthetic conditions were not too different from those used for 3D bulk materials. As a result, the synthesized products, although possessing a layered 2D structure, were usually in the form of microcrystals or powders rather than 2D monolayers/few-layers. To push the morphology to the real 2D regime, numerous advances in the synthetic conditions and techniques have been made. Among those techniques, interfacial synthesis has been the most fruitful one thanks to the intrinsic 2D nature of the interface[1,2].

In this chapter, we will discuss the developments in 2DP synthesis, from its very early proof-of-concept trials that focused on the realization of 2D layered structure in nano-sized crystals to the most advanced techniques that brought us to freestanding monolayers with the size of tens of centimeters.

2.2 Design & Chemistry of 2DPs

Among all low-dimensional materials, 2D materials was the last one to come, partly due to their extreme structural anisotropy. For inorganic materials, researchers can look for potential 2D materials from layered bulk materials, where the anisotropic in-plane and out-of-plan bonding allow for isolation and synthesis of individual layers. However, such approach usually does not apply to 2DPs, where a bottom-up approach is required for both materials design and synthesis.

Fortunately, with various synthetic toolboxes and decades of structure-property relationship research, this is hardly a challenge for chemists and materials scientists. In addition, the first inorganic 2D material, graphene, has showcased a working solution that chemists cannot be more familiar with – the *sp*^{2} hybridization. When a carbon-carbon double bond is formed between two *sp*^{2} carbon atoms, they define a plane where everything connected to them must reside. As the *sp*^{2} network (i.e., conjugation) extends, the plane grows only in two dimensions, with graphene being an extreme example where all carbon atoms are connected to each other through *sp*^{2} hybridization forming an infinite 2D layer of carbon atoms.

Inspired by this, initial 2DP monomer design focused on incorporating as much conjugation as possible. Noticeable examples of this philosophy include the use of monomers derived from pyrene, triphenylene, porphyrin, phthalocyanine (Fig. 1.2B). With proper linkage chemistry, individual planar molecules can be connected into the same plane, which gave rise to the first examples of 2DPs[3,4]. However, those large, conjugated molecules also introduce strong $\pi - \pi$ stacking, which is sometimes strong enough to compete with the in-plane bonding and leads to preferential out-of-plane crystal growth[5,6].

It is crucial to choose the right linkage chemistry. Several common linkages for 2DPs are shown in Fig. 1.2C. There are in general 2 common features for those linkages. First, the linkage should be planar. This one is obvious but limits the options for 2DP synthesis as nature usually favors high-symmetry 3D structure over 2D ones. For instance, neither tetrahedral or octahedral symmetries, two of the most common bonding symmetries in nature, is considered planar, and both are usually incompatible with a 2D lattice without certain distortion. A 2D lattice can be formed when planar linkages and planar molecules/monomers are arranged into the same plane through matching geometry of the monomers. Second, the linkage should have as few rotatable parts as possible. This is critical to keep the linkages and the monomers fixed in the same plane. For this purpose, multi-dentate bonds and conjugated bonds are usually adopted[1]. It is worth noting that the rotation of bonds can happen not only at the linkage but also within the monomer when single bonds are present. It is sometimes beneficial as it can allow certain distortion to accommodate otherwise frustrated 2D structure. However, it often increases the amorphousness and degrades the robustness of the structure, and hence, impedes the formation of a 2D lattice. As a result, most 2DP monomers are composed of either fused or connected aromatic rings to limit the rotation.

In addition, there is a practical aspect of the linkage chemistry that every 2DP synthesist needs to consider: how easy it is to make the bonds. As we mentioned before, synthesis of 2DPs usually

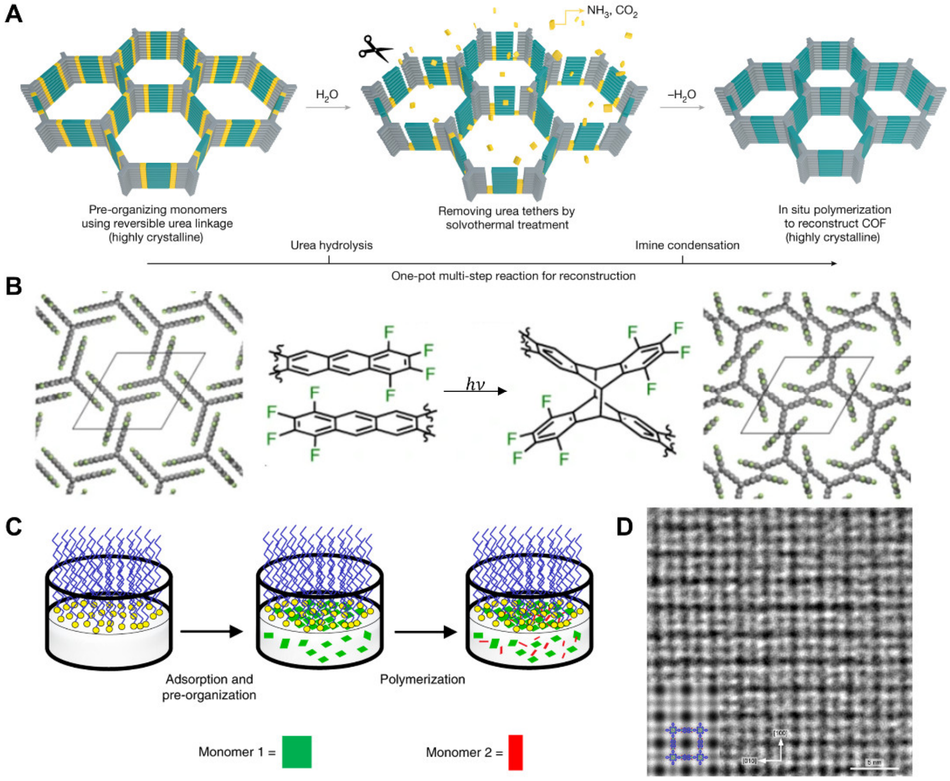

Figure 2.1 Templated synthesis of 2DPs with stable chemical bonds. **(A)** Synthesis of highly crystalline imine-2DP through reversible urea linkage pre-organization. Reproduced from Ref. 10. **(B)** Photopolymerization of pre-organized anthracene-based monomers. Reproduced from Ref. 8. **(C)** Surfactant-assisted polymerization of imide-2DPs and **(D)** a representative HRTEM image. Reproduced from Ref. 9.

needs to be done at a relatively low thermal budget to maintain the integrity of the final structure. Therefore, the formation of the linking bonds must be done before any of the reactants decomposes or undergoes any side reactions. In addition, to restore any structural defects and non-planarity caused during the polymerization, it is better to have reversible bonds that allow for correction for crystalline lattice. For these reasons, most early works on 2DP synthesis focus on reversible bonds that are easy to form and break[3,7]. However, the poor chemical stability of those bonds limits the application scenarios of the 2DP products. To address this problem, several strategies has been developed to take advantage of stable chemical bonds in 2DPs. For example, the single-step synthesis of a stable chemical bonds can be broken into multiple steps utilizing the topochemical polymerization. In those methods, a crystalline lattice is first formed by reversible assembly of the monomers through weak interactions (e.g. $\pi - \pi$ interaction[8], Coulomb interaction[9], reversible chemical bonds[10]). And then, irreversible bonds are formed between monomers without changing the crystalline assembly, leading to 2DPs of high crystallinity (Fig. 2.1). In addition, new synthetic processes, catalysts, and monomers are constantly being developed to achieve stable 2DPs, with a plethora of examples[11–14].

With the constant development of design and chemistry of 2DPs, more and more structures become available. Nevertheless, for any synthesis to produce high-quality materials with controlled morphology, fundamental understanding and knowledge must be combined with practical implementations. Without proper reaction conditions, the monomers would never form the desired linkage and structure. For the remaining of this chapter, we will discuss in detail how the knowledge we have learned so far are applied in several synthetic approaches that are able to generate, or at least bring us closer to, 2DPs with large-scale and high crystallinity.

2.3 Solution-Based Synthesis

In solution-based synthesis, all the reactants are dissolved (or sometimes dispersed) homogeneously in a solvent, where desired products formed through control of the temperature, catalysts, molar ratio, etc. Because it is the most common method for synthesizing 3D framework materials, such as metal-organic frameworks (MOFs) and covalent-organic frameworks (COFs), solution-based synthesis was used to test the feasibility of 2DP synthesis when proper monomers and linkage chemistries first became available[1,15,16]. For early trials, however, the synthetic conditions for solution-based 2DP synthesis were not significantly different from those used for synthesis of 3D frameworks, resulting in poorly controlled morphology in the form of powder/nanocrystals[17–19] (Fig. 2.2). In some cases, the strong $\pi - \pi$ stacking between the molecules can obscure any 2D features of the resulting products, requiring crystallography studies to reveal the layered structure[4,6]. Despite the poor morphology control, solution-based synthesis of 2DPs has offered a viable approach to identify proper monomer designs, develop new linkage chemistry, and refine synthetic conditions. Today, solution-based synthesis remains a major test field for novel 2DP synthesis, providing a solid foundation for many other methods that have emerged in recent years.

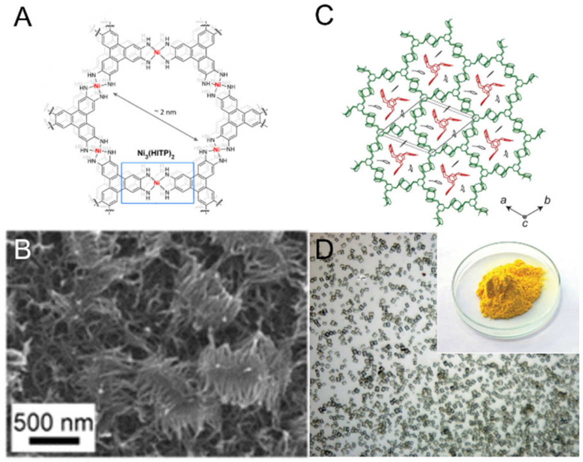

Figure 2.2 Typical morphology of solution-synthesized 2DPs. (A) Structure of the $Ni_3(HITP)_2$ 2DP. (B) SEM images of the $Ni_3(HITP)_2$ 2DP film. (C) Structure of the 2DP3. (D) Optical image of the microcrystals of 2DP3. Inset: photograph of the 2DP3 crystalline powder. Reproduced from Ref. 17-19.

In solution-based 2DP synthesis, anisotropic growth can only arise from structural anisotropy since all reactants are homogeneously dispersed in the solvent. Therefore, the most critical factor in solution-based 2DP synthesis is to engineer the structural anisotropy through monomer and linkage chemistry design. In works that focuses on getting high quality crystalline 2DPs rather than morphology control, it is important to balance the intralayer and interlayer interaction. It has been shown that strong interlayer interaction helps the assembly of monomers in adjacent layers, thereby increasing the crystallinity of the materials with the annealing process[20–22]. As a result, many non-covalent interactions have been utilized to increase the interlayer interaction, and many of those strategies have yielded crystalline power of 2DPs[23–27] (Fig. 2.3). However, whether strong interlayer interaction is always beneficial for enhancing crystallinity is still under debate with results supporting both sides reported[28,29].

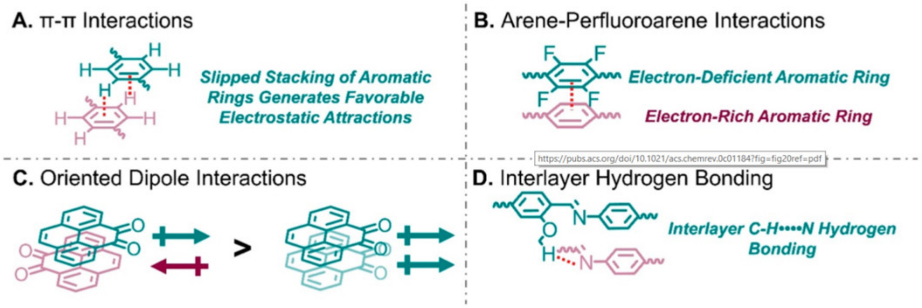

Figure 2.3 Typical interlayer interactions in 2DPs. Reproduced from Ref. 1.

In contrast, for better control of the morphology or formation of monolayer/few-layer nanosheets, it is always beneficial to increase the in-plane bonding and/or reduce out-of-plane stacking. One notable example is the synthesis of Zr/Hf-based 2DPs through solution synthesis (Fig. 2.4). The 3D Zr/Hf-based MOFs are known for their remarkable chemical and thermal stability, as well as the structural variety from the 12-connectivity Zr_6/Hf_6 nodes[30]. Although the

12-connectivity nodes do not form a 2D lattice, it is possible to control the connectivity by adding monocarboxylic acid, which cap the nodes instead of connecting them to each other. By doing so, the large size of the Zr_6/Hf_6 nodes and the presence of capping ligands greatly reduce the $\pi - \pi$ stacking between layers. Together with the strong in-plane Zr/Hf cluster-carboxylate coordination bonds, this has enabled high yield of monolayer/few-layer 2DP nanosheets that can be obtained through ultrasonic exfoliation[31].

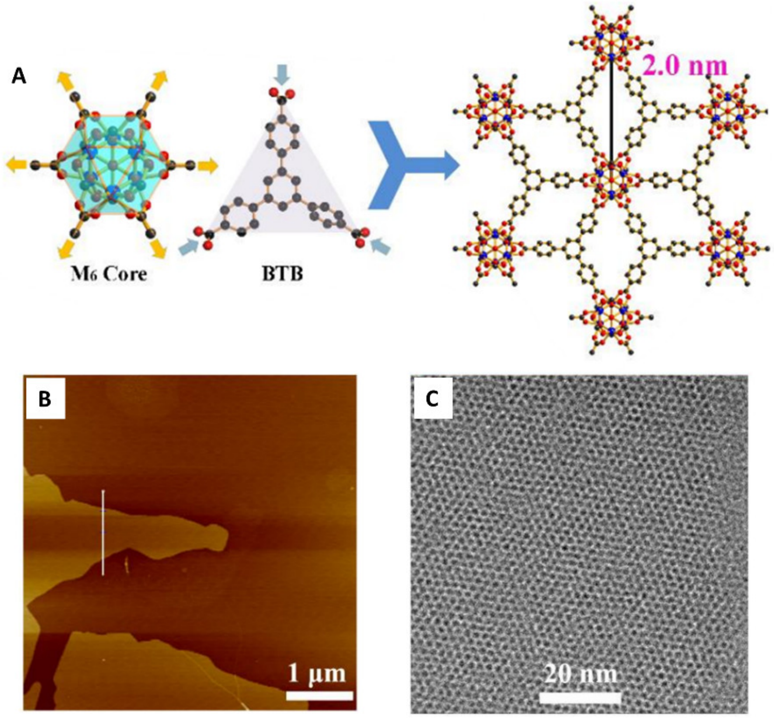

Figure 2.4 Zr-based 2DP synthesized from solvothermal methods. **(A)** Building blocks and structure of the Zr-based 2DP. **(B)** AFM image of solution-exfoliated Zr-2DP. **(C)** HRTEM of solution-exfoliated Zr-2DP. Reproduced from Ref. 31.

Another strategy for promoting 2D growth in solution-based synthesis involves using a 2D substrate. Although technically, growth in this case is an interfacial one that happens at a liquid-solid interface, we include it in our discussion for solution-based 2DP synthesis since all the reactants are still homogeneously dispersed in a solvent. When a liquid-solid interface is present, heterogeneous nucleation on the solid surface can lead to thin film growth on the solid substrate. However, such nucleation is usually promoted by the oxygen-rich surface and results in a thin film composed of randomly oriented nanocrystalline domains, which can hardly be considered

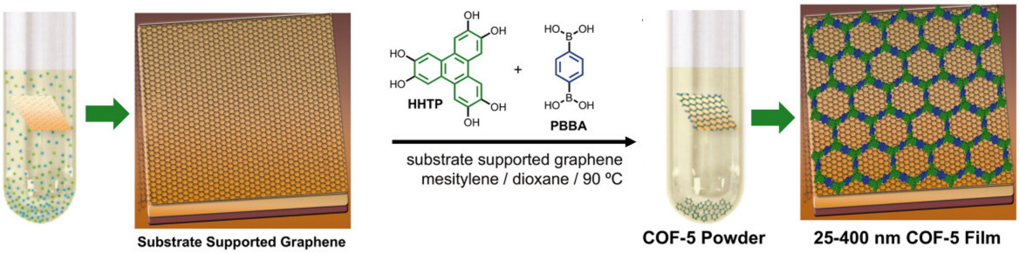

Figure 2.5 Synthesis of oriented 2DPs on monolayer graphene. Reproduced from Ref. 32.

2D. In 2011, Dichtel and coworkers[32] developed an ingenious method of using graphene as the growth substrate for 2DPs (Fig. 2.5). The extreme flatness and dangling bond free surface of graphene allows for face-to-face stacking of 2DP monomers onto the substrate, promoting aligned growth of 2DPs with crystalline plane parallel to the substrate. This method allowed for large-scale 2DP synthesis that is only limited by the inorganic 2D substrate and was later extended to other 2D substrates, resulting in various 2DP/inorganic 2D materials heterostructures. However, despite preferred crystalline orientation, it is not possible to precisely control the layer number of grown 2DPs due to the homogeneous solution environment, which is the limitation for all solution-based synthesis methods. To achieve precise layer number control and move towards the real 2D regime, it is necessary to develop other methods that are fundamentally different from a homogeneous reaction mixture of reactants.

2.4 Interfacial Synthesis

Many heterogeneous interfaces inherently exhibit a 2D nature, and the fabrication and study of these interfaces even predates those of 2D materials[33–36]. Therefore, it is natural to use an interface for the synthesis of 2DPs as the two have matching dimensionality. Many different forms of heterogeneous interfaces have been utilized for 2DP synthesis[37–41] (Fig. 2.6). In this

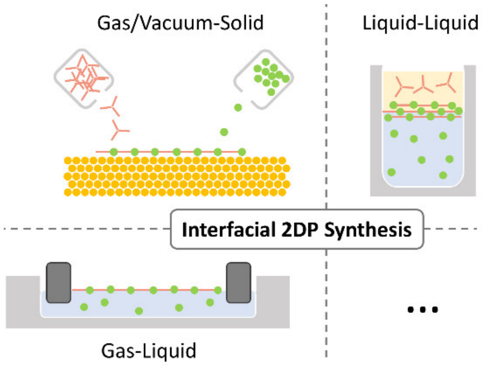

Figure 2.6 Different interfacial methods for 2DP synthesis.

chapter, we will focus our discussion on recent developments regarding gas/vacuum-solid, air-liquid and liquid-liquid interfacial 2DP synthesis, as they have accounted for a significant portion of relevant research and are likely to continue developing in the future.

Gas/Vacuum-Solid interfacial synthesis

The gas/vacuum-solid interfacial synthesis is the most popular method for inorganic 2D materials synthesis and is prevalent in almost all modern thin film deposition techniques (ALD, CVD, MBE, PVD, etc.). It is considered to be the most stable interface against mechanical and thermal disturbance. In fact, various 2DP structures have been deposited on different substrates in ultrahigh vacuum (UHV) chambers[8,42,43]. For instance, in the work by Ditchtel and Crommie group[43], monolayers of COF-366 was deposited on Au(111) surface in UHV, and the electronic structure of the 2DP was studied by scanning tunneling microscopy (STM). Moreover, the metal substrate can facilitate certain linkage chemistries that are hard to access in a solution-based synthesis, allowing the formation of stable chemical bonds under non-destructive conditions[44–46]. However, the lateral size of the 2DP in this method is limited by the underlying substrate terraces, which is typically a few hundred nanometers. Additionally, it is constrained by the availability of UHV equipment and limited range of substrates that can be used.

In recent years, many researchers investigated the possibility of utilizing a gas-solid interface in chemical vapor deposition (CVD) for precise monolayer 2DP synthesis. However, although sub-2nm and even monolayer films have been synthesized[47], the high reaction temperature often leads to decomposition of the monomer and 2DP, resulting in amorphous products. Nonetheless, the use of a gas-solid interface in CVD for 2DP synthesis shows promise for large scale, high crystallinity, and precise layer control[47,48]. Further research is required to overcome the limitations of high-temperature decomposition and to expand the range of suitable substrates.

Liquid-Liquid Interfacial Synthesis

Compared to the gas/vacuum-solid interface, the liquid-liquid interface is a simpler and more accessible method for synthesizing 2DPs, as it does not require complex apparatus. In a typical liquid-liquid interfacial synthesis, reactants, catalysts and other reagents are dissolved separately in two immiscible solvents (e.g. water and chloroform) so that the reaction confined at the interface where all the participating reagents converge (Fig. 2.6)[49,50]. Thanks to the all-liquid environment, many well-established reactions and techniques in solution-based synthesis can be

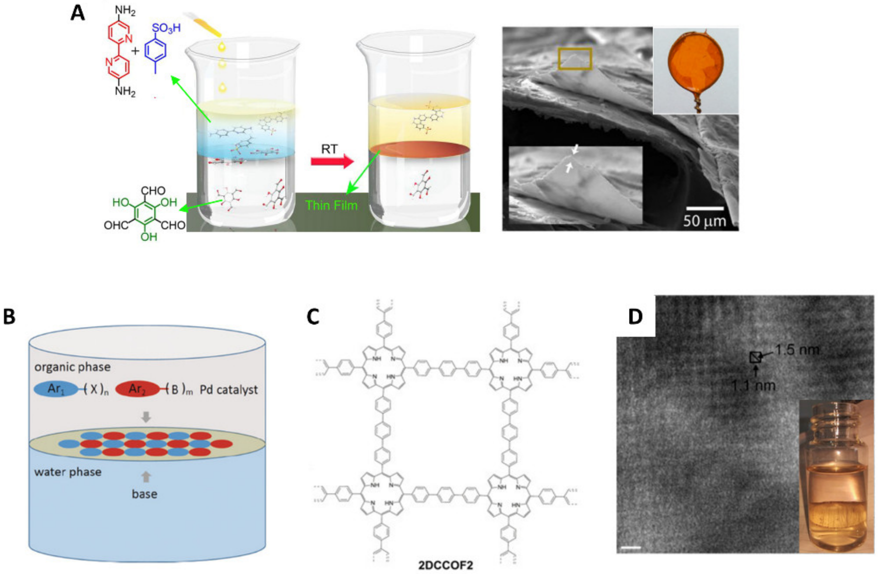

Figure 2.7 Examples of 2DPs synthesized at a liquid-liquid interface. **(A)** Synthesis of an imine-2DP at a water-chloroform interface. Reproduced from Ref. 49. **(B)** Schematic of interfacial synthesis of a conjugated 2DP using Suzuki coupling. **(C)** Structural illustration of the conjugated 2DP. **(D)** TEM image of the 2DP and a picture of the 2DP at the chloroform-water interface (inset). Reproduced from Ref. 50.

directly applied in liquid-liquid interfacial synthesis. For instance, Li and coworkers demonstrated that Suzuki coupling can be applied to a water-chloroform interfacial synthesis, which produced stable C-C connected 2DPs with intense PXRD peaks[50]. Dichtel's group also showed that a Lewis acid catyalyst, Sc(OTf)$_3$, improved the crystallinity and reduced reaction time in solution-based synthesis for 2DPs. The same catalyst also demonstrated similar effect for an interfacial synthesis, and 2DPs as thin as 3nm was synthesized[51,52]. Moreover, in many cases, 2DPs synthesized through liquid-liquid interfacial synthesis demonstrate better morphologies and properties. For instance, Zhu and coworkers showed that CuBHT, a Cu benzoate 2DP, showed increased electrical conductivity when synthesized using interfacial methods[53], and with improved procedures, the same group later observed superconductivity from the same 2DP[54,55] (Fig. 2.8).

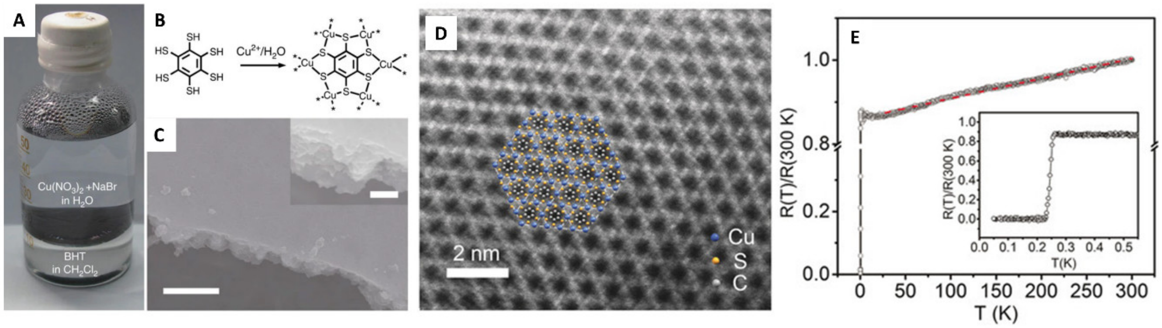

Figure 2.8 Synthesis and structure characterization of the CuBHT 2DP. **(A)** Photograph of the CuBHT synthesis setup. **(B)** Reaction scheme for the CuBHT. **(C)** SEM images of the synthesized CuBHT film. Scale bar: 200 nm (main) and 100 nm (inset). **(D)** HRTEM image of the CuBHT film. **(E)** Relative resistance of the CuBHT film at various temperatures. Reproduced from Ref. 54 and 55.

However, the interface formed between two liquids is usually not as well-defined as that formed between gas-solid or gas-liquid, and many reagents may have a finite solubility in both liquid phases that can further degrade the confinement. Consequently, the film is usually composed of randomly oriented nanocrystalline particulates, with large thickness and non-uniform surfaces.

Nonetheless, the simplicity and generality of liquid-liquid interfacial synthesis makes it an attractive method for production of 2DP thin films and membranes, as well as exploration of novel structures and reactions.

Gas-Liquid Interfacial Synthesis

Currently, the most common method to prepare monolayer/few-layer 2DPs is the gas-liquid interfacial synthesis, particularly using the Langmuir-Blodgett (LB) deposition. The LB deposition forms a monolayer by compressing free or sub-monolayer monomers at an air-water interface. By monitoring the surface tension and optical contrast of the film, LB deposition can work with a variety of monomers and produce 2DPs with large lateral sizes[56–58]. The LB deposition can be further improved by pre-organization of monomers at the interface before polymerization, as the pre-organized monomers can accommodate the mechanical stress through their fluidity and provide a template for crystallization. For instance, Makiura and coworkers showed that polymerization of pre-assembled porphyrin monomers shows a better crystallinity compared to directly reacted ones[59]. In a series of works by Schlüter's group, they showed that

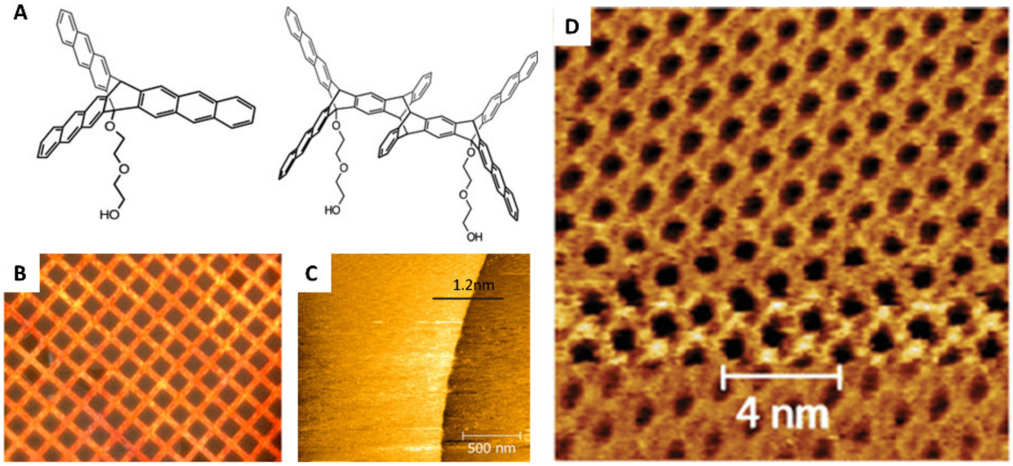

Figure 2.9 Topochemically polymerized 2DP using tri-anthracene monomers. **(A)** Schemes for the tri-anthracene monomer and their photopolymerization. **(B)** Reflectance image of the synthesized 2DP on Cu grids. **(C)** AFM image of the 2DP film. **(D)** STM topology of the synthesized 2DP. Reproduced from Ref. 62.

topochemically polymerized (i.e. polymerization of monomers aligned in the crystal state) tris(anthracene) monomers demonstrated great mechanical strength and the crystalline domains can be imaged with STM at molecular resolution[38,60–62] (Fig. 2.9). However, the mechanical stress can never be completely removed as long as macroscopic compression is applied, and the low thermal budget for an open air-water interface would always limit the crystallinity this method can achieve.

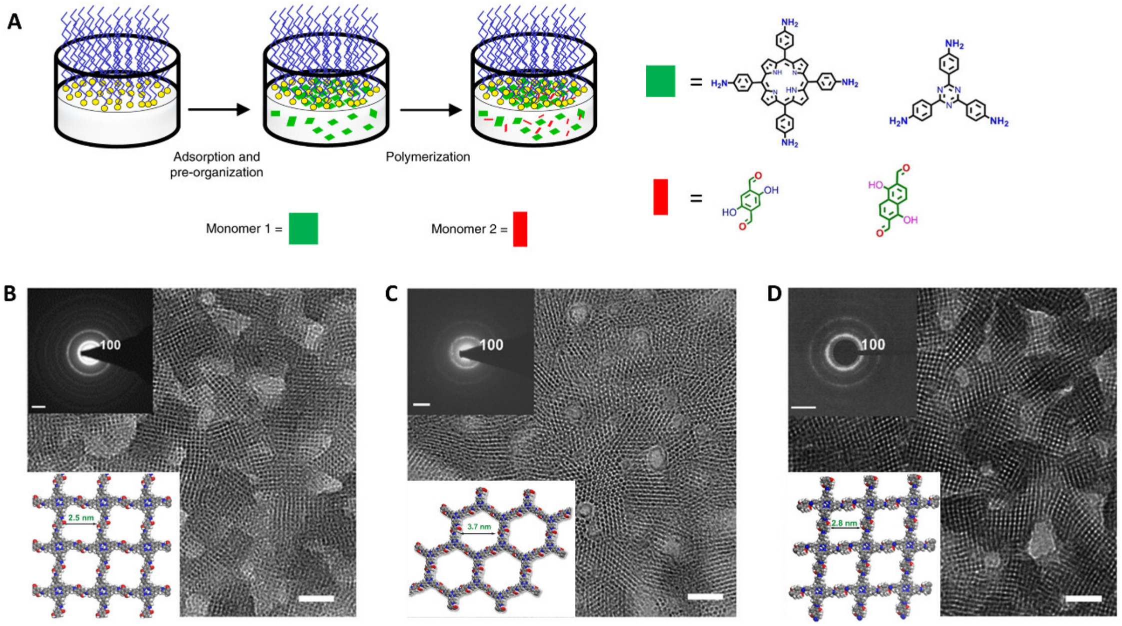

Figure 2.10 Surfactant-assisted synthesis of crystalline 2DPs. **(A)** Schematic illustration of the synthesis procedures. **(B)-(D)** HRTEM of various crystalline 2DPs synthesized using the method, with SAED patterns and structures of each 2DP shown in insets. Reproduced from Ref. 63.

The monomer pre-organization has also been utilized in other gas-liquid interfacial synthesis methods. For example, Feng's group has demonstrated that by using a monolayer of charged surfactants as template, oppositely charged monomers can be pre-organized under the surfactants and form a highly crystalline 2DP film with tunable thickness from a couple of nanometers to a hundred nanometers[9,63] (Fig. 2.10). With this method, the researchers were able to get several-micrometer crystalline domains and do so with strong chemical bonds at room temperature that usually require much higher temperature in solution-based synthesis[8,61]. While this surfactant-assisted approach significantly increases the crystallinity of the film, the charge-induced monomer pre-organization forfeit the strict confinement of the air-water interface, and therefore monolayer thickness control was not achieved.

2.5 Summary

In this chapter, we discussed the major factors to consider for 2DP synthesis and presented several different synthetic approaches for chemical and morphological control of the products. The focus of 2DP synthesis gradually shifted from the structural aspects to functions and morphology control. Multiple interfacial synthesis methods have enabled production of monolayer/few-layer 2DPs but reliable large-scale production and the ultimate combination of precise layer control and high crystallinity is still missing. In the next chapter, we will introduce our approach for wafer-scale synthesis of monolayer 2DPs and compare it with other interfacial methods discussed in this chapter.

2.6 References

1. Evans, A. M. *et al.* Two-Dimensional Polymers and Polymerizations. *Chem. Rev.* **122**, 442–564 (2022).
2. Zhang, F., Fan, J. bing & Wang, S. Interfacial Polymerization: From Chemistry to Functional Materials. *Angew. Chemie - Int. Ed.* **59**, 21840–21856 (2020).
3. Côté, A. P. *et al.* Porous, crystalline, covalent organic frameworks. *Science* **310**, 1166–1170 (2005).
4. Hmadeh, M. *et al.* New porous crystals of extended metal-catecholates. *Chem. Mater.* **24**, 3511–3513 (2012).
5. Dou, J. H. *et al.* Atomically precise single-crystal structures of electrically conducting 2D metal–organic frameworks. *Nat. Mater.* **20**, 222–228 (2021).
6. Day, R. W. *et al.* Single Crystals of Electrically Conductive Two-Dimensional Metal-

Organic Frameworks: Structural and Electrical Transport Properties. *ACS Cent. Sci.* **5**, 1959–1964 (2019).

7. Wan, S. *et al.* Covalent organic frameworks with high charge carrier mobility. *Chem. Mater.* **23**, 4094–4097 (2011).
8. Grossmann, L. *et al.* On-surface photopolymerization of two-dimensional polymers ordered on the mesoscale. *Nat. Chem.* **13**, 730–736 (2021).
9. Liu, K. *et al.* On-water surface synthesis of crystalline, few-layer two-dimensional polymers assisted by surfactant monolayers. *Nat. Chem.* **11**, 994–1000 (2019).
10. Zhang, W. *et al.* Reconstructed covalent organic frameworks. *Nature* **604**, 72–79 (2022).
11. Zhou, D., Tan, X., Wu, H., Tian, L. & Li, M. Synthesis of C−C Bonded Two-Dimensional Conjugated Covalent Organic Framework Films by Suzuki Polymerization on a Liquid-Liquid Interface. *Angew. Chemie* **131**, 1390–1395 (2019).
12. Wang, Z. *et al.* On-water surface synthesis of charged two-dimensional polymer single crystals via the irreversible Katritzky reaction. *Nat. Synth.* **1**, 69–76 (2021).
13. Jin, E. *et al.* Two-dimensional sp 2 carbon–conjugated covalent organic frameworks. *Science* **357**, 673–676 (2017).
14. He, T., Geng, K. & Jiang, D. All sp2 carbon covalent organic frameworks. *Trends Chem.* **3**, 431–444 (2021).
15. Matsumoto, M. *et al.* Rapid, Low Temperature Formation of Imine-Linked Covalent Organic Frameworks Catalyzed by Metal Triflates. *J. Am. Chem. Soc.* **139**, 4999–5002 (2017).
16. Bhola, R. *et al.* A Two-Dimensional Polymer from the Anthracene Dimer and Triptycene Motifs. *J. Am. Chem. Soc.* **135**, 14134–14141 (2013).
17. Kory, M. J. *et al.* Gram-scale synthesis of two-dimensional polymer crystals and their structure analysis by X-ray diffraction. *Nat. Chem.* **6**, 779–784 (2014).
18. Sheberla, D. *et al.* High electrical conductivity in Ni3(2,3,6,7,10,11-hexaiminotriphenylene)2, a semiconducting metal-organic graphene analogue. *J. Am. Chem. Soc.* **136**, 8859–8862 (2014).
19. Wang, W. & Schlüter, A. D. Synthetic 2D Polymers: A Critical Perspective and a Look into the Future. *Macromol. Rapid Commun.* **40**, 1800719 (2019).
20. Auras, F. *et al.* Synchronized Offset Stacking: A Concept for Growing Large-Domain and Highly Crystalline 2D Covalent Organic Frameworks. *J. Am. Chem. Soc.* **138**, 16703–16710 (2016).
21. Ascherl, L. *et al.* Molecular docking sites designed for the generation of highly crystalline covalent organic frameworks. *Nat. Chem.* **8**, 310–316 (2016).
22. Keller, N. *et al.* Dibenzochrysene enables tightly controlled docking and stabilizes

photoexcited states in dual-pore covalent organic frameworks. *Nanoscale* **11**, 23338–23345 (2019).

23. Spitler, E. L. *et al.* A 2D covalent organic framework with 4.7-nm pores and insight into its interlayer stacking. *J. Am. Chem. Soc.* **133**, 19416–19421 (2011).

24. Braunecker, W. A. *et al.* Phenyl/Perfluorophenyl Stacking Interactions Enhance Structural Order in Two-Dimensional Covalent Organic Frameworks. *Cryst. Growth Des.* **18**, 4160–4166 (2018).

25. Halder, A. *et al.* Ultrastable Imine-Based Covalent Organic Frameworks for Sulfuric Acid Recovery: An Effect of Interlayer Hydrogen Bonding. *Angew. Chemie Int. Ed.* **57**, 5797–5802 (2018).

26. Jin, S. *et al.* Creation of Superheterojunction Polymers via Direct Polycondensation: Segregated and Bicontinuous Donor-Acceptor π-Columnar Arrays in Covalent Organic Frameworks for Long-Lived Charge Separation. *J. Am. Chem. Soc.* **137**, 7817–7827 (2015).

27. Salonen, L. M. *et al.* A supramolecular strategy based on molecular dipole moments for high-quality covalent organic frameworks. *Chem. Commun.* **52**, 7986–7989 (2016).

28. Wu, X., Han, X., Liu, Y., Liu, Y. & Cui, Y. Control Interlayer Stacking and Chemical Stability of Two-Dimensional Covalent Organic Frameworks via Steric Tuning. *J. Am. Chem. Soc.* **140**, 16124–16133 (2018).

29. Feriante, C. *et al.* New mechanistic insights into the formation of imine-linked two-dimensional covalent organic frameworks. *J. Am. Chem. Soc.* **142**, 18637–18644 (2020).

30. Bai, Y. *et al.* Zr-based metal–organic frameworks: design, synthesis, structure, and applications. *Chem. Soc. Rev.* **45**, 2327–2367 (2016).

31. Cao, L. *et al.* Self-Supporting Metal-Organic Layers as Single-Site Solid Catalysts. *Angew. Chemie - Int. Ed.* **55**, 4962–4966 (2016).

32. Colson, J. W. *et al.* Oriented 2D covalent organic framework thin films on single-layer graphene. *Science* **332**, 228–231 (2011).

33. Grimes, C. C. Electrons in surface states on liquid helium. *Surf. Sci.* **73**, 379–395 (1978).

34. Platzman, P. M. & Dykman, M. I. Quantum computing with electrons floating on liquid helium. *Science* **284**, 1967–1969 (1999).

35. Peeters, F. M. Two-dimensional Wigner crystal of electrons on a helium film: Static and dynamical properties. *Phys. Rev. B* **30**, 159 (1984).

36. Thornton, T. J., Pepper, M., Ahmed, H., Andrews, D. & Davies, G. J. One-Dimensional Conduction in the 2D Electron Gas of a GaAs-AlGaAs Heterojunction. *Phys. Rev. Lett.* **56**, 1198 (1986).

37. Zhong, Y. *et al.* Wafer-scale synthesis of monolayer two-dimensional porphyrin polymers for hybrid superlattices. *Science* **366**, 1379–1384 (2019).

38. Murray, D. J. *et al.* Large Area Synthesis of a Nanoporous Two-Dimensional Polymer at the Air/Water Interface. *J. Am. Chem. Soc.* **137**, 3450–3453 (2015).

39. Dong, R., Zhang, T. & Feng, X. Interface-Assisted Synthesis of 2D Materials: Trend and Challenges. *Chem. Rev.* **118**, 6189–6325 (2018).

40. Pal, T. *et al.* Interfacial transmetallation synthesis of a platinadithiolene nanosheet as a potential 2D topological insulator. *Chem. Sci.* **10**, 5218–5225 (2019).

41. Galeotti, G. *et al.* Synthesis of mesoscale ordered two-dimensional π-conjugated polymers with semiconducting properties. *Nat. Mater.* **19**, 874–880 (2020).

42. Bieri, M. *et al.* Surface-supported 2D heterotriangulene polymers. *Chem. Commun.* **47**, 10239–10241 (2011).

43. Chen, C. *et al.* Local Electronic Structure of a Single-Layer Porphyrin-Containing Covalent Organic Framework. *ACS Nano* **12**, 385–391 (2018).

44. Zhong, W. *et al.* Synthesizing Cr-Based Two-Dimensional Conjugated Metal-Organic Framework Through On-Surface Substitution Reaction. *Small* **19**, 2207877 (2023).

45. Pinardi, A. L. *et al.* Tailored formation of n-doped nanoarchitectures by diffusion-controlled on-surface (Cyclo)Dehydrogenation of heteroaromatics. *ACS Nano* **7**, 3676–3684 (2013).

46. Gutzler, R. *et al.* Ullmann-type coupling of brominated tetrathienoanthracene on copper and silver. *Nanoscale* **6**, 2660–2668 (2014).

47. Liu, R. *et al.* Chemical Vapor Deposition Growth of Linked Carbon Monolayers with Acetylenic Scaffoldings on Silver Foil. *Adv. Mater.* **29**, 1604665 (2017).

48. Liu, M. *et al.* Two-dimensional covalent organic framework films prepared on various substrates through vapor induced conversion. *Nat. Commun.* **13**, (2022).

49. Dey, K. *et al.* Selective Molecular Separation by Interfacially Crystallized Covalent Organic Framework Thin Films. *J. Am. Chem. Soc.* **139**, 13083–13091 (2017).

50. Li, C. *et al.* Two-Dimensional Conjugated Polymer Synthesized by Interfacial Suzuki Reaction: Towards Electronic Device Applications. *Angew. Chemie - Int. Ed.* **59**, 9403–9407 (2020).

51. Matsumoto, M. *et al.* Lewis-Acid-Catalyzed Interfacial Polymerization of Covalent Organic Framework Films. *Chem* **4**, 308–317 (2018).

52. Matsumoto, M. *et al.* Rapid, Low Temperature Formation of Imine-Linked Covalent Organic Frameworks Catalyzed by Metal Triflates. *J. Am. Chem. Soc.* **139**, 4999–5002 (2017).

53. Huang, X. *et al.* A two-dimensional π-d conjugated coordination polymer with extremely high electrical conductivity and ambipolar transport behaviour. *Nat. Commun.* **6**, 1–8 (2015).

54. Huang, X. *et al.* Superconductivity in a Copper(II)-Based Coordination Polymer with Perfect Kagome Structure. *Angew. Chemie* **130**, 152–156 (2018).

55. Takenaka, T. *et al.* Strongly correlated superconductivity in a copper-based metal-organic framework with a perfect kagome lattice. *Sci. Adv.* **7**, eabf3996 (2021).

56. Makiura, R. *et al.* Surface nano-architecture of a metal-organic framework. *Nat. Mater.* **9**, 565–571 (2010).

57. Sahabudeen, H. *et al.* Wafer-sized multifunctional polyimine-based two-dimensional conjugated polymers with high mechanical stiffness. *Nat. Commun.* **7**, 13461 (2016).

58. Müller, V. *et al.* A Two-Dimensional Polymer Synthesized at the Air/Water Interface. *Angew. Chemie Int. Ed.* **57**, 10584–10588 (2018).

59. Makiura, R. & Konovalov, O. Interfacial growth of large-area single-layer metal-organic framework nanosheets. *Sci. Rep.* **3**, 2506 (2013).

60. Müller, V. *et al.* Structural Characterization of a Covalent Monolayer Sheet Obtained by Two-Dimensional Polymerization at an Air/Water Interface. *Angew. Chemie - Int. Ed.* **56**, 15262–15266 (2017).

61. Payamyar, P. *et al.* Synthesis of a covalent monolayer sheet by photochemical anthracene dimerization at the air/water interface and its mechanical characterization by AFM indentation. *Adv. Mater.* **26**, 2052–2058 (2014).

62. Murray, D. J. *et al.* Large Area Synthesis of a Nanoporous Two-Dimensional Polymer at the Air/Water Interface. *J. Am. Chem. Soc.* **137**, 3450–3453 (2015).

63. Sahabudeen, H. *et al.* Highly Crystalline and Semiconducting Imine-Based Two-Dimensional Polymers Enabled by Interfacial Synthesis. *Angew. Chemie - Int. Ed.* **59**, 6028–6036 (2020).

64. Wang, Z. *et al.* On-water surface synthesis of charged two-dimensional polymer single crystals via the irreversible Katritzky reaction. *Nat. Synth. 2021 11* **1**, 69–76 (2021).

Chapter 3: Wafer-Scale Synthesis of Monolayer 2DPs

3.1 Introduction

With decades of development in 2DP synthesis, hundreds of different 2DP structures are now available through various synthetic techniques[1]. However, little progress has been made in the production of large-scale monolayer 2DPs, which in some restrictive opinions are the only form that satisfies the definition of 2D materials. Although this constraint is no longer widely accepted, monolayers are still the ideal form to deploy the interesting properties of 2DPs, which can be largely attributed to the anisotropic structure and the accessible molecular units[2].

Moreover, access to monolayer 2DPs would also enable layer-by-layer integration of distinct 2DPs as well as other inorganic 2D materials free of lattice-matching constraint, a method often referred to as van der Waals (vdW) integration. Such integration strategy has been widely used with inorganic 2D materials and has produced many interesting properties not available in individual component such as superconductivity and Wigner crystals[3]. The chemical tunability and structural diversity of 2DPs would allow for molecular-level engineering of the properties and functionalities in vdW heterostructures, and provide a versatile platform for the design and tuning of interlayer interaction when combined with recent development in moiré physics. With improved materials quality and processing techniques, it is also possible to investigate the moiré physics of heterostructures made of 2DPs alone, as that in bilayer graphene, which has so far remained completely unexplored mainly due to the materials limitation.

For a very long time, LB deposition has been the only method that can produce large-scale monolayers of 2DPs, but the quality of the materials is usually compromised by the mechanical compression process. As a result, it is extremely challenging to scalably synthesize monolayer

2DP films and subsequently integrate them with other materials with monolayer precision[2,4]. The challenges of large-scale 2DP synthesis have been discussed in detail in Chapter 1 &2. The fragility of the monolayer further impede its processing and integration. Previous experiments have reported progress toward large-scale synthesis of 2DPs[5–13], but with limited success regarding wafer-scale homogeneity, microscopic characterization of crystalline structures, and scalable thin-film integration[14].

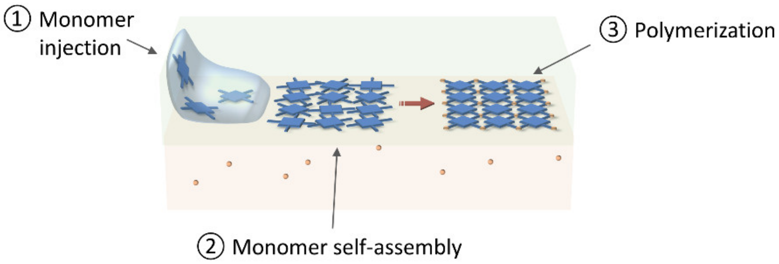

Figure 3.1 Schematic of LAP synthesis

In this chapter, we present a novel interfacial synthesis method, which is the main experimental advance in this thesis. It enables wafer-scale synthesis of monolayer 2DPs from various monomers and linkage chemistries (Fig. 3.1). The method utilizes the self-assembly of amphiphilic monomers at a water-pentane interface to pre-organize the monomers while using laminar flow formed by controlled monomer delivery to achieve wafer-scale monolayer film without mechanical compression. This approach, named as laminar assembly polymerization (LAP), incorporated key features necessary for scalable and facile processing, including large-area synthesis, ambient growth conditions, and compatibility with established patterning and integration methods. We will describe the experimental setup of the method, detail our mechanistic understanding of the process, and present experimental results of several wafer-scale 2DPs synthesized using LAP.

3.2 Laminar Assembly Polymerization

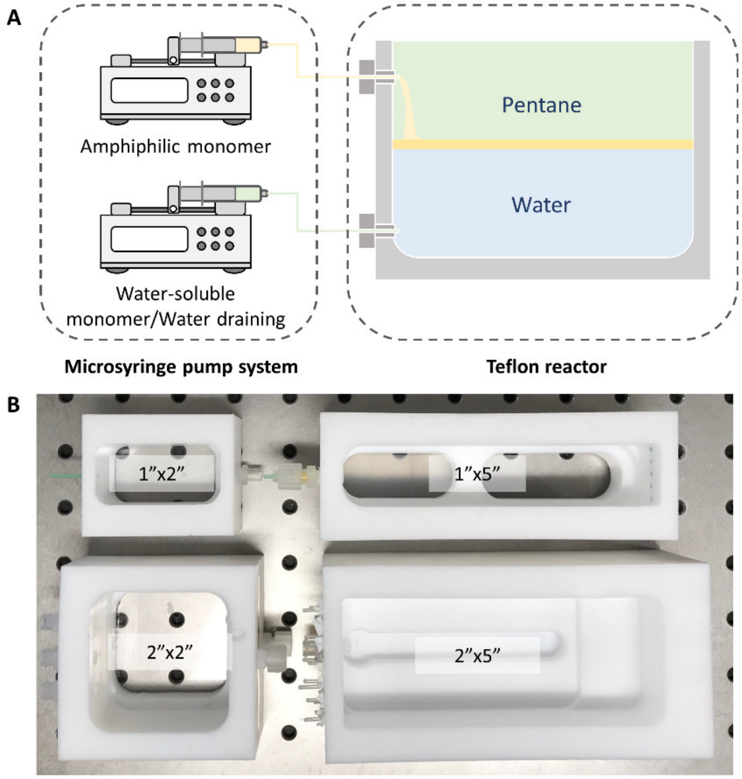

Figure 3.2 Experimental setup of LAP. **(A)** Schematic of LAP setup. **(B)** PTFE LAP reactors of various sizes.

The laminar assembly polymerization (LAP) method is a special liquid-liquid interfacial synthesis method that polymerizes amphiphilic monomers at a well-defined, stable pentane-water interface. Fig. 3.2A shows a schematic illustration of the LAP setup. The setup has two major components: a) the reactor where pentane-water interface is formed and polymerization happens, and b) the microsyringe pump system that precisely controls the amount and rate of monomer being introduced.

In order to form a stable pentane-water interface and be compatible with as many chemical reagents as possible, the reactor is custom-made with a Teflon block. For different purposes, the size and shape of the reactors can be varied (Fig. 3.2B). For all reactors, the injection ports are located at short edge wall allowing a side-injection. The side-injection is critical for the formation of stable laminar flows and will be discussed more in detail in the next section. For precise control of the monomer injection, the microsyringe pump system is connected to the injection port on the reactor through a very thin fluorinated plastic tubing (inner diameter of 150

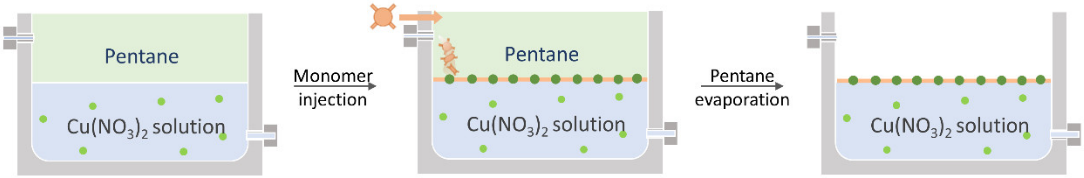

Figure 3.3 Schematic illustration of LAP procedures.

μm). The amphiphilic monomers are dissolved in a mixture solvent at a very low concentration (~0.1mM) to ensure controllable and slow injection.

Fig. 3.3 illustrates a typical synthesis procedure of LAP. First, a stable pentane-water interface is formed in the reactor with the surface below the injection port, with linking reagent dissolved in water. Next, solutions carrying the amphiphilic monomers are slowly injected onto the interface (~10 μL/min) until full coverage is reached. Finally, the pentane is allowed to vaporize completely at room temperature and the 2DP film is accessible for transfer at the air-water interface. The linking reagent are sometimes introduced by a second microsyringe pump system to the water phase after the amphiphilic monomers spread. This double-injection strategy can afford better 2DP quality and is necessary for certain reactions.

There are three major characteristics that sets LAP apart from previous liquid-liquid interfacial methods. First, the pentane phase in LAP acts as an inert buffer layer which does not dissolve any reactants. The pentane-mediated monomer delivery allows for a continuous mass flow of the precursor, which contrasts with dropwise delivery through the air. This allows the surface to remain steady during the entire monomer delivery process, preventing wrinkles and cracks from ripples.

Second, the pentane-water interface facilitates the self-assembly of amphiphilic monomers. The self-assembly behavior ensures a monolayer distribution and an increased local concentration of the monomers, which facilitates the polymerization process. In addition, the self-assembly also provides a template for polymerization, which could help the formation of crystalline domains.

Third, the side-injection arrangement and the monomer self-assembly give rise to laminar flow of the monomer. Because the assembly and spreading of the monomer are restricted by the reactor sidewalls, a constant supply of monomers leads to laminar flow away from the injection region and results in a continuous monolayer assembly and transport at the interface. The laminar transport characteristics limits the oversupply of precursors to the upstream of the monolayer and accommodates potential stress/strain caused by reaction/transport through the fluidity of the assembly.

As discussed above, the successful implementation of LAP requires amphiphilic molecules as monomers, and from the discussion of previous chapters, it is also required the monomer is topologically flat (e.g., a surfactant molecule with long alkyl chains cannot be used as LAP monomers). These two requirements may seem to significantly limit the applicable monomers for LAP. However, as most conjugated planar molecules are hydrophobic and many linkage substituents (e.g. carboxylic acid, amines, aldehydes, etc) are hydrophilic, the combination of them naturally give rise to amphiphilic monomers with hydrophobic cores and hydrophilic peripherals. As a result, potential candidates for LAP are plentiful. For this dissertation, we focus

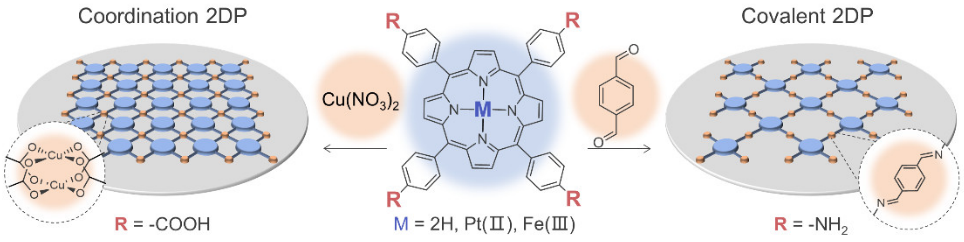

Figure 3.4 Schematic of monolayer 2DP structures and corresponding chemical structures of the molecular precursors.

on amphiphilic monomers with porphyrin cores and various linkage substituents as representative examples. In the next two sections, we will discuss in detail the mechanics of LAP and experimental results of LAP using porphyrin-based monomers (Fig. 3.4). These molecules have two variation sites: one at the center of the porphyrin ring [M = 2H, Fe(III), or Pt(II)] that tunes the optical properties and the other on the phenyl groups (R = -COOH or -NH$_2$) that controlled the monomer-monomer bonds.

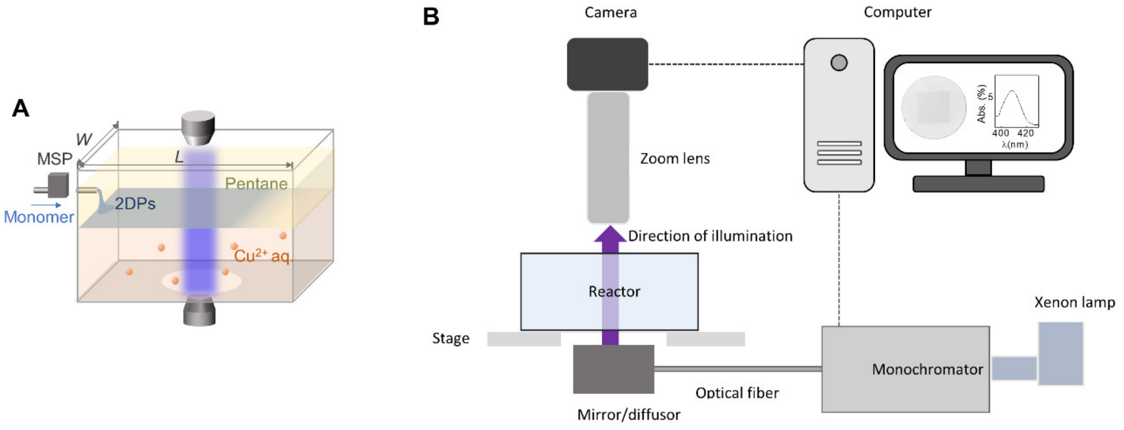

Figure 3.5 In situ optical characterization of the LAP process. **(A)** Schematic of a LAP reactor with in-situ optical characterization apparatus. **(B)** Schematic of in situ optical measurement setup.

3.3 Mechanics of Self-Assembly Guided 2DP growth

We used a home-made in situ optical characterization apparatus to investigate the monomer self-assembly at the interface (Fig. 3.5). To monitor the monomer delivery, assembly, and transport at the interface, we use a monochromic light (bandwidth ~20nm) at the peak absorption of the monomer to for illumination, a long working distance zoom lens for magnification, and an electrically cooled CCD camera for imaging. Figure. 3.6 shows the images taken at the injection area at different injection time in a 1 x 2 inch^2 reactor with 10 μL/min injection rate of 0.1mM 2H-TCPP (M = 2H, R = -COOH) monomer. At the beginning, the delivered monomers are

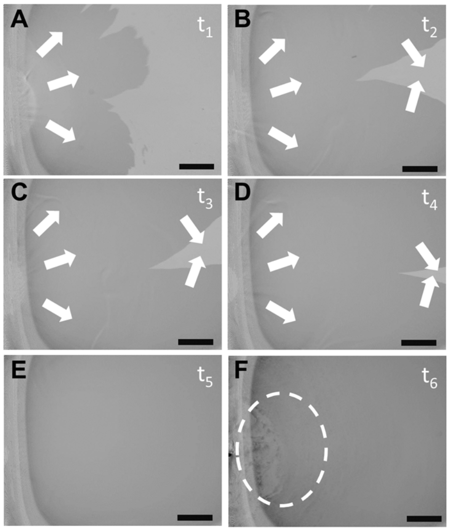

Figure 3.6 Delivery and transport of monolayer film at the injection point. **(A)-(F)** Transmission optical images taken at the injection end of a 1x2 inch^2 reactor with 425nm illumination for 2DP I. t_1 to t_6 indicate the progression in time. The entire injection takes ~1min. Scale bar: 2 mm.

preferentially transported towards the sidewall, forming a void wedge at the center. After a short time, the wedge closes, and entire injection area is covered uniformly with the monomer. Eventually, when excess monomers are injected, particulate aggregates and ripple-like inhomogeneities form, but they are limited only close to the injection area. For the entire injection process, the interface remained stable thanks to the continuous delivery of monomer solutions buffered by the pentane phase.

The uniform contrast of the monomer (dark), which remain the same throughout the entire injection, indicates the self-assembly of the monomer at the interface. We believe that formation of the void wedge and its closure directly resulted from the side-injection geometry. As monomers start to be delivered to the interface, they tend to move randomly towards all directions. However, due to the proximity of the injection wall, most monomer flows are diverted towards the sidewalls, where they are further diverted to the downstream and middle of the reactor. As a result, the flux of monomers is larger at the side than at the middle, leading to the formation of the edge. As the injection continues, more area under the injection port is covered by assembled monomers, leaving no free space for the diverted monomer and the wedge closes.

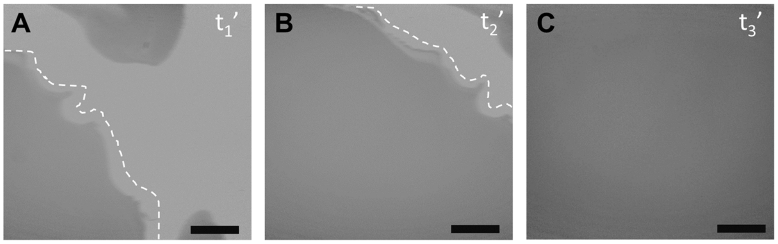

Figure 3.7 Laminar flow of monolayer film transport. (**A**)-(**C**) Transmission optical images taken at the center end of a 1x5 inch^2 reactor with 425nm illumination for 2DP I. t_1' to t_3' indicate the progression in time. The entire injection takes ~1min A steady frontline is indicated by the white dashed line. Scale bar: 2 mm.

At positions further away from the injection area (Fig. 3.7), a steady frontline is observed to pass through the region, indicating laminar flow. The laminar flow allows the monomer assembly to cover a large interface continuously and uniformly, with ideally infinite length and finite width, without mechanical compression. Figure 3.7 also shows that even after excess monomers are injected, no particles or ripples are observed in this region, suggesting the self-limiting feature of LAP. Using 2DP I as an example, the synthesized area of 2DP was measured as a function of the injected volume of the monomer solution (Fig. 3.8). The linear relationship is consistent with a near-unity monomer-to-monolayer growth model, further supporting the formation of self-assembled monolayer and the self-limiting feature of LAP.

By comparison, the injection from the middle of the reactor is significantly different from the side-injection as shown in Fig. 3.9.

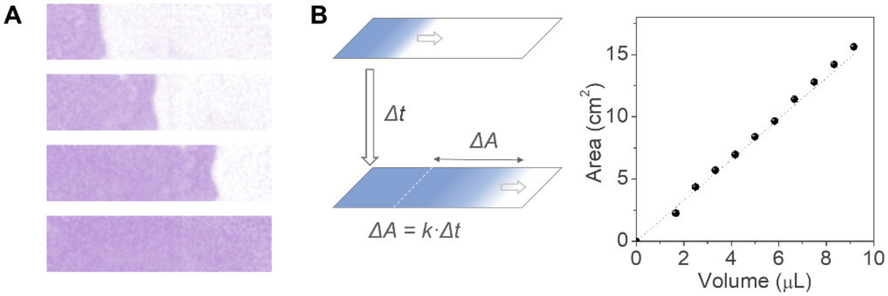

Figure 3.8 Linear growth mode of LAP. (**A**) False-color images of 2DP I film at four different stages during growth. The view size is 6x24 mm^2. (**B**) Left: Schematic of a linear growth model based on LAP. The film area increase linearly with rate constant $k = C_N \cdot A_0 \cdot v \cdot \eta / N_{eff}$, where C_N is number concentration (i.e., the number of molecules per microliter) of the molecular precursor, A_0 is the unit cell area of the 2DP I lattice, v is the volumetric injection rate, η is the monomer-to-monolayer yield, and N_{eff} is the effective layer number. Right: Relation between film area and volume of the injected precursor, measured for 2DP I. The dashed line indicates the theoretical curve for 100% monomer-to-monolayer conversion based on the lattice structure of 2DP I ($\eta = 100\%$, $N_{eff} = 1$).

During the injection, strips and islands are randomly formed at the interface and transported away in all directions. As more monomers are introduced, islands and strips start to crash and merge with each other, leaving cracks, voids, and wrinkles that cannot be reversed.

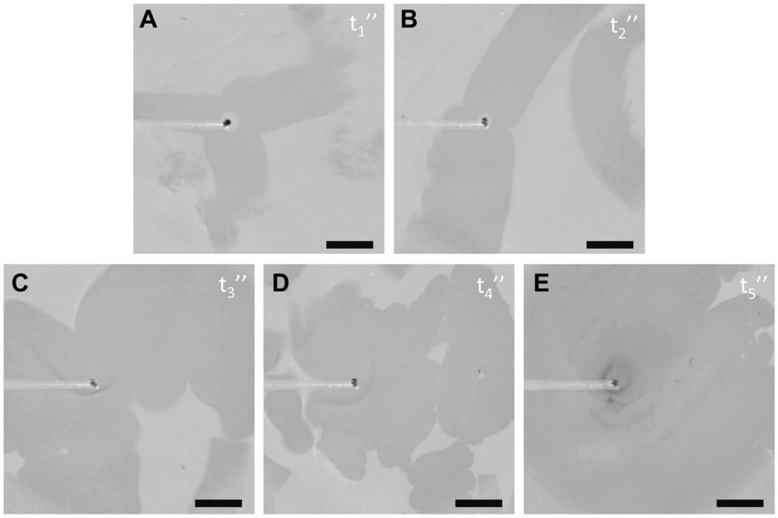

Figure 3.9 Delivery and transport of monomers with center injection. (**A**)-(**E**) Transmission optical images taken at center of a 2x2 inch^2 reactor with 425nm illumination for 2DP I. The bright horizontal line is the injection tubing. t_1'' to t_5'' indicate the progression in time. The entire injection takes ~1min Scale bar: 2 mm.

In summary, the mechanics of LAP is a combination of injection geometry and the self-assembly of amphiphilic monomers at the interface. While self-assembly process of the monomer is a thermodynamically driven process regardless of the injection condition, proper side-injection geometry and continuous monomer delivery are critical to form a uniform and homogeneous 2DP film at large scale, as they are necessary for a unidirectional laminar flow. In the next section, we are going to present LAP's capabilities of synthesizing wafer-scale monolayer 2DPs and lateral heterostructures with detailed characterizations on the quality of the synthesized materials.

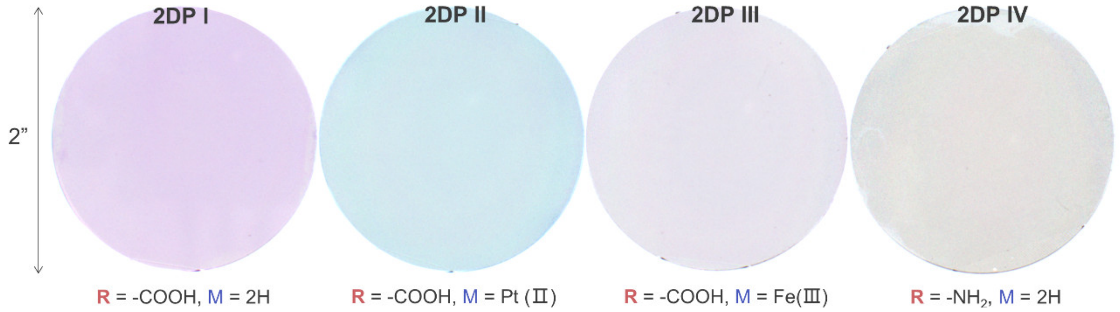

Figure 3.10 False-color images of monolayer 2DPs covering entire 2-inch fused silica wafers. Transmission images taken at the wavelengths of 405, 420, and 440 nm were assigned red, green, and blue channels, respectively, to generate the false-color image. A linear transmission scale of 50 to 95% was applied to all the channels.

3.4 Well-Controlled Synthesis of Diverse 2DP Structures at Wafer-Scale

Fig. 3.10 shows the false-color images of four 2DPs transferred onto 2-inch fused silica substrate. 2DP I-III are synthesized from 5,10,15,20-tetrakis(4-carboxyphenyl)-porphyrin precursors with different metal centers (M-TCPP) and Cu^{2+} ions in the water phase through coordination bonds, while 2DP IV is synthesized from 5,10,15,20-tetrakis(4-aminophenyl)-porphyrin (TAPP) and terephthalaldehyde (TPA) in the water phase through imine bonds (Fig. 3.4). The linkage chemistry for 2DP I-IV were confirmed by Fourier-transform infrared spectroscopy (FTIR) as shown in Fig. 3.11.

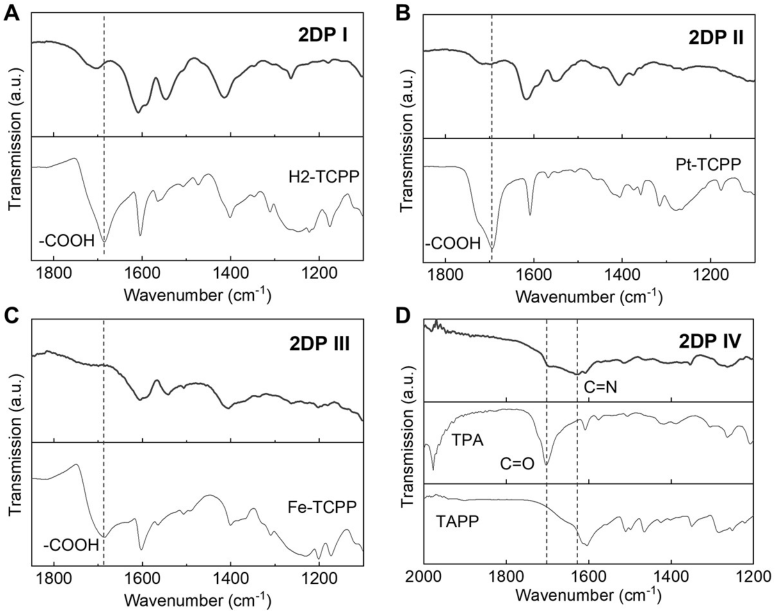

Figure 3.11 FTIR spectra of 2DP I-IV and their corresponding monomers. FTIR spectra of (**A**) 2DP I and H2-TCPP, (**B**) 2DP II and Pt-TCPP, (**C**) 2DP III and Fe-TCPP, and (**D**) 2DP IV, TPA, and TAPP.

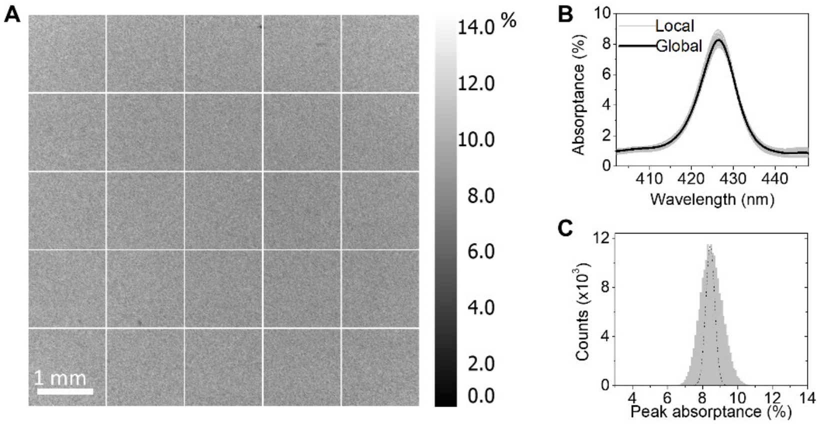

Figure 3.12 Hyperspectral characterization of 2DP I. (**A**) Hyperspectral absorptance image of 2DP I monolayer at the pentane/water interface. (**B**) Absorptance spectra taken for the entire film in view (global) and those of small squares indicated by the white outlines (local). (**C**) Histogram of peak absorptance from all pixels in (A). The dashed line indicates the noise level.

All 2DPs displayed uniform contrast over entire wafers, suggesting macroscopic continuity and homogeneity, which are further confirmed by absorption analysis at higher magnification (Fig. 3.12). By varying the metal centers in coordination-based 2DP I-III, their absorption spectra can be significantly modulated (Fig. 3.13), resulting in markedly different colors shown in Fig. 3.10. In addition, the direct correlation be tween the spectra of the 2DPs and their corresponding porphyrin monomers (Fig. 3.13) indicate that the optical properties of the 2DP films could be directly tuned at the molecular level.

Due to the unique self-assembly and laminar flow of monomers, LAP can be easily scaled up by proper geometry arrangements. As discussed in the previous section, the laminar flow allows almost infinite growth in the flow direction, and the perpendicular dimension can be increased by adding more injection nozzles in parallel. For instance, the 2-inch films shown in Fig. 3.10 were synthesized with three injection nozzles in a 2 (W) x 5 (L) inch^2

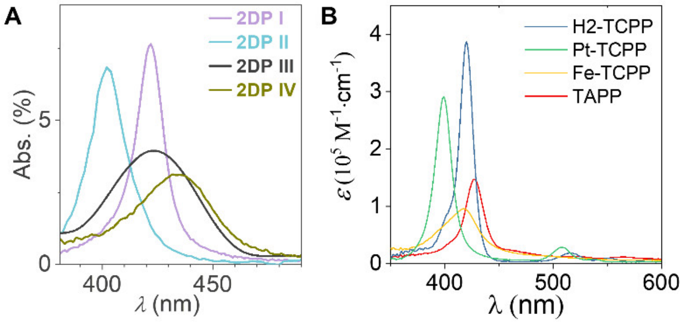

Figure 3.13 UV-Vis spectra of (**A**) 2DP I-IV and (**B**) their corresponding porphyrin-based monomers.

Figure 3.14 Lateral junctions of various 2DPs. (**A**) False-color image of 2DP I/2DP III/2DP II lateral junctions. (Inset) Schematic of generating lateral heterostructures of 2DP I/2DP III/2DP II generated using three nozzles in LAP. (**B**) False-color images of 2DP I/2DP II lateral junctions with tunable stripe widths.

reactor. In addition, with the unidirectional laminar flow, lateral heterojunctions of monolayer 2DPs can be grown with tunable compositions and widths by introducing different monomers from each injection nozzle and by controlling the relative injection rates (Fig. 3.14). Sharp interfaces between adjacent monolayer stripes were observed without voids or interdiffusion, which is a direct result of the laminar flow.

All four 2DP films show a homogeneous thickness of ~1 nm, which is consistent with the expected thickness of a monolayer[15], with a uniform and smooth surface as measured by atomic force microscopy (AFM) (Fig. 3.15). Despite the monolayer thinness, the 2DP films synthesized by LAP exhibit considerable mechanical strength and can be transferred onto various substrates as continuous films without cracking as shown in Fig. 3.10. As an additional example, a

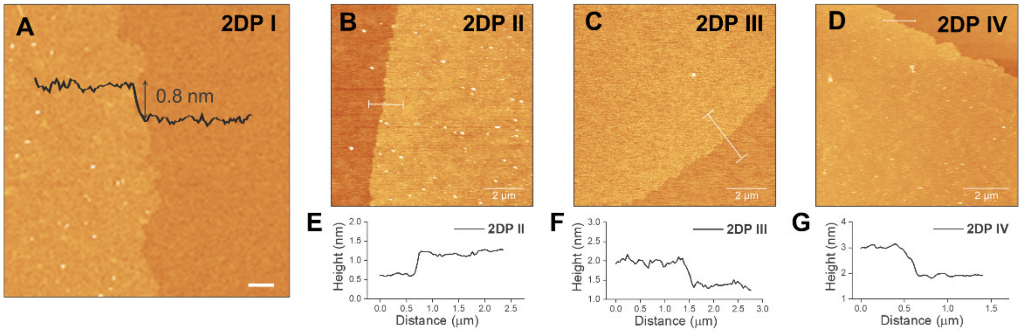

Figure 3.15 AFM characterizations of 2DP I – IV. (**A**) 2DP I (inset: AFM height profile; scale bar: 500 nm), (**B**) 2DP II, (**C**) 2DP III, and (**D**) 2DP IV. (**E**) – (**G**) AFM height profiles for 2DP II – IV.

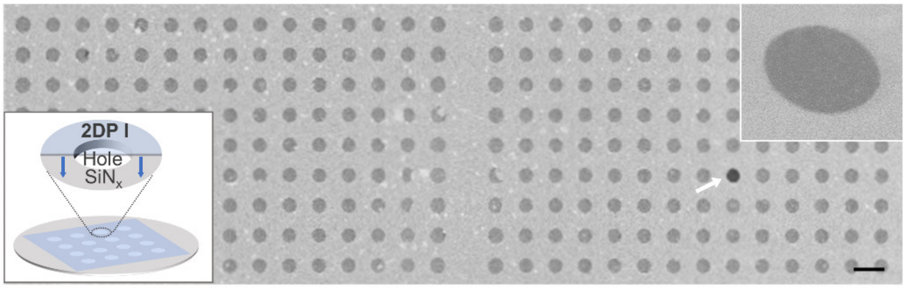

Figure 3.16 SEM image of monolayer 2DP I on a holey silicon nitride TEM grid. The white arrow indicates a hole not covered by monolayer 2DP I. Scale bar, 5 μm. (Bottom left inset) Schematic of monolayer 2DP I suspended over a hole on a silicon nitride TEM grid. (Top right inset) Magnified SEM image of monolayer 2DP I suspended over a 2-μm hole.

scanning electron microscopy (SEM) image of a 2DP I film transferred and suspended over a holey transmission electron microscope (TEM) grid (2 μm diameter holes; Fig. 3.16) displays an array of freestanding 2DP membranes. These membranes were suspended with a near perfect yield (> 99%; one broken membrane denoted by an arrow) and appeared uniform and continuous over the entire area without crack s or voids. Such mechanical strength is the foundation for membrane-related applications for 2DPs, which will be discussed in detail later in Chapter 5 with osmotic power generation as an example.

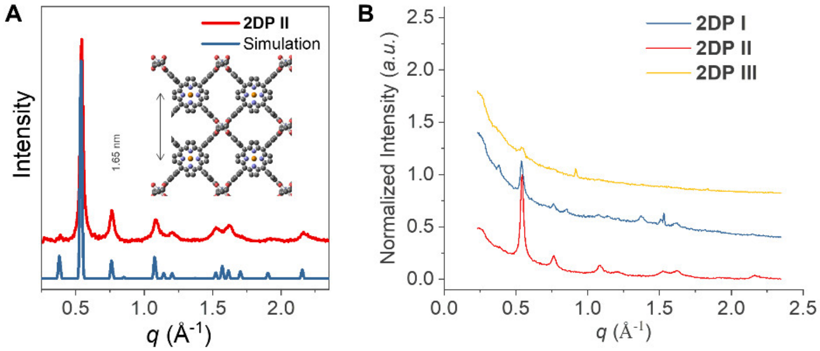

Figure 3.17 GIXRD pattern of LAP synthesized 2DPs. (**A**) Experimental and calculated in-plane XRD profiles for 2DP II. The experiment was conducted on a stacked 2DP II of 147 layers on sapphire. (Inset) Crystal structure of 2DP II. (**B**) Unprocessed in-plane GIXRD intensity profiles of 2DPs. Measurements were done on stacked samples (2DP I: 40 layers; 2DP II: 147 layers; 2DP III: 37 layers) to increase signal intensity.

Despite the room temperature synthesis and short reaction time (~30min), the coordination-based 2DP I-III are polycrystalline and show clear diffraction peaks in the synchrotron grazing incidence X-ray diffraction (GIXRD) spectra after repeated stacking to enhance scattering (Fig. 3.17). Using 2DP II as an example, the in-plane XRD pattern showed all the main peaks predicted based on the structure model (inset in Fig. 3.17), with an average lateral domain size estimated to be ~20 nm according to Scherrer equation. The observed crystallinity likely results from the combination of the reversibility of the copper-carboxylate coordination bonds and the templation of monomer self-assembly, which has been observed in other systems[5,16].

Moreover, the crystalline structure of 2DP II monolayers was confirmed with scanning tunneling microscopy (STM) performed under ultra-high vacuum after transferred onto Au(111) on mica substrate. The STM topography image in Fig. 3.18A showed a square lattice with a single-crystalline domain that fully covered the 30 nm by 30 nm area (2D fast Fourier transform (FFT) image shown in Fig. 3.18A inset). Another STM image (Fig. 18B; 60 nm by 60 nm) displayed three primary crystalline orientations with a lattice constant *a* = 1.66 ± 0.03 nm (measured from

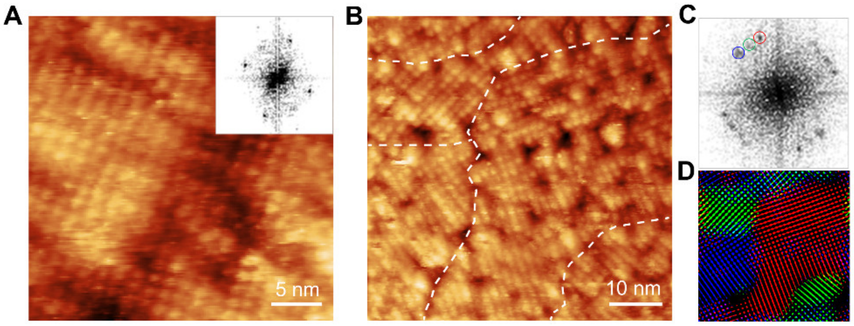

Figure 3.18 STM topography images of monolayer 2DP II. (**A**) Constant-current STM topography image of a single-crystalline domain of monolayer 2DP II on a thin film of Au(111) on mica. (Inset) 2D FFT of the image. (**B**) Constant-current STM topography image of multiple-crystalline domains of monolayer 2DP II. Boundaries between different domains are manually identified by the white dashed line. (**C**) 2D FFT of (B) showing square lattices of three major orientations. (**D**) Color-coded inverse 2D FFT image generated using the three sets of square lattice spots in (C). One spot from each set is circled with the corresponding color in (C).

Fig. 3.18C). The lattice constant extracted from these microscopic STM analyses is close to that from GIXRD measurements (1.64 nm) performed on the macroscopic scale (0.1 mm by 10 mm) with a mismatch less than 2%. Fig. 3.18D shows a composite inverse 2D FFT image where each colored region corresponds to one lattice orientation. The domain size estimated from Fig. 3.18D (between 10 and 40 nm) is consistent with that from the Scherrer equation with domain boundaries marked by dashed lines. For the imine-based 2DP IV, no evidence for long-range order could be collected (through GIXRD or selected area electron diffraction), similar to other monolayer covalent 2DPs reported previously[17].

3.5 Summary

In this chapter, we introduced a novel interfacial synthesis method, namely laminar assembly polymerization (LAP), that can generate wafer-scale continuous and homogeneous 2DP films using different monomers and linkage chemistries. The LAP differs from previous liquid-liquid interfacial methods by utilizing a pentane phase that does not dissolve any reactants but only facilitate continuous monomer distribution and interfacial self-assembly. With amphiphilic monomers and side-injection arrangement, it eliminates the requirement for mechanical compression in LB deposition and achieves precise monolayer control and large-scale film synthesis by self-assembly of monomers and unidirectional laminar flow. The synthesized 2DP films are mechanically robust and polycrystalline, which likely benefits from the templation of monomer self-assembly.

3.6 References

1. Evans, A. M. *et al.* Two-Dimensional Polymers and Polymerizations. *Chem. Rev.* **122**, 442–564 (2022).
2. Feng, X. & Schlüter, A. D. Towards Macroscopic Crystalline 2D Polymers. *Angew.*

Chemie - Int. Ed. **57**, 13748–13763 (2018).

3. Mak, K. F. & Shan, J. Semiconductor moiré materials. *Nat. Nanotechnol.* **17**, 686–695 (2022).

4. Colson, J. W. & Dichtel, W. R. Rationally synthesized two-dimensional polymers. *Nat. Chem.* **5**, 453–465 (2013).

5. Makiura, R. *et al.* Surface nano-architecture of a metal-organic framework. *Nat. Mater.* **9**, 565–571 (2010).

6. Dong, R., Zhang, T. & Feng, X. Interface-Assisted Synthesis of 2D Materials: Trend and Challenges. *Chem. Rev.* **118**, 6189–6325 (2018).

7. Sheberla, D. *et al.* High electrical conductivity in Ni3(2,3,6,7,10,11-hexaiminotriphenylene)2, a semiconducting metal-organic graphene analogue. *J. Am. Chem. Soc.* **136**, 8859–8862 (2014).

8. Dong, R. *et al.* Large-Area, Free-Standing, Two-Dimensional Supramolecular Polymer Single-Layer Sheets for Highly Efficient Electrocatalytic Hydrogen Evolution. *Angew. Chemie Int. Ed.* **54**, 12058–12063 (2015).

9. Sahabudeen, H. *et al.* Wafer-sized multifunctional polyimine-based two-dimensional conjugated polymers with high mechanical stiffness. *Nat. Commun.* **7**, 13461 (2016).

10. Dong, R. *et al.* High-mobility band-like charge transport in a semiconducting two-dimensional metal–organic framework. *Nat. Mater.* **17**, 1027–1032 (2018).

11. Bauer, T. *et al.* Synthesis of Free-Standing, Monolayered Organometallic Sheets at the Air/Water Interface. *Angew. Chemie* **123**, 8025–8030 (2011).

12. Matsumoto, M. *et al.* Lewis-Acid-Catalyzed Interfacial Polymerization of Covalent Organic Framework Films. *Chem* **4**, 308–317 (2018).

13. Müller, V. *et al.* Structural Characterization of a Covalent Monolayer Sheet Obtained by Two-Dimensional Polymerization at an Air/Water Interface. *Angew. Chemie - Int. Ed.* **56**, 15262–15266 (2017).

14. Wang, W. & Schlüter, A. D. Synthetic 2D Polymers: A Critical Perspective and a Look into the Future. *Macromol. Rapid Commun.* **40**, 1800719 (2019).

15. Motoyama, S., Makiura, R., Sakata, O. & Kitagawa, H. Highly crystalline nanofilm by layering of porphyrin metal-organic framework sheets. *J. Am. Chem. Soc.* **133**, 5640–5643 (2011).

16. Makiura, R. & Konovalov, O. Interfacial growth of large-area single-layer metal-organic framework nanosheets. *Sci. Rep.* **3**, 2506 (2013).

17. Cardenas, L. *et al.* Synthesis and electronic structure of a two dimensional π-conjugated polythiophene. *Chem. Sci.* **4**, 3263 (2013).

Chapter 4: Van der Waals Heterostructures from 2DPs and inorganic 2D materials

4.1 Introduction

One of the most intriguing properties of 2D materials is the dangling-bond free surface that enables arbitrary assembly of dissimilar materials without the constraint of lattice matching. The layer-by-layer integration of 2D materials is commonly referred to as van der Waals (vdW) integration, as different layers only interact through weak vdW forces, allowing easy manipulation of individual layers through transfer-based techniques[1–3]. By tuning the permutation and composition of individual layers, thousands of distinct vdW heterostructures can be made from just a few monolayers, allowing for materials design/engineering with atomic precision. In addition, the rotational alignment between layers can also significantly influence the characteristics of vdW heterostructures, leading to exotic phenomena and properties in homo- and hetero- vdW heterostructures with precisely controlled interlayer rotation angles[4].

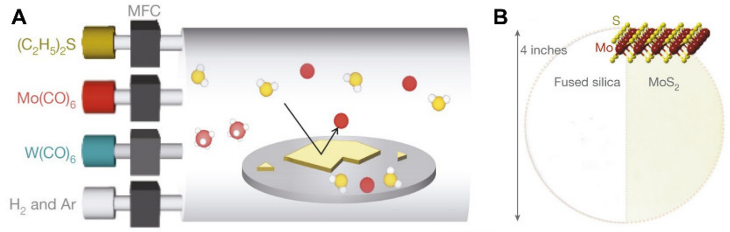

Figure 4.1 Large-scale monolayer TMD synthesis using MOCVD. (**A**) Schematic of the MOCVD setup. (**B**) Optical image of homogeneous monolayer MoS_2 (right half) grown on 4-inch fused silica substrate (left half for comparison). Inset: the structure of monolayer MoS_2.

Until recently, vdW integration has been exclusive to inorganic 2D materials, mainly due to the lack of precise monolayer synthesis for 2DPs and their fragility for integration. In addition, most vdW heterostructures are demonstrated with micron-sized exfoliated 2D crystals, which significantly limits their practical applications. In 2015, our group developed a method for growing wafer-scale transition metal dichalcogenides

(TMDs) by metal-organic chemical vapor deposition (MOCVD)[5] (Fig. 4.1). Based on the high-quality and large-scale TMD materials, our group further demonstrated wafer-scale layer-by-layer integration of TMD monolayers with pristine interfaces by using a vacuum environment in 2017[6] (Fig. 4.2). These two advances mark a critical step towards the practical applications of 2D materials and vdW heterostructure, and build the foundation for many later works on large-scale 2D materials growth and vdW integration.

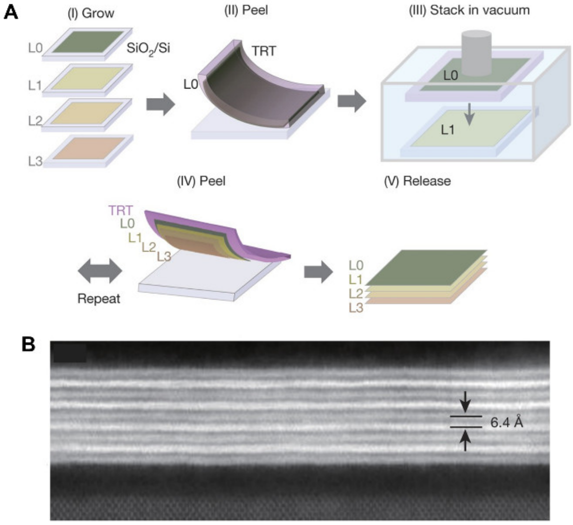

Figure 4.2 Layer-by-layer vacuum stacking of monolayer TMD materials. (**A**) Schematic of the vacuum stacking procedures. (**B**) Cross-sectional ADF STEM image of a MoS_2/WS_2 superlattice fabricated using the vacuum stacking method.

With LAP, the capability of large-scale vdW integration, for the first time, were extended to organic 2D materials. With precise monolayer control and large area synthesis, LAP is compatible with the previous developed inorganic materials and their layer-by-layer integration technique in our group. Compared to inorganic 2D materials, organic 2D materials, or 2DPs, have greater structural varieties and chemical functionalities through rational molecular design, which can potentially enhance the performance of 2D electronics, optoelectronics, and sensors[7,8]. Moreover, in the context of rising moiré physics with 2D material, 2DPs, with their wide range of lattice topologies and large lattice constants (~10X that of inorganic ones), are likely to host interesting physics when combined with inorganic 2D materials.

In this chapter, we will discuss in detail how LAP is combined with the toolboxes originally developed for inorganic 2D materials to generate large-scale hybrid vdW heterostructures. Specifically, water-based transfer technique is combined with vacuum-based dry peeling approaches to accommodate the distinct mechanical properties of 2DPs and TMDs. Programmable 2DP/MoS_2 superlattices are fabricated using the combined approaches with micro-, meso-, and macro-scale characterizations confirming the high quality of the interfaces. Moreover, as a proof-of-concept demonstration, capacitor arrays made from 2DP/MoS_2 superlattices are demonstrated using a non-perturbative device fabrication process that are general to fragile and sensitive organic 2D materials.

4.2 Transfer-Based Integration of 2DPs and Inorganic 2D Materials

With lower in-plane bond density and strong out-of-plane $\pi - \pi$ stacking, it is challenging to isolate intact monolayer 2DPs from their bulk crystals[9,10]. Using LAP, large-scale monolayer 2DPs are directly synthesized at a pentane-water interface. In addition, as no monomers are dissolved in the pentane phase, the volatile pentane can be easily removed by evaporation leaving the monolayer 2DP at an air-water interface with almost no residue or contamination. The monolayer 2DP can be easily accessed at the air-water interface for patterning and transfer, making LAP an ideal platform for the integration of 2DPs.

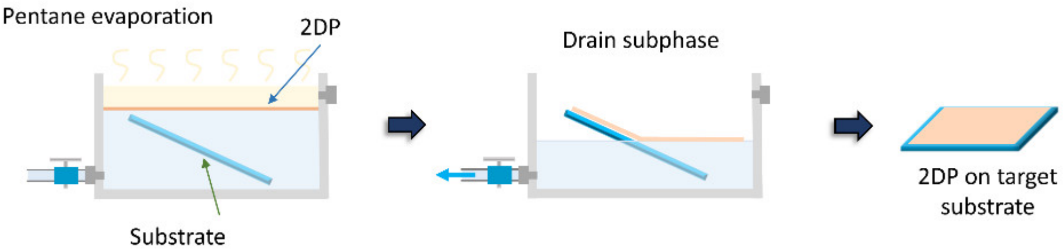

Figure 4.3 Schematic of 2DP transfer by water draining.

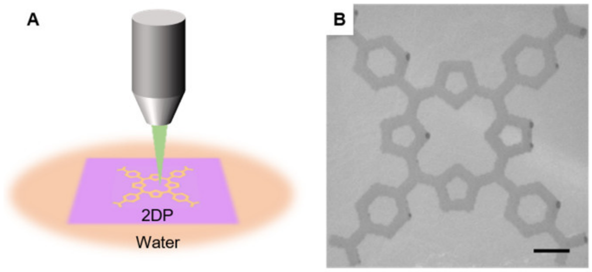

Figure 4.4 Laser patterning of 2DPs. (**A**) Schematic of patterning 2DP monolayers on the water surface. (**B**) Optical reflection of laser-patterned 2DP I at the wavelength of 420 nm. Scale bar: 1mm.

Due to the monolayer and fragile nature of the 2DPs, we designed a water-based transfer process that allows reliable large-scale transfer of 2DPs to arbitrary substrates (Fig. 4.3). Before the LAP process, a substrate is placed in the subphase at a small tilt angle (~15°). After polymerization of the 2DP film, the pentane is allowed to evaporate at room temperature leaving the 2DP film at the air-water interface. The subphase is then drained at a controlled rate to slowly transfer the 2DP film onto the substrate by lowering the water level. The slow draining process allows for a steady transfer of the film and the small tilt angle prevents any water from being trapped between the film and the substrate.

While on the water surface, the 2DP film can be easily patterned using lasers (Fig. 4.4). For instance, Fig. 4.4B shows a reflection image of 2DP I film (taken at its peak absorption wavelength of 420nm) patterned by a pulsed 532nm laser at the air-water interface right after the polymerization, where the dark contrast indicates the film has been removed. Thanks to the large-scale and mechanical robustness, the film shows no distortion of the pattern or collapsing after the laser patterning. This is further demonstrated by the patterning and transfer of the stripy

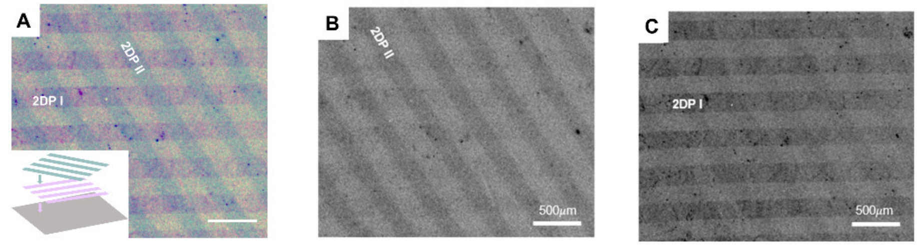

Figure 4.5 Transfer of patterned 2DPs. (**A**) False-color image of overlapped **2DP I** and **2DP II** stripes. Scale bar, 500 µm. Transmission optical images of the heterostructure at (**B**) 400 nm and (**C**) 425 nm.

feature on the 2DP films shown in Fig. 4.5. First, the 2DP film transferred onto a transparent fused silica substrate from the air-water interface after parallel stripes were created by the 532 laser. Second, the transferred 2DP film was submerged in the subphase and used as a new substrate for the transfer of a newly grown 2DP film. Last, new 2DP film was patterned with parallel stripes of a different orientation and transferred onto the underlying substrate. As shown in Fig. 4.5 the stripes in 2DP films remained parallel after the transfer and their orientation was unchanged before and after the transfer.

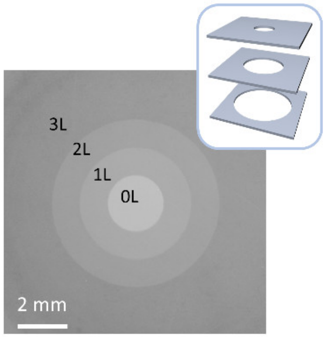

Figure 4.6 Transmission optical images of 3 layers of 2DP I with laser-patterned concentric circles. Inset: schematic of the layer and pattern arrangement.

In addition to in situ patterning on the water surface, the 2DP films can also be patterned after transferred to a target substrate. Shown in Fig. 4.6 is a set of concentric circles made of 3 layers of 2DPs, which were laser-patterned after transfer. It demonstrates the homogeneity of the 2DP films and the reliability of our water-based transfer technique.

However, our water-based transfer-technique is not as versatile as the dry peeling/stacking method that is commonly used for inorganic 2D materials[6,11]. Due to the abundant oxyphilic groups and weak bonding capping ligand (e.g. H_2O and pyridine), 2DPs tends to adhere to the underlying substrate more strongly than inorganic 2D materials with perfectly saturated in-plane bonding. Moreover, 2DPs usually have weaker in-plane mechanical strength due to weaker bonds and lower bond density. As a result, the dry peeling/stacking method can’t be directly applied to 2DPs, which limits their application in vdW heterostructure fabrication.

To overcome this limitation, we combine 2DP with MOCVD-grown TMD materials, which can be easily delaminated from the growth substrate due to the weak vdW interaction. For instance, if a 2DP/MoS_2 bilayer heterostructure is formed, the bilayer can be easily separated from the substrate either through water delamination or PMMA dry peeling. With the large-scale MoS_2 synthesis previously developed in our group[5], such bilayer should be easily made by using MoS_2 on its growth substrate as the transfer target for the water-based 2DP transfer (Fig. 4.3). However, the interaction between the MoS_2 and the substrate is so weak that it is delaminated by surface tension of water upon dipping into the water phase, preventing it to be used to as the transfer target in the water subphase. In order to place the MoS_2 into the subphase, we first cover the MoS_2 surface with methanol, which is water-miscible and has lower surface tension than water. Upon submerging into the water phase, the methanol provides a buffer and prevent the MoS_2 from being delaminated by the water surface tension. For all our experiments, the small amount of methanol didn't alternate the spreading and assembly of the porphyrin-based monomers.

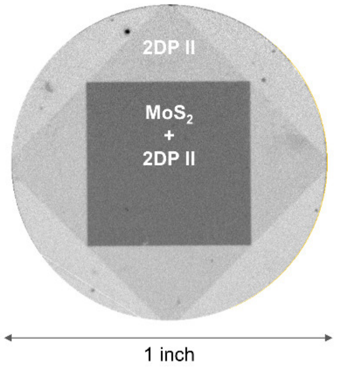

Figure 4.7 Optical transmission image of a 2DP II/MoS_2 heterostructure on fused silica taken at the wavelength of 405 nm.

With the methanol protection, we were able to generate large scale 2DP/MoS_2 bilayer heterostructures as shown in Fig. 4.7. Those bilayer heterostructures can be easily delaminated from the substrate as designed, and their application as building blocks for programmable vdW heterostructure fabrication is discussed in detail in the next section.

4.3 Fabrication of Programmable 2DP/MoS$_2$ Superlattices

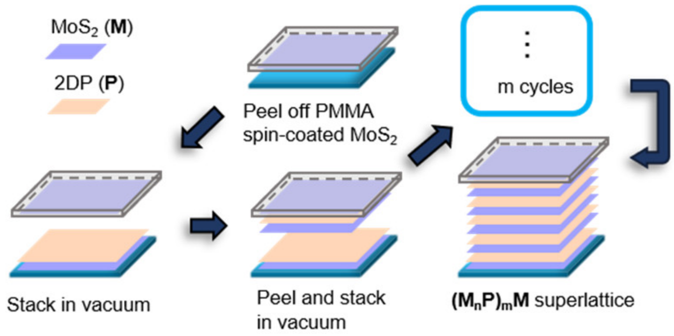

Figure 4.8 Schematic of fabricating programmable 2DP/MoS$_2$ superlattices.

The 2DP/MoS$_2$ bilayer is compatible with most vdW integration techniques, and hence, can be considered a new component for vdW integration. With slight modification to a previously developed vacuum stacking method[6], we can generate various 2DP/MoS$_2$ superlattices using 2DP/MoS$_2$ bilayers and MoS$_2$ monolayers (Fig. 4.8). The fabrication starts from an initial monolayer MoS$_2$ (L_0). Poly-methyl methacrylate (PMMA) is first spin-coated onto L_0 to provide mechanical support and facilitate the delamination. After baking the sample at 180°C, a piece of thermal release tape (TRT) is applied onto the sample and mechanically peeled off the growth substrate with PMMA and L_0 on it. The fabricated *TRT/PMMA/* L_0 is mounted onto the top pressor of a vacuum stacking apparatus and another as-grown monolayer MoS$_2$ film or 2DP/MoS$_2$ heterostructure film is placed on the bottom stage of the vacuum chamber which is maintained at 100 °C. The vacuum chamber was then evacuated to less than 100 mTorr, and the pressor was lowered through a linear motion vacuum feed-through to bring *TRT/PMMA/* L_0 into contact with the film on the bottom stage. The resulting stack was taken out from the vacuum chamber and heated at 120 °C under ambient

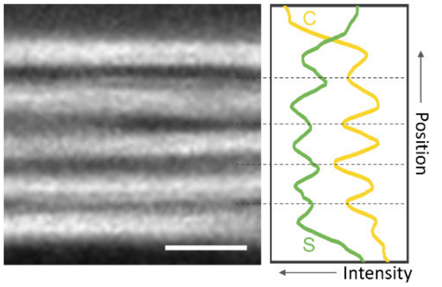

Figure 4.9 STEM images of a 2DP/(MoS$_2$)$_2$ superlattice. Left: Cross-sectional ADF STEM image of a 2DP III/(MoS$_2$)$_2$ superlattice film transferred onto a SiO$_2$/Si substrate. Each bright layer consists of two layers of MoS$_2$ stacked, and each dark layer is a 2DP III monolayer. Right: EELS profiles of carbon and sulfur taken from a different area on the sample. Scale bar, 5 nm.

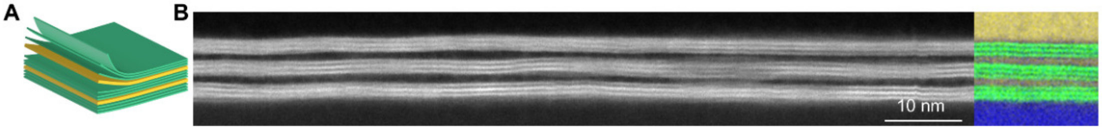

Figure 4.10 (**A**) Schematic and (**B**) STEM image of a 2DP/$(MoS_2)_3$ superlattice. Left: Cross-sectional ADF STEM image of a 2DP II/$(MoS_2)_3$ superlattice film transferred onto a SiO_2/Si substrate. Each bright band consists of three MoS_2 monolayers, and each dark layer between the bands is a monolayer 2DP II. Right: Composite image of carbon (yellow) and oxygen (blue) EELS mapping and ADF STEM signal (green) taken from

condition to release the *TRT*. A new *TRT* was then used to mechanically detach the whole stack from the growth substrate. The whole process can then be repeated with either as-grown monolayer MoS_2 or 2DP/MoS_2 bilayers to generate stacked films of arbitrary layer number, composition, and permutation. Finally, the top PMMA layer can be removed using solvents like chloroform, leaving a clean top surface. In addition, the 2DP/MoS_2 bilayer building block can be extended to any heterostructures of $(2DP)_n/(MoS_2)_m$ through a combination of water-based 2DP transfer and vacuum stacking, making the approach highly programmable. Due to the weak interaction between 2DPs and MoS_2, the stacked film sometimes tends to cleave at the 2DP-MoS_2 interface rather than detaching from the substrate. To avoid this problem, water is dropped around the sample to utilize the surface tension for peeling when a 2DP-MoS_2 interface is present.

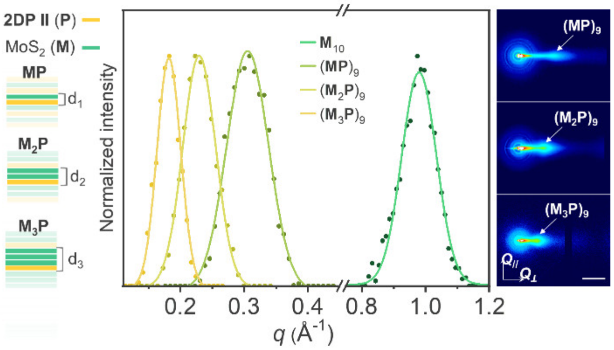

Figure 4.11 Programmable 2DP/$(MoS_2)_m$ superlattices. Left: Structures of 2DP II/$(MoS_2)_m$ vertical superlattices. Middle: Normalized diffraction peaks corresponding to 2DP II /$(MoS_2)_m$ superlattices measured by GIWAXS. Right: 2D GIWAXS scattering patterns of 2DP II/$(MoS_2)_m$ superlattices. Scale bar, 0.2 Å^{-1}.

Fig. 4.9 shows a cross-sectional annular dark field (ADF) scanning transmission electron microscopy (STEM) image of a 2DP III/$(MoS_2)_2$ superlattice and the corresponding electron energy loss spectroscopy (EELS) profiles of carbon and sulfur. The five bright bands correspond to the MoS_2 bilayers while the dark bands in between are the 2DP III monolayers, with EELS confirming the composition of each constituent layers. In addition, the programmability of the 2DP/MoS_2 superlattice is demonstrated in Fig. 4.10 with a hybrid superlattice made of repeating 2DP/$(MoS_2)_3$ building units. Each bright band shown in the image consists of three layers of MoS_2, and the dark layer in between corresponds to a 2DP II monolayer, with the EELS mapping shown next to the image. The films are parallel to each other with sharp interfaces and uniform layer thickness over the entire 100 nm view of the ADF STEM image, indicating a high level of uniformity.

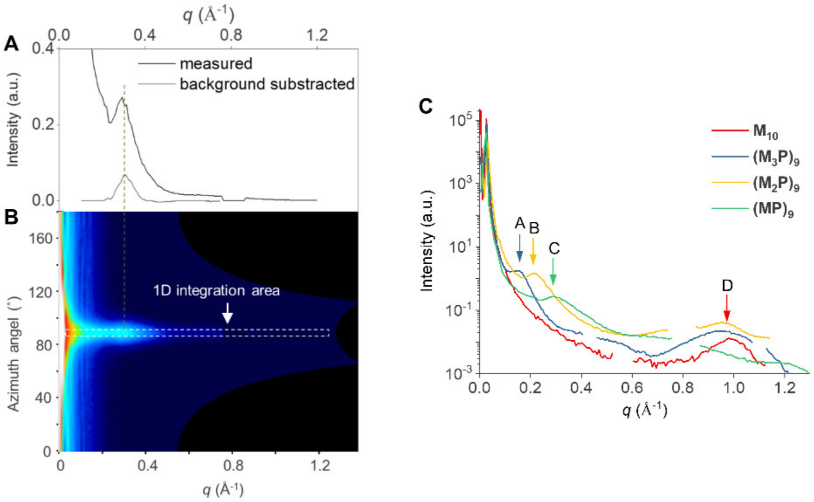

Figure 4.12 GIWAXS spectra of different 2DP/$(MoS_2)_m$ superlattices. (**A**) Integrated 1D line profile from the dash line box area in (**B**) Polar transformation of 2D GIWAXS pattern of $(MP)_9$. (**C**) GIWAXS spectra of different 2DP II/$(MoS_2)_m$ superlattices. The arrows indicate the peaks corresponding to the superlattices used for Gaussian fitting in Fig. 4.11.

The programmability of the 2DP/MoS_2 superlattices with different 2DP/$(MoS_2)_m$ building units are demonstrated with a series of superlattices with $m = 1, 2$, or 3. Fig. 4.11 (left) shows a series of vdW superlattices with varied superlattice periodicity d made of 2DP II/$(MoS_2)_m$. The grazing incidence wide-angle x-ray scattering (GIWAXS) data presented in Fig. 4.11 (middle and right)

Peak position	Superlattice	d-spacing (Å)
A	**$(M_3P)_9$**	34.5
B	**$(M_2P)_9$**	27.5
C	**$(MP)_9$**	20.7
D	**M_{10}**	6.4

Table 4.1 Lattice constants of different 2DP II/(MoS2)$_m$ superlattices obtained from GIWAXS.

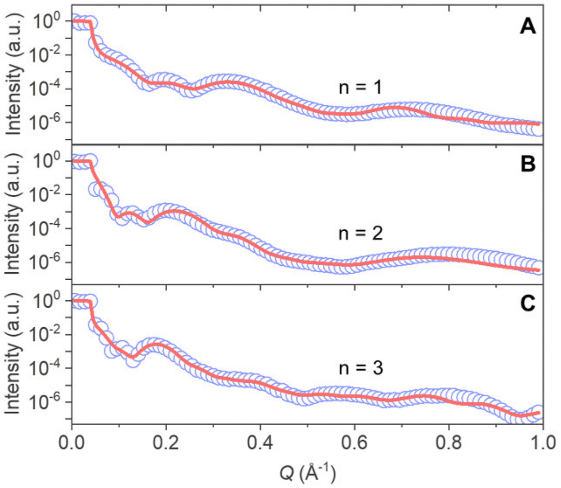

Figure 4.13 X-ray reflectivity (XRR) spectra of different $(MoS_2)_n$/2DP II/$(MoS_2)_n$/2DP II/$(MoS_2)_n$ superlattice on sapphire substrates. (**A**) XRR spectrum of n=1. (**B**) XRR spectrum of n=2. (**C**) XRR spectrum of n=3.

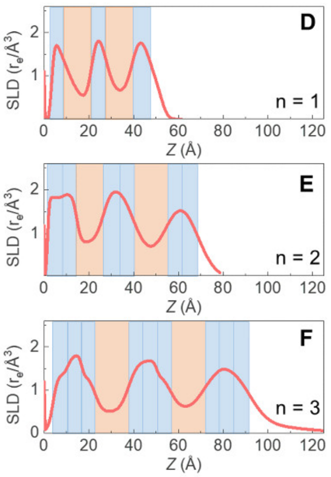

Figure 4.14 Scattering length density profiles of different $(MoS_2)_n$/2DP II/$(MoS_2)_n$/2DP II/$(MoS_2)_n$ superlattice on sapphire substrates. Line profile of scattering length density along the vertical direction for (**A**) n=1, (**B**) n=2, and (**C**) n=3.

show the distinctive diffraction peak for each superlattice. For all the superlattices, the diffraction peaks appeared only along the out-of-plane direction indicating films within the superlattices are all parallel to each other. By radially integrating the 2D GIWAXS images along the out-of-plane direction, 1D spectra were obtained in reciprocal space and used to measure d (Fig. 4.12). For example, the superlattice with $n = 3$ showed $d = 3.5$ nm and a vdW thickness of 1.5 nm for 2DP II, consistent with the value measured from Fig. 4.10. The results from other superlattices agreed very well with the predicted values as well (Fig. 4.12C and Table 4.1).

In addition, the large footprint of GIWAXS measurement (0.5 X 10 mm) indicates large-scale uniformity of the vacuum stacked superlattice. The uniformity and alternating structure of 2DP/$(MoS_2)_m$ ($m = 1, 2,$ or 3) superlattices are further characterized by X-ray reflectivity (XRR) measurements. In all measurements, the direct reflection beam shows oscillations of intensity

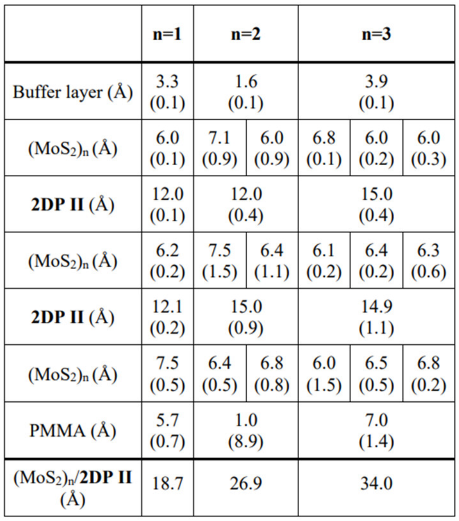

	n=1	n=2		n=3		
Buffer layer (Å)	3.3 (0.1)	1.6 (0.1)		3.9 (0.1)		
(MoS$_2$)$_n$ (Å)	6.0 (0.1)	7.1 (0.9)	6.0 (0.9)	6.8 (0.1)	6.0 (0.2)	6.0 (0.3)
2DP II (Å)	12.0 (0.1)	12.0 (0.4)		15.0 (0.4)		
(MoS$_2$)$_n$ (Å)	6.2 (0.2)	7.5 (1.5)	6.4 (1.1)	6.1 (0.2)	6.4 (0.2)	6.3 (0.6)
2DP II (Å)	12.1 (0.2)	15.0 (0.9)		14.9 (1.1)		
(MoS$_2$)$_n$ (Å)	7.5 (0.5)	6.4 (0.5)	6.8 (0.8)	6.0 (1.5)	6.5 (0.5)	6.8 (0.2)
PMMA (Å)	5.7 (0.7)	1.0 (8.9)		7.0 (1.4)		
(MoS$_2$)$_n$/**2DP II** (Å)	18.7	26.9		34.0		

Table 4.2 Summary of the thickness of the individual layers in (MoS2)$_n$/2DP II/(MoS2)$_n$/2DP II/(MoS2)$_n$ (n = 1, 2, or 3) from the XRR fitting. Errors presented in the parentheses are calculated as a 5% increase in the optimal Figure of Merit from the simulation.

when incident angle is scanned. These oscillations directly confirm that the superlattices have layered vertical structures. The features of these oscillations also change with *m*, which indicates that the periodicity and other superlattice structures are directly tuned by the 2DP/(MoS$_2$)$_m$ building blocks. The simulations based on our proposed superlattice structures proved excellent fits to the XRR spectra (Fig. 4.13), suggesting the successful fabrication of the designed superlattice structures. Moreover, the scattering length density profiles generated from fitting the XRR spectra clearly reveal the oscillations of electron density consistent with the alternating structures of (MoS$_2$)$_m$ and 2DP II (Fig. 4.14). The thickness of the repeating units extracted from the XRR analysis matches those obtained from GIWAXS and cross-sectional STEM within 2Å mismatch (Table 4.2). Both the GIWAXS and the XRR data were taken from a macroscopic area randomly chosen from 1 cm by 1 cm superlattice films, illustrating the homogeneity of the vdW superlattices on a large scale.

4.4 Non-Perturbative Device Fabrication with 2DP/MoS$_2$ Superlattices

The programmable vdW superlattices and heterostructures provide a powerful platform for fabricating electronic/optoelectronic devices whose properties are engineered layer by layer. Specifically, the semiconducting monolayer MoS$_2$ can serve as electron channels while the chemical versatile 2DPs can introduce functionalities for sensing, catalysis, and/or photochemical gating.

However, it has been shown that conventional device fabrication processes, such as metal evaporation and sputtering, can deteriorate the structural integrity of 2D materials, introducing defects and amorphousness[12]. This problem becomes even more severe when 2DPs are involved in the process. Due to the weaker chemical bonds and intrinsic porosity, 2DPs are susceptible to various degradations during the conventional photolithography and deposition processes. For instance, the basic pH of many common developer solutions can break most coordination bonds and hydrolyze many covalent linkages for 2DPs. Not to mention that the energetic metal atoms from deposition processes can easily break the 2DP film, and cause pinhole or short-circuit due to the intrinsic porosity.

In order to utilize the chemical versatility of 2DPs for electronic/optoelectronic devices, we developed a non-perturbative device fabrication process, which uses transfer-based vdW integration techniques and is compatible with our 2DP/MoS_2 superlattice fabrication. Fig. 4.15 illustrates the procedure of this method.

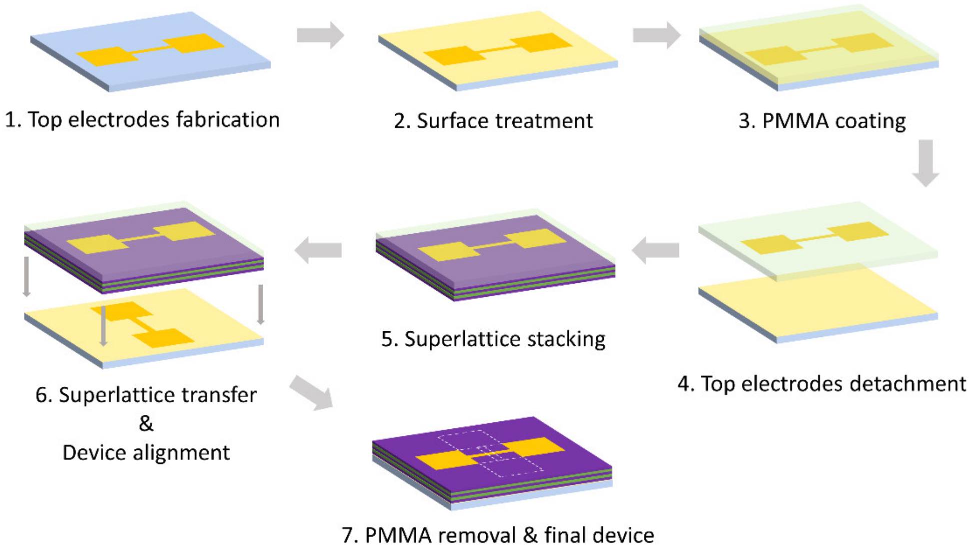

Figure 4.15 Procedures of the non-perturbative device fabrication for 2DP/MoS_2 superlattices.

Step 1. Top electrodes were fabricated using standard photolithography process followed by e-beam evaporation of 50 nm Au on a SiO_2/Si wafer.

Step 2. After removing the photoresist and cleaning, we treated the top electrode substrate with heptane solution of trichloro(1H,1H,2H,2H-perfluorooctyl)silane (TCFS) (1 μL/mL), which can selectively bond to the substrate through Si-O bonds.

Step 3. After the treatment, PMMA is spin-coated onto the substrate. Due to the fluorine-saturated alkyl chain in TCFS, the substrate becomes omniphobic while the Au surface remains unchanged. As a result, the adhesion between PMMA and the SiO_2 surface is significantly reduced without influencing that between the PMMA and the Au electrodes, which facilitate the detachment of Au electrodes from the substrate in the next step.

Step 4. The PMMA is peeled off from the substrate with the Au electrode, resulting a TRT/PMMA/electrode stack.

Step 5. The TRT/PMMA/electrode stack is used to generate various 2DP/MoS_2 superlattices using the vacuum stacking method described in previous section. Once the superlattice reaches designed structure (i.e. layer number and composition), we release the TRT and kept the stack (PMMA/electrode/superlattice film) on the substrate before we proceeded to the next step.

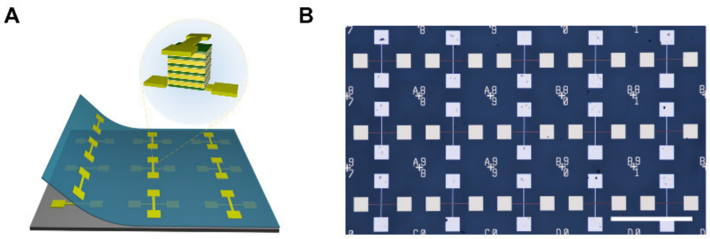

Figure 4.16 Capacitor arrays fabricated on 2DP/MoS_2 superlattice films. (**A**) Schematic of vertical capacitor device arrays and individual device geometry. (**B**) Optical image of a 3-by-5 capacitor device array. Scale bar, 500 μm.

Step 6. A transparent PDMS film with rigid backside support was attached onto the stack in Step 5. The PMMA/electrode/superlattice film

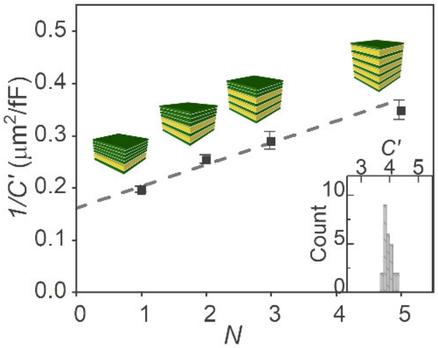

Figure 4.17 Capacitance of the 2DP/MoS_2 superlattice capacitors. The reciprocal of area-normalized capacitance, $1/C'$, is plotted as a function of N, the number of 2DP II layers in stacked $(MoS_2/2DP\ II)_N(MoS_2)_{6-N}$ films. Each data point is averaged from 10 devices with corresponding stacked film structures shown above. Green, MoS_2; yellow, 2DP II. The inset shows a capacitance histogram of 25 devices of $N = 2$.

stack was then detached from the substrate onto the supported PDMS film with the presence of water. The resulting PDMS/ PMMA/electrode/superlattice film is carefully aligned with the bottom electrodes (fabricated using conventional photolithography and deposition) using a home-made transfer stage and slowly brought into contact. The base stage is then gradually heated to 120 ℃ to release the PMMA/electrode/superlattice film from the PDMS support.

Step 7. The resulting device arrays are baked at 180 ℃ to improve adhesion and uniformity, and PMMA is removed in solvents (acetone or chloroform).

To demonstrate the capability of this method, we fabricated arrays of electrical capacitors (Fig. 4.16) from vdW heterostructures of 2DP II and MoS_2 (Fig. 4.17 inset), as it involves integration and alignment of both top and bottom electrodes, and the capacitance can be directly tuned by the thickness of the superlattices. Each device in an array consists of two gold electrodes sandwiching the vdW heterostructure film.

Fig. 4.17 shows the results measured from a series of heterostructures, $(MoS_2/2DP\ II)_N(MoS_2)_{6-N}$, where N monolayers of 2DP II films were inserted in between MoS_2 layers of a 6-layer MoS_2 stack (Fig. 4.17 inset). Thus, the dielectric thickness and the capacitance are directly tuned by varying the layer number of monolayer 2DP II. The measured inverse capacitance $1/C'$, where C' is the area-normalized capacitance, linearly increases as N increases from 1 to 5. Using the classical capacitor model, we extracted the dielectric constants of 2DP II (4.1) and MoS_2 (2.7), in agreement with reported values[13,14]. The measured capacitance from an array of devices exhibited a narrow distribution (Fig. 4.17 bottom inset), suggesting the spatial uniformity of the hybrid heterostructures. In short, this method offers a general platform to incorporate diverse molecular functionalities into vdW hybrid thin films for functional devices without compromising their structural integrity.

4.5 Summary

In Chapter 4, we discussed in detail the fabrication of hybrid vdW heterostructures and superlattices using 2DPs and monolayer MoS_2. With the large-scale synthesis capability of LAP and the easy access to the air-water interface, monolayer 2DP films can be patterned and transferred reliably at large scale, opening many opportunities for vdW integration of monolayer 2DPs. For the first time, we demonstrated programmable vdW superlattices of monolayer 2DPs and MoS_2, with arbitrary control over layer number, composition, and permutation. Both microscopic and macroscopic characterizations suggest high quality of the interface and homogeneity of the superlattice. Moreover, we developed a non-perturbative device fabrication process that uses transfer-based processes compatible with vdW integration. Using this method, we fabricated capacitor arrays using 2DP/MoS_2 heterostructure films, which showed expected behavior and demonstrated the potential of incorporating 2DPs for functional electronic devices.

4.6 References

1. Geim, A. K. & Grigorieva, I. V. Van der Waals heterostructures. *Nature* **499**, 419–425 (2013).
2. Xu, X. *et al.* Van der Waals organic/inorganic heterostructures in the two-dimensional limit. *Chem* **7**, 2989–3026 (2021).
3. Liu, Y. *et al.* Van der Waals heterostructures and devices. *Nat. Rev. Mater.* **1**, 16042

(2016).

4. Mak, K. F. & Shan, J. Semiconductor moiré materials. *Nat. Nanotechnol.* **17**, 686–695 (2022).

5. Kang, K. *et al.* High-mobility three-atom-thick semiconducting films with wafer-scale homogeneity. *Nature* **520**, 656–660 (2015).

6. Kang, K. *et al.* Layer-by-layer assembly of two-dimensional materials into wafer-scale heterostructures. *Nature* **550**, 229–233 (2017).

7. Xiao, P. & Xu, Y. Recent progress in two-dimensional polymers for energy storage and conversion: design, synthesis, and applications. *J. Mater. Chem. A* **6**, 21676–21695 (2018).

8. Payamyar, P., King, B. T., Öttinger, H. C. & Schlüter, A. D. Two-dimensional polymers: Concepts and perspectives. *Chem. Commun.* **52**, 18–34 (2016).

9. Evans, A. M. *et al.* Two-Dimensional Polymers and Polymerizations. *Chem. Rev.* **122**, 442–564 (2022).

10. Sakamoto, J., Van Heijst, J., Lukin, O. & Schlüter, A. D. Two-dimensional polymers: Just a dream of synthetic chemists? *Angew. Chemie - Int. Ed.* **48**, 1030–1069 (2009).

11. Castellanos-Gomez, A. *et al.* Van der Waals heterostructures. *Nat. Rev. Methods Prim.* **2**, 1–19 (2022).

12. Liu, Y. *et al.* Approaching the Schottky–Mott limit in van der Waals metal–semiconductor junctions. *Nature* **557**, 696–700 (2018).

13. Chen, X. *et al.* Probing the electron states and metal-insulator transition mechanisms in molybdenum disulphide vertical heterostructures. *Nat. Commun.* **6**, 6088 (2015).

14. Redel, E. *et al.* On the dielectric and optical properties of surface-anchored metal-organic frameworks: A study on epitaxially grown thin films. *Appl. Phys. Lett.* **103**, 091903 (2013).

Chapter 5: Osmotic Power Generation with Nanoporous 2DPs

5.1 Introduction

In this chapter, we will shift our focus to applications of 2DPs as advanced membranes. Membrane-based processes have attracted great attention due to their low energy cost and small environmental footprint compared to traditional energy-intensive processes such as distillation. For almost all membrane-based processes, permselectivity and permeability are the two most important characteristics of a membrane. In general, there is a significant trade-off between the permselectivity and permeability which is materials dependent. Therefore, great efforts have been put into finding new membrane materials that can mitigate the trade-off. With their nanoscale thickness and intrinsic porosity, 2DPs are regarded as a promising platform for future membrane-based technologies that enables ultra-high permeability. Meanwhile, the chemical tunability and ordered pore structure, through precise molecular design, can lead to high permselectivity for specific applications, and therefore, significantly improve the permselectivity-permeability trade-off.

With the chemical and structural tunability, 2DPs can be used for various membrane applications that require different membrane characteristics. For instance, 2DPs with sub-nanometer pore size and hydrophobic surfaces can be used for water desalination as they allow fast and selective water transport over ions. Meanwhile, 2DPs with slightly larger pores (1-2nm) and electronegative surface decorations can selectively pass certain ions over others, leading to permselective membranes for fuel cell membrane and osmotic power generation. In addition, by designing the pore size and geometry, it is also possible to utilize 2DPs for the separation of compounds with very similar physical properties, such as propane and propene, which are difficult to separate using traditional distillation.

In this chapter, we will focus on the application of ultrathin 2DPs as membrane for osmotic power generation. Osmotic power or "blue energy", is the energy available from a salinity gradient, and is emerging as a new form of renewable energy suitable for a wide range of applications including megawatt power plants at estuaries, medical implant devices, and microscopic iontronics[1–4]. A permselective membrane that enables selective transport of cations over anions (or vice versa) is the key component for osmotic power generation. The requirement for high osmotic power generation is straightforward in principle: the membrane needs to maximize the product of net ionic current and the voltage (V_o; determined by permselectivity of the membrane) for a given concentration gradient ($\Delta = C_H/C_L$, where C_H and C_L are the ionic concentrations in either side of the membrane) across the membrane. Therefore, an ideal permselective membrane should have both large ionic conductivity and high selectivity.

As ionic conductivity scales inversely with the membrane thickness, 2D materials offer an unparalleled opportunity for high ionic conductivity. This was first demonstrated in inorganic 2D materials with single nanopores fabricated using top-down techniques (i.e., electron beam irradiation). For instance, Radenovic and coworkers[5] showed that a ~6nm diameter nanopore in a monolayer MoS_2 can generate an osmotic power density of 1 MW/m^2, while in comparison, the commercial target is only ~5 W/m^2. However, inorganic 2D materials are nonporous and impermeable to ions, and therefore, the scalability of their application is significantly limited by the top-down fabrication technique.

In contrast, the intrinsic porous structure of 2DPs allows them to be easily used for large-scale membrane applications. In addition, the structural and chemical tunability of 2DPs allows the membrane to be precisely designed at molecular level, which greatly reduces the membrane-to-membrane variation caused by fabrication and enables consistent high performance.

However, despite the outstanding potential, examples of 2DPs used for osmotic power generation with performance comparable to single pore extrapolation has never been seen[5,6]. The major reason is due to the breakdown of long-range permselectivity which is based on Coulomb screening. For most porous membranes, the selective ion transport is realized through surface charges on the membrane. For instance, if the membrane is negatively charged, it will attract cations and facilitate their trans-membrane diffusion, while it will repel anions and reduce their permeation, leading to cation-selectivity. However, this Coulomb effect is volumetric and relies on enough membrane surface and volume to accommodate surface charges. As the membrane becomes thinner, lighter, and more porous, as is the case in 2DPs, the screening effect drastically weakens resulting in a significant drop in permselectivity. Therefore, a fundamentally different permselective mechanism must be exploited to maintain high selectivity in 2DPs, which has long been missing.

In addition, the large-scale production methods for 2DPs with high mechanical strength and uniform morphology for membrane application are still limited[7]. Even though a couple of methods are used to generate large-scale 2DPs with satisfying quality, the intrinsic fragility of these materials presents a great challenge for their large-scale processing and integration. As a result, utilization of 2DPs for osmotic power generation is still preliminary and their practical application remains elusive.

In this chapter, we introduce a -OH functionalized 2D nanoporous polymer (2DNP) membrane synthesized using LAP, which utilizes short-range interactions to simultaneously realize high permselectivity and permeability. The ionic transport and the osmotic power generation of the 2DNP are measured using home-made microfluidic devices with record-high osmotic power density.

5.2 Design and Synthesis of Functionalized 2D Nanoporous Membranes

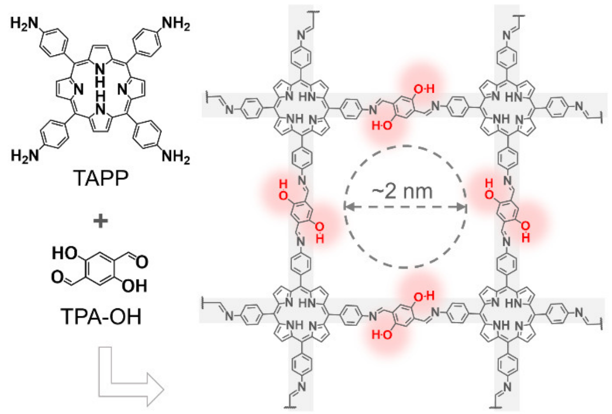

Figure 5.1 Reaction scheme and structural backbone of the 2DNP membrane.

The design of our 2DNP membrane is illustrated in Fig. 5.1. The 2DNP membrane was synthesized using LAP that has been discussed in detail in previous chapters. Here, the amphiphilic monomer is 5,10,15,20-tetrakis(4-aminophenyl)-21H,23H-porphine (TAPP), which reacts with the 2,5-dihydroxyterephthalaldehyde (TPA-OH) in the bottom phase to form an imine-linked 2D network through Schiff-base reaction. The reaction can happen at room temperature in a relatively short time (~1 day) without any catalysts, and the imine linkage is chemically stable in aqueous environment, making the 2DNP suitable for osmotic power generation applications.

As discussed in section 5.1, the Coulomb interaction-based permselectivity is not effective in 2DNPs with high porosity and extreme thinness. Inspired by biological ion channels, which utilizes short-range interactions between polar functional groups (e.g., carbonyls and hydroxyls) and ions for selective ion diffusion, we integrated hydroxyl groups in the 2DNP by using OHsubstituted linkers (TPA-OH). Thanks to the versatile reticular chemistry of 2DPs, we can change the TPA, which was used in previous synthesis of 2DP IV as described in Chapter 3, to TPA-OH without significantly modifying the synthetic conditions, and still produce materials with similar quality and morphology.

	H_2O (kcal/mol)	Phenol (kcal/mol)
Na^+	~24[8]	21-24[9]
Cl^-	13.1 ~15[10]	19.4[11]
K^+	17.9[8]	17.7[12]
Li^+	34.0[8]	42.7[12]

Table 5.1 Literature binding energies for ions with H_2O and phenol.

While many polar functional groups can be incorporated into the 2DNP through molecular design, we choose hydroxyl groups for two reasons: (i) at moderate pH conditions (5~8), -OH is virtually free of deprotonation due to its large pKa (~10) and leaves the 2DNP charge-neutral. This charge-neutrality allows us to investigate the effectiveness of the short-range interaction for selective ion transport and better understand the mechanism of this new approach without interference of surface charges; (ii) due to the large polarity and hydrogen bonding capability, it can bind strongly to various ions, with $\varepsilon_{\mathrm{OH}}$, the ion-OH binding energy, comparable to $\varepsilon_{\mathrm{H_2O}}$, the ion-water binding energy[8–12] (Table 5.1). As an important example, previous studies showed that Cl^- binds more strongly to -OH (i.e., $\varepsilon_{\mathrm{OH}} > \varepsilon_{\mathrm{H_2O}}$)[10,11], while Na^+ prefers binding to a water molecule ($\varepsilon_{\mathrm{OH}} < \varepsilon_{\mathrm{H_2O}}$)[8,9]. Such binding preferences give -OH groups the potential to selectively passing Na^+ over Cl^-, which are the major ions in seawater and river water for practical osmotic power generation; (iii) it has been shown that -OH groups at the ortho position of the imine bond can form intramolecular hydrogen bonds between the hydroxyl hydrogen and the imine nitrogen, which increase the chemical stability of the 2DP and increase the crystallinity[13].

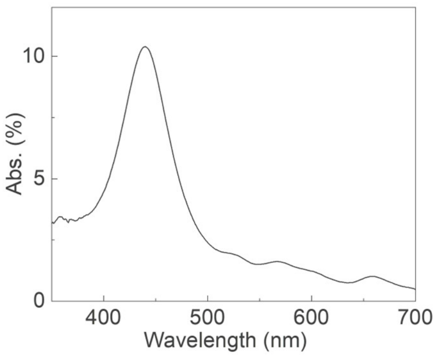

Figure 5.2 UV-Vis spectrum of the 2DNP membrane.

Based on the molecular design, TAPP and TPA-OH forms an imine-linked network with high density of ~2 nm nanopores (~2.5 nm center-to-center distance between neighboring pores) that are decorated by phenolic -OH groups (Fig. 5.1). The pore size should allow for sufficient short-range interaction while most hydrated ions can pass through it. The formation of the imine-linked network was characterized using UV-Vis spectroscopy and Fourier-transform infrared (FTIR) spectroscopy. Figure 5.2 shows the UV-Vis absorption spectrum of the 2DNP membrane. The prominent absorption peak at ~440 nm was identified as the porphyrin Soret band, indicating the incorporation of the TAPP molecule in the 2DNP. In the FTIR spectra shown in Fig. 5.3, the two monomers and the 2DNP show distinct features, indicating the occurrence of the reaction. Particularly, the new peak at 1635 cm^{-1} for 2DNP is a signature for imine bond stretching, and the absence of the doublet N-H stretching also indicates a relatively complete polymerization. The FTIR also suggests the integration of -OH groups in the 2DNP as indicated by the broad peak at ~3400 cm^{-1} that is typical for O-H stretching.

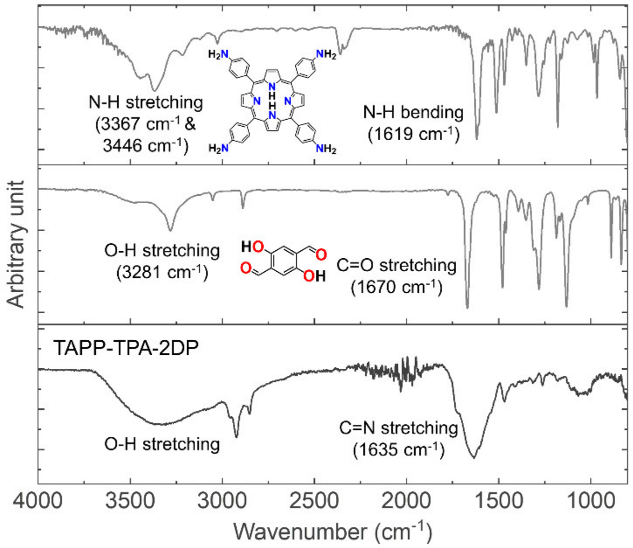

Figure 5.3 FTIR spectra of the 2DNP membrane and its molecular precursors.

Using the LAP method, the 2DNP can be synthesized at large-scale with homogeneous sub-2 nm thickness and substantial mechanical strength. As a result, the membrane can be transferred to various substrates either through water-based transfer technique (Fig. 5.4A, detailed discussion in Chapter 4) or directly using the Langmuir-Schaefer method (Fig. 5.5A). Fig. 5.4B shows an optical image of the transferred 2DNP of more than 1x1 mm^2 on SiO_2/Si substrate with a laser-created pattern. The uniform and strong optical contrast indicate the high quality of the synthesized 2DNP. The mechanical strength of the 2DNP allows it to be transferred to holey carbon films and suspend over micron-sized holes (Fig. 5.5B), creating freestanding 2DNP membranes that are essential for any ionic transport. The ultra-thinness of the 2DNP and the surface morphology have been characterized using atomic force microscopy (AFM). As shown in Fig. 5.6, the 2DNP has a uniform thickness of ~2nm, corresponding to 3-4 monolayers. In addition, the surface is extremely smooth with a roughness of ~0.1 nm, which is comparable to the underlying SiO_2/Si substrate (Fig. 5.6 and Fig. 5.7).

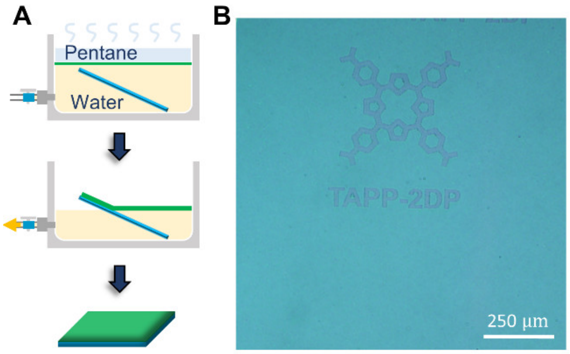

Figure 5.4 Water-draining transfer of the 2DNP membrane. (**A**) Schematic illustration of transferring 2DNP membrane by draining the subphase. (**B**) Optical image of 2DNP membrane on SiO2/Si substrate transferred by draining. The patterns are created by a 532nm laser.

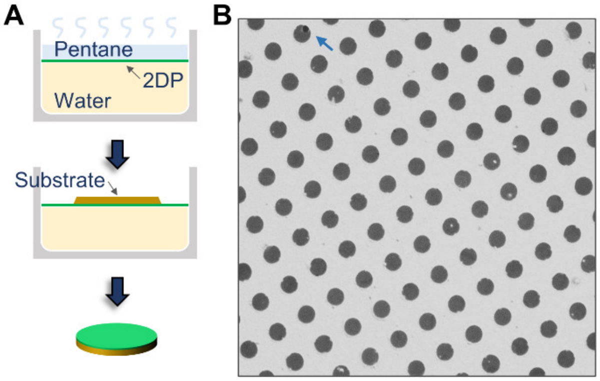

Figure 5.5 Modified Langmuir-Schaefer transfer of the 2DNP membrane. (**A**) Schematic illustration of transferring 2DNP membrane by contacting from the top. (**B**) SEM image of 2DNP membrane suspended over a porous carbon support using the top contact method. The arrow indicates a hole with broken membrane. The diameter of the holes is 2 μm.

5.3 Microfluidic Membrane Devices for Ion Transport

The 2D thinness (< 2 nm) makes it difficult to suspend 2DNP membranes beyond microscale,

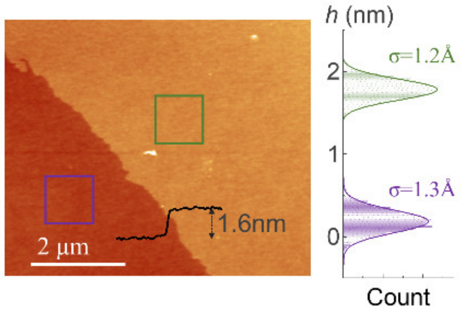

Figure 5.6 AFM characterization of transferred 2DNP. Left: AFM image of 2DNP transferred onto a SiO_2/Si substrate. A line profile across the 2DNP edge is overlayed. Right: Height histograms for the corresponding areas in the AFM on the left (purple: SiO_2/Si substrate, green: 2DNP).

and therefore, prohibits 2DNPs from direct large-scale membrane application. However, it is possible to leverage 2DNPs for membrane applications in combination with microporous support[14]. As a proof-of-concept demonstration and for the purpose of mechanistic study, we fabricated customized microfluidic devices (illustrated in Fig. 5.8) of 2DNP membrane supported by a micropore (diameter between 200 ~ 500 nm) to conduct various ion transport measurements and osmotic power generation experiments. To fabricate the microfluidic device, a submicron hole was first created in a SiN_x membrane (thickness of 50 nm) using focused ion-beam milling. Then, the 2DNP membrane was transferred to the SiN_x membrane using a modified Langmuir-Schaefer method by dropping the SiN_x membrane onto the 2DNP (Fig. 5.5). Finally, the 2DNP membrane on the SiN_x support was mounted between two customized acrylic compartments using silicone O-rings (Fig. 5.8).

For the electrical measurements, a pair of Ag/AgCl electrode were used to apply voltage and collect current from the microfluidic device. The voltage was supplied using a NI-6341 I/O device while the current was first amplified by a SR-570 preamplifier and then analyzed by the same I/O device that supplied the voltage. To eliminate the capacitance effect from the SiN_x in all current-voltage (*I-V)* measurements, the DC current was obtained by applying a constant voltage for at least 5s and using an exponential fit to get the steady state current. The redox potentials of the Ag/AgCl electrodes in

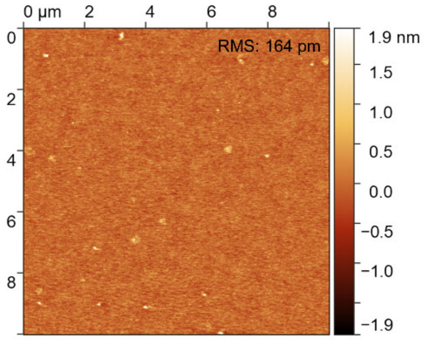

Figure 5.7 AFM image of continuous 2DNP on SiO_2/Si substrate.

different salt solutions were measured against a saturated Ag/AgCl reference electrode, and the contribution from their potential difference was subtracted when a concentration gradient is present across the membrane. The ionic concentrations of the solutions on either side of the membrane were controlled independently (C_{H} and C_{L}, respectively), generating a concentration gradient $\Delta = C_{\mathrm{H}}/C_{\mathrm{L}}$, ranging between 1 to 1000.

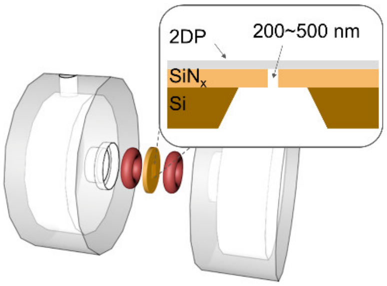

Figure 5.8 Schematic of the 2DNP microfluidic device.

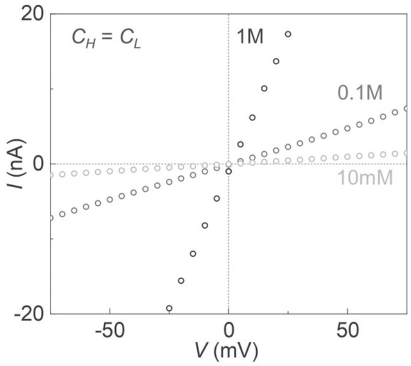

Figure 5.9 *I*−*V* responses of a representative 2DNP membrane with different salt concentrations ($C_{\mathrm{H}} = C_{\mathrm{L}}$).

Fig. 5.9 shows *I-V* curves measured from a representative device using KCl solutions of three different concentrations (C; $\Delta = 1$). The ionic conductance (G) of the membrane, measured from the slope of these linear *I-V* curves, is plotted at different C in Fig. 5.10. It shows that G monotonically decreases with C but shows different characteristics at high concentrations and low concentrations: at higher C (> 10 mM), G decreases linearly with C, whereas the dependence is sublinear at lower C. Such behavior is significantly different from that of an electrically charged membrane, where G remains constant at low salt concentrations as the ionic conductance is dominated by surface charges[15–17]. For comparison, G vs C curves expected for three different surface charges (1, 0.1, 0 mC/m^2, dashed lines) are shown in Fig. 5. 10. In contrast, our data agree well with a variable

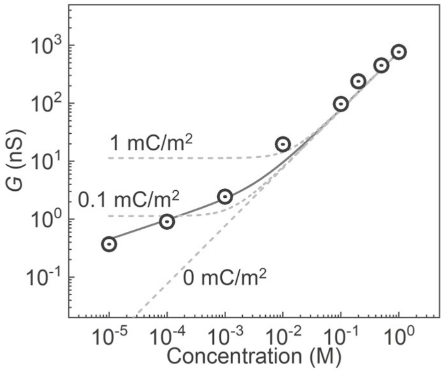

Figure 5.10 Conductance of the 2DNP membrane at different KCl concentrations. The dashed lines are calculated for different constant surface charge densities, and the solid line is the best fit of the data to a variable surface charge model.

Material	Δ	power density (W/m^2)	*S*	areal conductance (S/m2)	Ref.
2DNP	10	203	~0.6	5.2x10^6 (at 1M KCl)	This thesis
	100	551			
	1000	2003			
monolayer COF	50	204	~0.4	5.7x10^5 (at 0.1M KCl)	30
imine-based 2D polymer	50	130	~0.6	70000 (at 0.1M KCl)	31
holey-graphene-like network	10	10	~0.6 (pH=11)	32000 (10nm membrane, at 1M KCl)	20
	100	35			
	1000	70			
single-layer nanoporous carbon	10	28	~0.4	3.2x10^6 (at 1M KCl, contribution from support has been subtracted)	14
	50	67			
	100	70			
	1000	131			
PSS/MOF composite	50	2.87	~0.8 (1uM||10uM) ~0.4 (1uM||1M)	1200 (at 1M KCl)	33
free-standing COF membrane	5	0.48	~0.7	10000	17
	50	5.9			
	500	20.1			
Mxene nanosheets	1000	21	~0.95	92000 (at 1M KCl)	34
nanoporous graphene	10	5	~0.88	15000 (at 1M KCl)	29
	100	14			
	1000	27			
functionalized track-etched PET	10	0.022			26
	50	0.078			
	100	0.11			
	1000	0.15			
Janus porous polymer	5	0.26	~0.84		27
	50	2.65			
	500	5.1			
block copolymer/PET hybrid membrane	10	0.16	~0.74		28
	50	0.35			
	100	0.91			
	1000	1.6			
Nafion	10	0.075	~0.8		21
	100	0.475			
	1000	0.675			
	2000	0.755			
black phosphorus/graphene oxide composite	50	4.7	~0.7		32

Table 5.2 Comparison between the 2DNP membrane and previously reported membranes.

surface charge model where *G* scales with $C^{1/3}$ at low concentrations (solid line) without a constant minimum[18]. This behavior has been related to the adsorption of charged species onto a neutral surface, consistent with the charge-neutral structure of our 2DNP membrane. Our data also confirm that the 2DNP membrane is highly permeable to ions, with one of the highest areal ionic conductance *G*/*A*, where *A* is the membrane area defined by the aperture of the SiN_x support (Fig. 5.11), for osmotic power membranes reaching ~ 500 S/cm^2 at 1M KCl (Table 5.2).

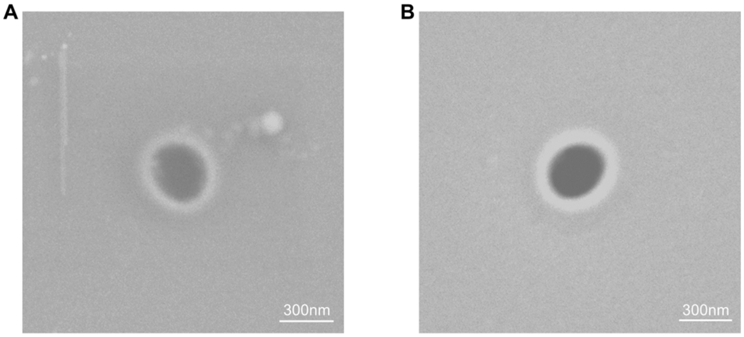

Figure 5.11 SEM images of (**A**) a SiN_x aperture covered by 2DNP membrane and (**B**) a SiN_x aperture not covered by 2DNP membrane

In addition, the ion transport across the 2DNP membrane allows us to estimate its effective pore size. This is achieved by measuring the transmembrane conductance of a series of tetraalkylammonium chlorides $[(C_nH_{2n+1})_4N]Cl$ with increasing alkyl chain lengths (n = 1 ~ 5). Thanks to their small sizes (~1 nm in diameter) and the rigidity of alkyl chains, the interaction between these ions and the 2DNP membrane is dominated by their ionic nature. Therefore, these ions allowed us to only increase the size of the cation without significantly affecting the ion-membrane interactions. As *n* increases, the cross-membrane mobility of the cation (α_m) will decrease relative to the bulk value (α_{bulk}) because of the small pore size and steric hindrance, and a simple hydrodynamic model predicts[19]:

$$\frac{\alpha_m}{\alpha_{bulk}} = c\left[1 - \frac{d}{D}\right]^2 \qquad (5.1)$$

where α_m and α_{bulk} are each normalized using the mobilities of Cl^- as a reference, *d* is the diameter of the hydrated cations, *D* is the diameter of the pores, and *c* is a constant coefficient[19]. Here, the relative ion mobility ratio α_m was extracted through a series of diffusion experiments with Δ = 10 across the membrane using the Henderson equation[20]:

$$\alpha_m = \frac{\mu_+}{\mu_{Cl}} = -\frac{z_+}{z_-} \cdot \frac{\ln(\Delta) - \frac{z_- F V_0}{RT}}{\ln(\Delta) - \frac{z_+ F V_0}{RT}} \qquad (5.2)$$

where μ_+ and μ_{Cl} are the ionic mobilities of various cations and Cl$^-$; z_+ and z_- are the charge valences of cations and anions (Cl$^-$); F is the Faraday constant; V_0 is the open-circuit potential; R is the universal gas constant, and T=296 ± 3K is the experimental temperature.

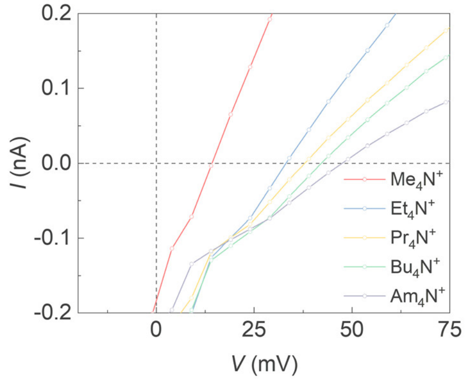

Figure 5.12 *I-V* characteristics of different tetraalkylammonium chlorides at Δ=10.

Fig. 5.12 plots the raw *I-V* curves measured from $[(C_nH_{2n+1})_4N]Cl$ solutions (n = 1-5) and the extracted μ_+/μ_{Cl} and α_m/α_{bulk} against ion radius are plotted in Fig. 5.13. Our results show that the relative mobility (μ_+/μ_{Cl}) for $[(C_nH_{2n+1})_4N]^+$ across the 2DNP membrane is monotonically decreasing as the cation size increases. The relative decrease from the bulk value becomes more significant as the cation becomes larger, leading to a result consistent with the hydrodynamic model. The best fit to the data using Equation 5.1 (dashed curve in Fig. 5.13B) results in a D value close to 1.9 nm, which is consistent with the designed pore size of our

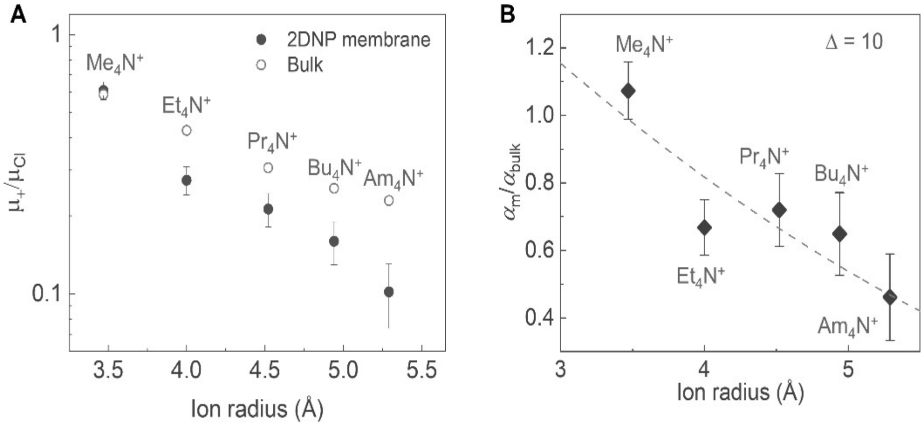

Figure 5.13 2DNP nanopore steric effects on different tetraalkylammonium cations. (**A**) The relative mobility of tetraalkylammonium cations to Cl$^-$ (μ_+/μ_{Cl}) across the membrane and in bulk (literature) as a function of the tetraalkylammonium cation radius. (**B**) Relative mobility ratios of different tetraalkylammonium cations to Cl$^-$ (normalized by their mobilities in bulk solutions). The dashed line is the best fit to the data using a hydrodynamic model. The extracted pore size from the fit is ~1.9 nm.

membrane (see Fig. 5.1). Through various ion transport measurements using our 2DNP microfluidic devices, we confirm that our 2DNP membranes are highly permeable to ions with effective pore size close to our molecular design.

5.4 Giant Osmotic Power Generation from Functionalized Nanoporous 2DPs

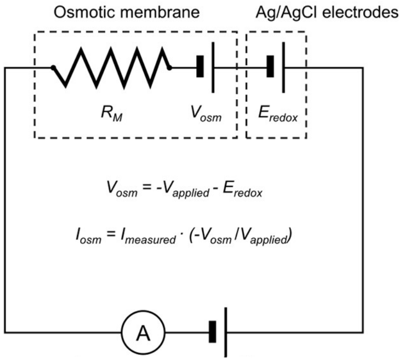

Figure 5.14 The circuit diagram for the osmotic power generation measurements with 2DNP.

The osmotic power generation from the 2DNP is also tested using the microfluidic devices with a salinity gradient *Δ* (>1) across the membrane. As ions move through a permselective membrane, preferential transport of cations or anions causes accumulation of charges on opposite sides of the membranes, creating a potential across the membrane. This membrane potential can then be harnessed using external circuits, and the whole process is called reverse electrodialysis, which is one of the two major methods for osmotic power generation.

Therefore, having high permselectivity is critical for 2DNPs to be used for osmotic power generation. Fig. 5.14 shows the equivalent circuit diagram of the osmotic power generation measurement. The 2DNP can be viewed as a voltage source (from osmotic power generation) and a resistor (from finite ion permeabilities) connected together, while the Ag/AgCl electrodes can be treated as an additional voltage source due to their redox potential difference in salt solutions of different concentrations. For the measurement, an

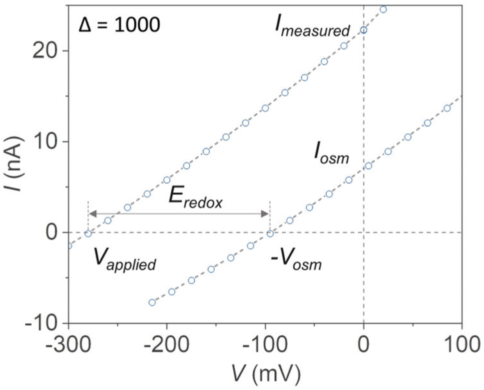

Figure 5.15 *I-V* characteristics of the 2DNP membrane before and after subtraction of the contribution of Ag/AgCl electrodes.

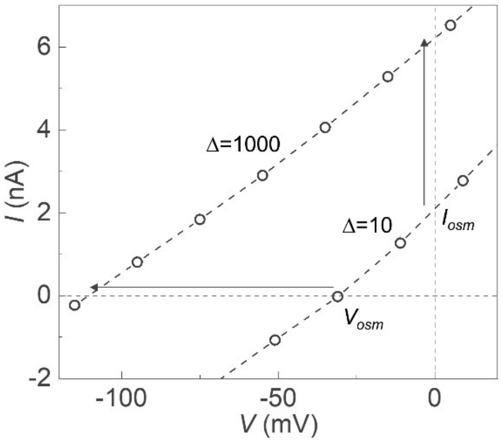

Figure 5.16 $I - V$ characteristics of a 2DNP membrane at Δ = 10 and Δ = 1000.

external voltage V_{applied} is applied and the current flowing through the circuit is recorded as I_{measured}. At zero current, the applied external voltage equals the sum of osmotic potential generated by the 2DNP and the redox contribution from the Ag/AgCl electrodes. After subtracting the Ag/AgCl contribution, we can get the osmotic potential V_{osm} from the 2DNP. Assuming the resistance of the system is dominated by that of the 2DNP and remains constant for all applied voltages, the osmotic current I_{osm}, defined as the current when the membrane is short-circuited, satisfy the relationship $I_{\text{osm}} / I_{\text{measured}} = -V_{\text{osm}} / V_{\text{applied}}$ (the minus sign account for the opposite polarity of V_{osm} and V_{applied}). Therefore, V_{osm} and I_{osm} can both be obtained by translating the raw *I-V* curves by the amount of the Ag/AgCl redox contribution as shown in Fig. 5.15. In addition, the polarity of I_{osm} also indicates the polarity of the permselectivity: the membrane is cation-selective if I_{osm} is positive (same direction as the concentration gradient) and vice versa. For the rest of this dissertation, all *I-V* curves have been translated to account for the Ag/AgCl redox contribution unless otherwise specified.

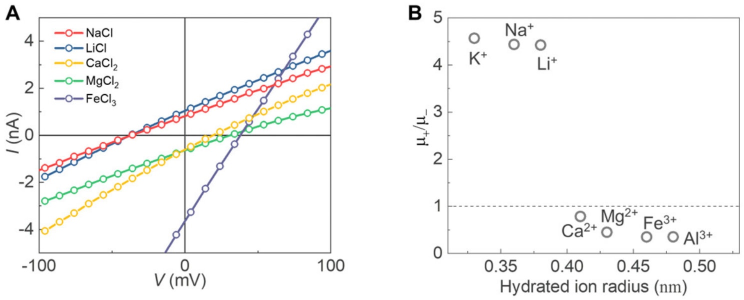

Figure 5.17 Transport of different metal chloride salts across the 2DNP membrane. (**A**) *I-V* characteristics of various metal chloride salts across the 2DNP membrane at Δ=10. (**B**) the relative mobility of cations with different charge valences to Cl^- (μ_+/μ_{Cl}) as a function of their hydrated radius.

Fig. 5.16 shows *I-V* curves measured using our 2DNP membrane under $\Delta = 10$ and 1000 with KCl solutions. KCl solutions are used to develop a mechanistic

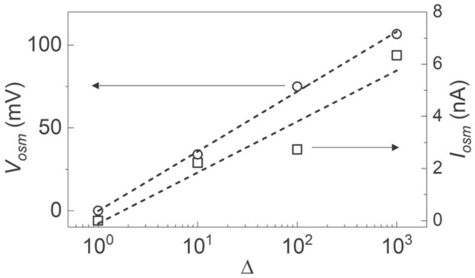

Figure 5.18 V_{osm} and I_{osm} of 2DNP measured at different Δ.

understanding of permselective process because of the close resemblance of K^+ and Cl^- in their sizes and ionic mobilities. Both curves show positive current I_{osm} at a zero bias, confirming net osmotic current and cation-selectivity. V_{osm} was measured to be ~ 120 mV for Δ = 1000, which is higher than most membranes of similar thickness[5,15,21]. These observations are the results of permselective ion transport and other monovalent ionic solutions (i.e., NaCl, LiCl) show similar characteristics (Fig. 5.17). Both V_{osm} and I_{osm} increase with increasing Δ (Fig. 5.18) and the cation selectivity S of the membrane can be calculated using the equation[22]:

$$V_{\mathrm{osm}} = S \cdot \frac{RT}{zF} \cdot ln\left(\frac{\gamma_{\mathrm{H}} C_{\mathrm{H}}}{\gamma_{\mathrm{L}} C_{\mathrm{L}}}\right) \qquad (5.3)$$

where R is the universal gas constant, T is the ambient temperature (296 ± 3K), z is the charge valence of ions, F is the Faraday constant, γ_{H} and γ_{L} are the activity coefficient[23] of the KCl at concentration C_{H} and C_{L} respectively. S here is defined as $S = t_+ - t_-$, where t_+ and t_- are the transference number of cations and anions across the membrane. From our data, we extract S ~ 0.6, which is higher than the values from previously reported ultrathin 2D nanoporous membranes and single pores in 2D materials[5,6,14,15].

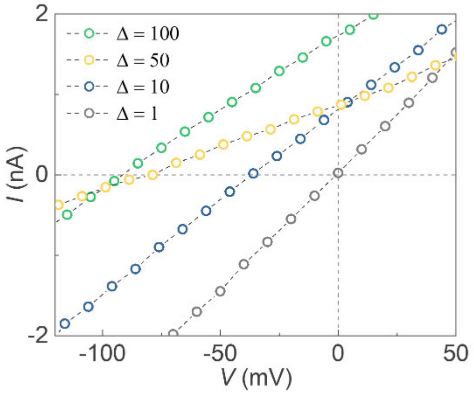

Figure 5.19 Osmotic power generation using NaCl solutions. The membrane diameter is ~350 nm.

Because the I-V response is linear within the range of interest, the maximum power density (P_{max}) of the membrane can be estimated as $P_{\mathrm{max}} = |I_{\mathrm{osm}} \cdot V_{\mathrm{osm}}|/4A$. For the device shown in Fig. 5.16, P_{max} is higher than 2

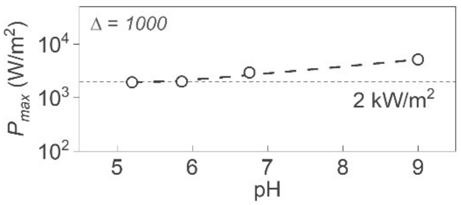

Figure 5.20 $P_{\max}$ of 2DNP membrane at different pH.

kW/m^2 at $\Delta = 1000$ (KCl solutions), setting a record for any reported porous membranes. To better represent the practical scenario, the osmotic power generation of 2DNP was measured with NaCl solutions, which is the predominant salt in natural seawater and river water. At a concentration arrangement of 0.5M||0.01M NaCl, which mimics that of natural seawater and river water, the 2DNP retained its high performance and achieved a power density of 350 W/m^2 (Fig. 5.19).

Remarkably, our 2DNP membrane can generate high osmotic power under a large range of pH (Fig. 5.20). This is drastically different from previously reported charge-based membranes: their power performance is sensitive to pH, which modulates the membrane surface charge densities. Achieving high performance usually requires harsh pH conditions to increase the surface charge density, which is not feasible in a practical situation. The pH-tolerance of our charge-neutral 2DNP membranes is a direct result of our molecular design, which leverage the pairwise short-

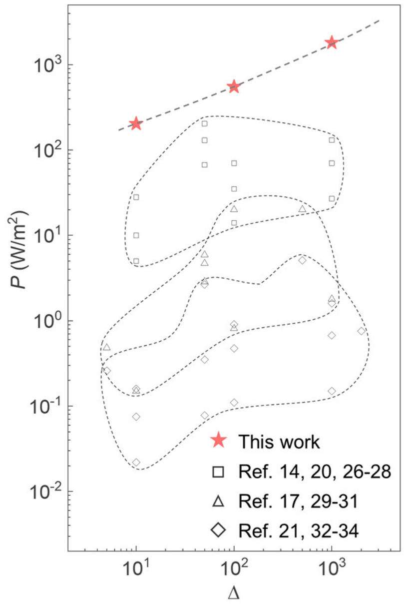

Figure 5.21 Comparison of power densities (P) for our 2DNP membrane (stars) and previously reported materials (squares for sub-10 nm nanoporous membranes, triangles for composite membranes, and rhombuses for polymeric membranes). All power densities are taken from ambient pH conditions.

range interactions between -OH and ions for permselectivity. As it has been shown in previous reports[24,25], the pairwise short-range interaction between polar groups and charged ions is less sensitive to pH conditions.

Fig. 5.21 compares osmotic power density reported from previous studies with our results (red stars). It clearly shows that our 2DNP produces the highest power density at various Δ[14,17,20,21,26–34]. This high performance is a direct result of the combination of high ionic conductance and high permselectivity, without a strong trade-off between the two that limits the performance of many ultrathin membranes[14,15,29,30].

5.5 Summary

In this chapter, we investigated the application of 2DPs as advanced membranes for osmotic power generation. Specifically, the 2D thinness, high porosity, and precisely tunable structures make them ideal candidate for this application. To circumvent the ineffectiveness of Coulomb screening in 2D porous membranes, we design and synthesized a -OH functionalized 2D nanoporous polymer with imine linkage using LAP, which utilize the short-range interaction between -OH and ions to achieve permselective ion transport. The ion transport and osmotic power generation of the 2DNP is characterized using a customized microfluidic device, and our results demonstrate that high permselectivity and high ionic conductance can be achieved simultaneously as short-range interactions are effective even in a porous and ultrathin membrane. As a result, a record-high power density exceeding 2 kW/m^2 was achieved. The effectiveness of this mechanism should change sensitively depending on the nature and strength of each interacting pair and the precise geometry of the membrane system. For systematic optimization and advanced application developments, it is essential to understand the role of short-range interactions and the nanopore dimensions during the ion transport. In next chapter, coarse-grained molecular dynamics simulation will be utilized to study the short-range interaction based permselectivity and to understand the interplay between these interactions and microscopic membrane structures.

5.6 References

1. Logan, B. E. & Elimelech, M. Membrane-based processes for sustainable power generation using water. *Nature* **488**, 313–319 (2012).
2. Siria, A., Bocquet, M. L. & Bocquet, L. New avenues for the large-scale harvesting of blue energy. *Nat. Rev. Chem.* **1**, 1–10 (2017).
3. Zhang, R. *et al.* A Streaming Potential/Current-Based Microfluidic Direct Current Generator for Self-Powered Nanosystems. *Adv. Mater.* **27**, 6482–6487 (2015).
4. Schroeder, T. B. H. *et al.* An electric-eel-inspired soft power source from stacked hydrogels. *Nature* **552**, 214–218 (2017).
5. Feng, J. *et al.* Single-layer MoS2 nanopores as nanopower generators. *Nature* **536**, 197–200 (2016).
6. Sahu, S. & Zwolak, M. Colloquium : Ionic phenomena in nanoscale pores through 2D materials. *Rev. Mod. Phys.* **91**, 021004 (2019).
7. Evans, A. M. *et al.* Two-Dimensional Polymers and Polymerizations. *Chem. Rev.* **122**, 442–564 (2022).
8. Džidić, I. & Kebarle, P. Hydration of the alkali ions in the gas phase. Enthalpies and entropies of reactions M+(H2O)n-1 + H2O = M+(H2O)n. *J. Phys. Chem.* **74**, 1466–1474 (1970).
9. Dunbar, R. C. Metal Cation Binding to Phenol: DFT Comparison of the Competing Sites. *J. Phys. Chem. A* **106**, 7328–7337 (2002).
10. Xantheas, S. S. Quantitative description of hydrogen bonding in chloride-water clusters. *J. Phys. Chem.* **100**, 9703–9713 (1996).
11. Yamdagni, R. & Kebarle, P. Hydrogen-bonding energies to negative ions from gas-phase measurements of ionic equilibriums. *J. Am. Chem. Soc.* **93**, 7139–7143 (1971).
12. Amunugama, R. & Rodgers, M. T. Influence of substituents on cation-π interactions. 3.: Absolute binding energies of alkali metal cation-aniline complexes determined by threshold collision-induced dissociation and theoretical studies. *Int. J. Mass Spectrom.* **227**, 339–360 (2003).
13. Kandambeth, S. *et al.* Enhancement of chemical stability and crystallinity in porphyrin-

containing covalent organic frameworks by intramolecular hydrogen bonds. *Angew. Chemie - Int. Ed.* **52**, 13052–13056 (2013).

14. Liu, X. *et al.* Power generation by reverse electrodialysis in a single-layer nanoporous membrane made from core–rim polycyclic aromatic hydrocarbons. *Nat. Nanotechnol.* **15**, 307–312 (2020).

15. Yazda, K. *et al.* High Osmotic Power Generation via Nanopore Arrays in Hybrid Hexagonal Boron Nitride/Silicon Nitride Membranes. *Nano Lett.* **21**, 4152–4159 (2021).

16. Siria, A. *et al.* Giant osmotic energy conversion measured in a single transmembrane boron nitride nanotube. *Nature* **494**, 455–458 (2013).

17. Hou, S. *et al.* Free-Standing Covalent Organic Framework Membrane for High-Efficiency Salinity Gradient Energy Conversion. *Angew. Chemie - Int. Ed.* **60**, 9925–9930 (2021).

18. Secchi, E., Niguès, A., Jubin, L., Siria, A. & Bocquet, L. Scaling Behavior for Ionic Transport and its Fluctuations in Individual Carbon Nanotubes. *Phys. Rev. Lett.* **116**, 154501 (2016).

19. Dwyer, T. M., Adams, D. J. & Hille, B. The permeability of the endplate channel to organic cations in frog muscle. *J. Gen. Physiol.* **75**, 469–492 (1980).

20. Wang, H. *et al.* Blue Energy Conversion from Holey-Graphene-like Membranes with a High Density of Subnanometer Pores. *Nano Lett.* **20**, 8634–8639 (2020).

21. Tsai, T.-C., Liu, C.-W. & Yang, R.-J. Power Generation by Reverse Electrodialysis in a Microfluidic Device with a Nafion Ion-Selective Membrane. *Micromachines* **7**, 205 (2016).

22. Kim, D. K., Duan, C., Chen, Y. F. & Majumdar, A. Power generation from concentration gradient by reverse electrodialysis in ion-selective nanochannels. *Microfluid. Nanofluidics* **9**, 1215–1224 (2010).

23. Dash, D., Kumar, S., Mallika, C. & Mudali, U. K. New Data on Activity Coefficients of Potassium, Nitrate, and Chloride Ions in Aqueous Solutions of KNO 3 and KCl by Ion Selective Electrodes . *ISRN Chem. Eng.* **2012**, 1–5 (2012).

24. Le Tilly, V., Sire, O., Wong, P. T. T. & Alpert, B. pH dependence of hydrogen bond strengths in myoglobin α-helices. *Chem. Phys. Lett.* **192**, 62–64 (1992).

25. Wu, X. *et al.* H-bond interactions between arsenite and deoxynucleotides at different pH values: A combined computational and experimental study. *Chemosphere* **251**, 126395 (2020).

26. Balme, S., Ma, T., Balanzat, E. & Janot, J. M. Large osmotic energy harvesting from functionalized conical nanopore suitable for membrane applications. *J. Memb. Sci.* **544**, 18–24 (2017).

27. Zhu, X. *et al.* Unique ion rectification in hypersaline environment: A high-performance and sustainable power generator system. *Sci. Adv.* **4**, eaau1665 (2018).

28. Zhang, Z. *et al.* Engineered Asymmetric Heterogeneous Membrane: A Concentration-Gradient-Driven Energy Harvesting Device. *J. Am. Chem. Soc.* **137**, 14765–14772 (2015).

29. Fu, Y., Guo, X., Wang, Y., Wang, X. & Xue, J. An atomically-thin graphene reverse electrodialysis system for efficient energy harvesting from salinity gradient. *Nano Energy* **57**, 783–790 (2019).

30. Yang, J. *et al.* Advancing osmotic power generation by covalent organic framework monolayer. *Nat. Nanotechnol.* **17**, 622–628 (2022).

31. Zhang, Z. *et al.* Cation-selective two-dimensional polyimine membranes for high-performance osmotic energy conversion. *Nat. Commun.* **13**, 1–9 (2022).

32. Zhang, Z. *et al.* Oxidation promoted osmotic energy conversion in black phosphorus membranes. *Proc. Natl. Acad. Sci. U. S. A.* **117**, 13959–13966 (2020).

33. Li, R., Jiang, J., Liu, Q., Xie, Z. & Zhai, J. Hybrid nanochannel membrane based on polymer/MOF for high-performance salinity gradient power generation. *Nano Energy* **53**, 643–649 (2018).

34. Hong, S. *et al.* Two-Dimensional Ti3C2Tx MXene Membranes as Nanofluidic Osmotic Power Generators. *ACS Nano* **13**, 8917–8925 (2019).

Chapter 6: Short-Range Interaction-Dominated Ion Selectivity

6.1 Introduction

Permselectivity is one of the most important characteristics of a membrane as the core function of a membrane is separate/differentiate different constituents[1,2]. In the simplest case, permselectivity can be achieved via size-exclusion based on the different size of the constituents in a mixture. This approach has mostly been applied in water desalination and water contamination removal, as the small size of water molecules allows them to pass through precisely engineered channels while other ions/organic contaminants cannot.

However, the size-exclusion strategy has two major limitations. First, if the target permeate is not the largest or smallest in size, multiple separation processes must be used to isolate the target, leading to ineffective separation with increased processing time and cost. Second, the capability of a membrane to differentiate different sizes is limited by the precision of the membrane fabrication. As the size of the target permeate becomes closer to the rest of the mixture on the atomic/molecular scale, it becomes extremely difficult to design and fabricate a membrane to separate the target based on size-exclusion alone.

Therefore, various interactions between the permeates and the membrane have been exploited to supplement the size-exclusion strategy, leading to various permselective mechanisms. Based on the effective distance of the interaction, those interaction-based permselective mechanisms can be categorized into long-range interaction-based permselectivity and short-range interaction-based permselectivity. It is worth noting that the long- and short-range is relative, and therefore, the categorization depends on the choice of definition. For our discussion in this chapter, we adopt the widely accepted definition for long/short-range interaction in physics: long-range interactions are those where the two-body potential decays algebraically at large distances with a power equal to or smaller than the spatial dimension, while short-range interactions are those where the two-body potential decays algebraically at higher powers than the spatial dimension.

Based on this definition, a typical long-range interaction is Coulomb interaction, which decays as the inverse of the distance. As will be discussed in the next section, Coulomb interaction has been widely used for permselective ion transport in porous membranes especially for osmotic power generation, and is probably the only long-range interaction used for permselective ion transport[3–7]. The ionic nature of the permeates and the variety of ionizable functional groups makes Coulomb interaction a general permselective mechanism readily available in many materials, and the long-range nature allows for some flexibility in the membrane design without the constraint of precise molecular design.

Various types of short-range interactions, including chemical bonding, dipolar interactions, and van der Waals interactions, have been used in permselective ion transport for different applications[8–15]. In contrast to Coulomb-based permselectivity, short-range interaction-based permselectivity usually requires precise molecular design due to their short effective distance. However, it can differentiate many other features of the permeates in addition to their charge polarity and lead to very high permselectivity.

In practice, most membranes would use a combination of size-exclusion, long-range interaction, and short-range interaction to achieve desired permselectivity. This usually requires precise structural design and functionalization of the membrane, as well as a comprehensive understanding of how each mechanism contributes to the permselectivity. In this chapter, we will focus on the short-range interaction-based permselectivity observed in our 2DNP, and use both computation and experiments to investigate the exact mechanism of the permselectivity.

6.2 Comparison between Long-Range and Short-Range Ion Selectivity

In the context of osmotic power generation, the task of the permselective membrane is to create a preferential transport of cations over anions (or vice versa), which creates a net ionic current and a potential across the membrane. While permselectivity is essential to osmotic power generation, high power density can be achieved without high permselectivity as long as the permeability of ions is large enough. For instance, the power density of a micrometer-thick polymeric membrane with near-unity permselectivity can be orders of magnitude lower than that of a 2D porous membrane with only 40% of the permselectivity, as permeability scales inversely with the membrane thickness[16,17]. Therefore, reducing the membrane thickness and increasing its porosity have attracted great interests and promise unprecedented osmotic power density.

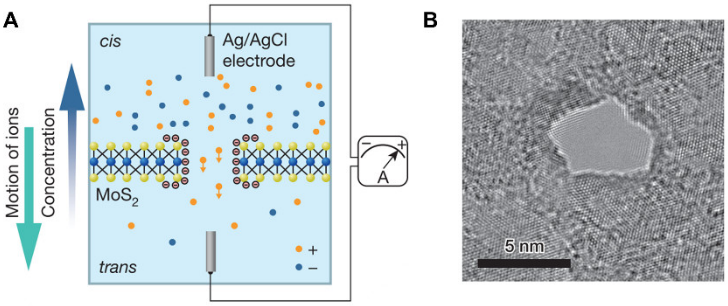

Figure 6.1 Osmotic power generation using a single MoS$_2$ nanopore. (**A**) Schematic of MoS$_2$ nanopore osmotic power generation. (**B**) TEM image of a MoS$_2$ nanopore. Reproduced from Ref. 6.

Both long-range and short-range interactions can be used to create preferential transport of ions across a membrane, and each has their own advantages and disadvantages. The osmotic power generation using 2D materials has been proposed for very long time, with probably the most successful demonstration being a series of single-pore experiments with monolayer MoS$_2$[6]. For example, a nanopore with the size of a few nanometers was created in monolayer MoS$_2$ (Fig. 6.1), and an astounding osmotic power density of 10^6 W/m^2 was achieved assuming a 10%

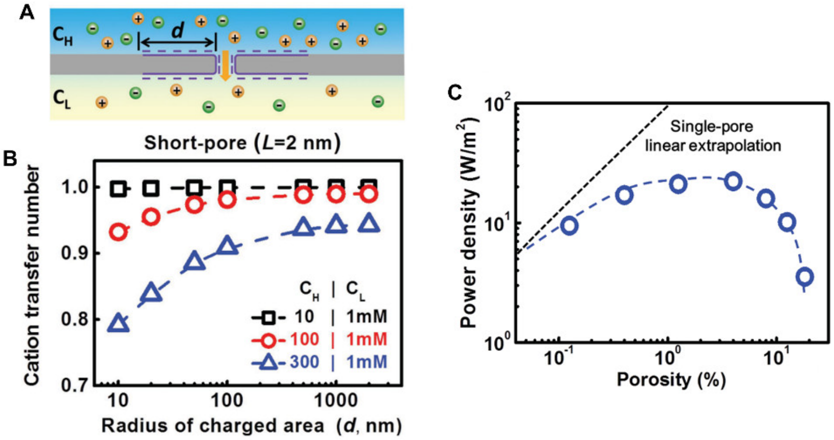

Figure 6.2 Effect of membrane surface area on Coulomb-based permselectivity. (**A**) Schematic of the simulation setup. (**B**) Cation transfer number as a function of the charged area radius. The pore length is 2 nm and diameter is 4 nm. (**C**) Calculated power density of a nanoporous membrane as a function of its porosity. The membrane is 2 nm thick, and the pore size is 4nm. Reproduced from Ref. 20.

porosity. Since the pore size is relatively large, long-range Coulomb interaction is used to achieve cation selectivity. Despite the relatively low selectivity of 0.4, the sub-nanometer thickness of the membrane allows for a very high ionic conductance, and hence, the high power density.

With more sophisticated synthetic methods, many porous 2D membranes have been synthesized using bottom-up approaches and applied to osmotic power generation[16–18]. Compared to the single pore demonstration, those porous membranes show high porosity and sometimes precisely engineered pore size. While the same Coulomb-based permselectivity is used in those membranes, none of them reaches the high power density extrapolated from the single pore experiments.

Such discrepancy between the porous membrane and the single pore experiment is due to the ineffectiveness of Coulomb screening for reduced membrane thickness and increased porosity

(Fig. 6.2). First, theoretical model has shown that as the porosity increases, the ionic conductance of the membrane does not increase linearly with the porosity. Instead, the conductance scales with $\sqrt{N}$, where N is the number of pores[19]. Second, as the membrane becomes thinner and more porous, there is less space to accommodate charges to achieve sufficient Coulomb screening (reduced d in Fig. 6.2A). Simulations have shown that sufficient membrane surface around the pore is necessary to maintain high permselectivity in a short nanopore, while increased porosity-therefore reduced d-leads to rapid degradation of the power generation (Fig. 6.2)[20]. As a result, while Coulomb screening is easy to implement and offers flexibility in membrane design, it cannot sustain a high osmotic power density alone in 2D porous membranes.

Short-range interactions, however, can be extremely effective even when the pore is ultra-short (<2nm) without surrounding membrane surface. For instance, in biological potassium channels KcsA, a Na^+/K^+ selectivity of more than 1000 can be achieved through a ~2nm selective filter composed of five sets of residual carbonyl groups (Fig. 6.3)[21,22]. In contrast to long-range

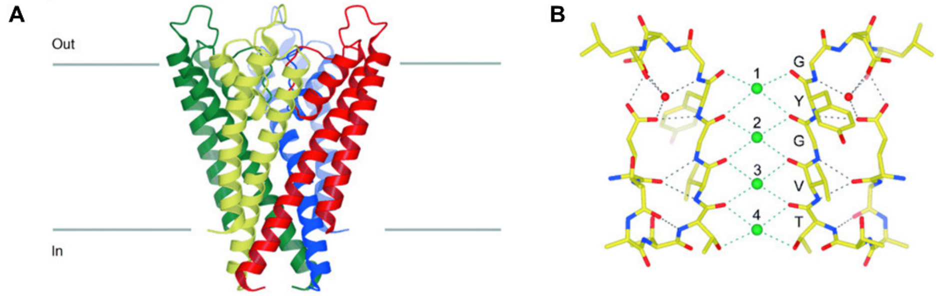

Figure 6.3 The KcsA K^+ channel. (**A**) A ribbon representation of the KcsA K^+ channel with its four subunits colored differently. The channel is oriented with the extracellular solution on top. (**B**) Detailed structure of the K^+-selectivity filter (two subunits). Oxygen atoms (red) coordinate K^+ ions (green spheres) at positions 1 to 4 from the extracellular side. Single letter amino acid code identifies select amino acids of the signature sequence (yellow: carbon, blue: nitrogen, and red: oxygen). Green and gray dashed lines show $O \cdot\cdot\cdot K^+$ and hydrogen-bonding interactions, respectively. Reproduced from Ref. 22.

interaction/Coulomb-based permselectivity, packing such selective filters into a 2D porous membrane would not influence its permselectivity as the mechanism is completely short-range and pairwise. However, to utilize short-range interactions, the membrane pore needs to be precisely designed and fabricated to ensure effective pairwise short-range interaction. In addition to size, the geometry of the pore can be equally important for certain short-range interactions such as hydrogen-bonding and coordination[11,14]. Moreover, while Coulomb screening directly sort different ions based on their polarity as needed in osmotic power generation, such selection is not always guaranteed in short-range interaction-based permselectivity. As a result, the interactions need to be carefully chosen to ensure desired selection for a given application.

With the recent advances in bottom-up synthesis of 2D polymers, it is possible to design and synthesize 2D porous membranes with atomic precision at large-scale that are relevant to practical applications. Using LAP, we made a 2DNP that for the first time utilizes short-range interactions for osmotic power generation in a 2D porous membrane (detailed discussion in Chapter 5). For the rest of this chapter, we will use molecular dynamics simulations to investigate the mechanism of short-range interaction-based permselectivity and experimentally demonstrate unique applications of our 2DNP that arise from the short-range interaction-based permselectivity. The molecular dynamics simulations were conducted by Prof. Suriyanarayanan Vaikuntanathan and Dr. Yuqing Qiu at the University of Chicago.

6.3 Mechanism Study of Short-Range Ion Selectivity Using Molecular Dynamics Simulations

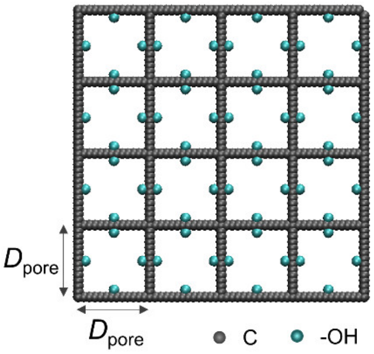

Figure 6.4 Visualization of the 2DNP membrane simulated by CG-MD.

In order to understand the mechanism of the short-range ion selectivity in our 2DNP, we developed a coarse-grained molecular dynamics (CG-MD) model incorporating realistic elements[23,24]. The essential structural features of the 2DNP are represented by porous carbon networks with -OH groups placed at all edges of each pore (Fig. 6.4). MD simulations of 2DNP membranes are performed with LAMMPS program[25], where water molecule is modeled using the monatomic water (mW) model[24] and NaCl is modeled with a coarse-grained ion model[23] that is parameterized to reproduce the water's solvation of ions. The backbone of the two-dimensional polymer is represented by a chain of CH_2 groups with the Lennard-Jones interactions of the UA-OPLS[26] force field. The hydroxyl groups are modeled with mW. The interactions between the OPLS carbon and mW water/Na^+/Cl^- ions are described by the same Lennard-Jones potential parameterized in a previous study to reproduce the surface tension of the nonane–water interface[27]. The interaction between OH and mW water is the same as that between mW water molecules. We scale the interactions between OH and Na^+(Cl^-) from the interactions between

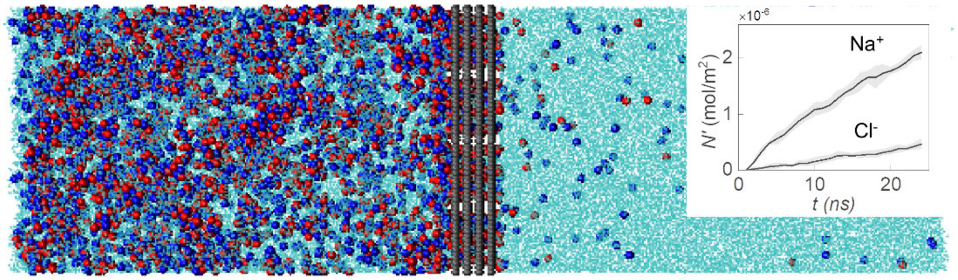

Figure 6.5 Snapshot of a representative simulation box used in CG-MD simulations. Inset: permeation of Na^+ and Cl^- across the 2DNP membrane from the simulation.

water and $Na^+(Cl^-)$. We fix the positions of the two-dimensional membrane so that there are no effective interactions between OPLS carbon and OH groups in the membrane.

A wide spectrum of membranes with different pore-to-pore distance D_{pore} (which is about 0.4 nm larger than the actual pore size due to the van der Waals volume of carbon atoms), 2DNP layer number n, and $\varepsilon_{\mathrm{OH}}$ were investigated using CG-MD simulations. A key parameter for the short-range interaction in our simulations is θ_{ion}, the ratio between specific ion's binding energies to -OH vs H_2O ($\varepsilon_{\mathrm{OH}}/\varepsilon_{\mathrm{H_2O}}$), making the ion more likely to bind to -OH if $\theta_{\mathrm{ion}} > 1$. Previous studies indicate that $\theta_{\mathrm{Cl}} = 1.2 \sim 1.4$, whereas $\theta_{\mathrm{Na}} \sim 1$[28,29].

In each simulation, a box containing a 32 nm water slab and a membrane of 4×4 pores are used, with a 16-nm water slab on each side (Fig. 6.5). Periodic boundary conditions are applied in the two directions parallel to the membrane (x & y) and fixed walls are placed at the ends of the simulation box along the z direction to confine the ions in the box. Before the actual ion diffusion simulation, each simulation box is equilibrated for 50 ns at 300 K in the *NVT* (fixed number of atoms, *N*, fixed volume *V*, and fixed temperature, *T*) ensemble.

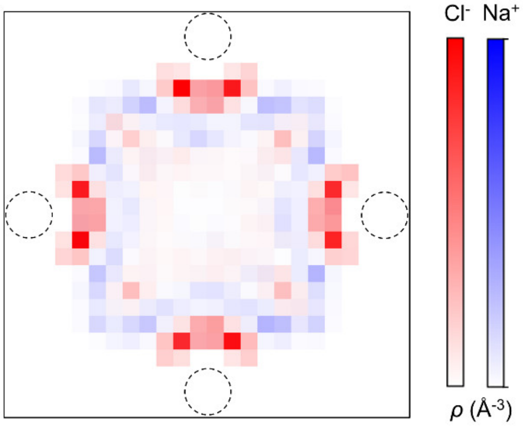

Figure 6.6 Cl^- (red) and Na^+ (blue) distribution within a single 2DNP (4-layer) nanopore calculated using CG-MD simulations. Center-to-center distance of edge carbon atoms is 2.25 nm, resulting in an open pore size of ∼1.9 nm. The dashed circles indicate the positions of –OH groups, and each pixel is 1×1 Å^2.

After ions diffuse across the membrane, we move the ions on the low-concentration side of the membrane back to the high-concentration side of the box, while keeping the ions within the membrane in place. This is to simulate the ion adsorption within the membrane and to rule out its contribution when counting the permeated ions. We then equilibrate the high-concentration side of the simulation box for 5 ns at 300 K in the *NVT* ensemble before we finally perform the actual ion transport simulations. To compute the number of permeated ions $N'(t)$, we run five independent repetitions of each simulation condition and count the numbers of Na^+ and Cl^- ions, $N'(t)$, that transport across the membrane every 1 ns for the first 25 ns. To avoid overcounting ions that are stabilized by the membrane, we exclude ions within 0.5 nm of the membrane. We normalized the number of permeated ions $N'(t)$ by the corresponding membrane area A.

Fig. 6.5 is a snapshot taken from a simulation run (at $t = 25$ ns) with parameters that closely represent our experiments ($D_{\mathrm{pore}} = 2.25$ nm, $n = 4$, $\theta_{\mathrm{Cl}} = 1.3$). High concentration of NaCl ($C_{\mathrm{H}} =$ 3 M) was introduced from one side to diffuse across the membrane to pure water, and the total number of permeated ions N' (normalized by the membrane area) was recorded as a function of time t. Fig. 6.5 (inset) plots $N'(t)$ for Na^+ and Cl^- up to t = 25 ns. N'_{Na} is larger than N'_{Cl}

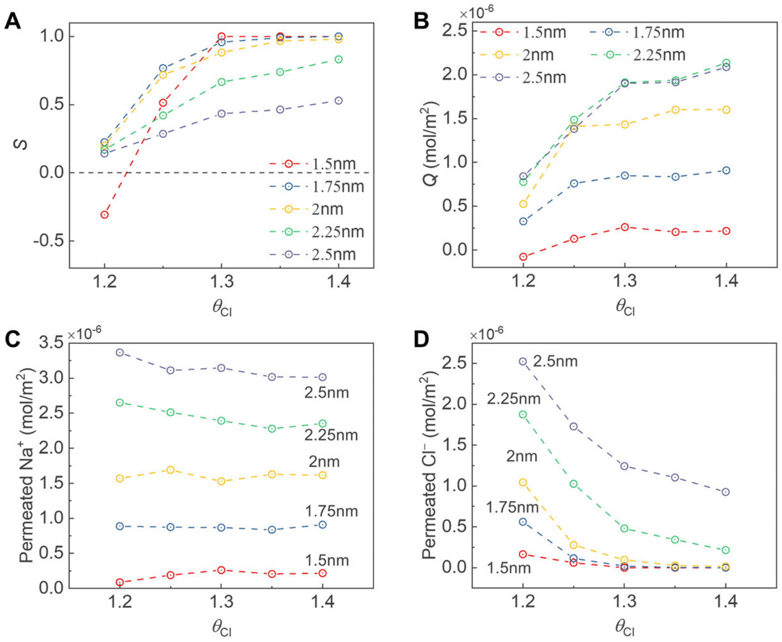

Figure 6.7 Simulated NaCl transport as a function of θ_{Cl}. (**A**) S, (**B**) Q, (**C**) permeated Na^+, and (**D**) permeated Cl^- as a function of θ_{Cl} with different D_{pore}.

throughout the simulation with the Na$^+$/Cl$^-$ flux ratio ~ 5 (the individual flux for Na$^+$ and Cl$^-$ is obtained by linear fitting of the $N'(t) - t$ data points). This ratio corresponds to a $S \sim 0.7$, a value similar to our experimental values (Fig. 5.18). In addition, the preferential binding of Cl$^-$ to -OH is clearly shown in our CG-MD simulations. Fig. 6.6 plots the density distribution of Na$^+$ (blue color) and Cl$^-$ (red) during the diffusion process across a membrane with the same parameters as in Fig. 6.5, where the position of -OH is indicated by the dotted circles. The ion density is averaged from all the pores in the membrane. Clear patterns emerge: while Cl$^-$ is strongly localized near the -OH groups, Na$^+$ stays away from the -OH. This indicates a preferential binding of Cl$^-$ to the -OH groups, which is a key to enable selective transport of Na$^+$ over Cl$^-$.

While the actual permselective process may involve complicated effects such as the rearrangement of the hydration structure, our results suggest that the relative binding strength θ_{ion} was the dominant factor in our tested conditions with both the polarity (i.e., cation-selectivity) and the magnitude of the permselectivity from the 2DNP experiments reproduced by our simulations. However, as the pore sizes enter the sub-nanometer regime, we expect the hydration structure become much more important and must be considered for an accurate description.

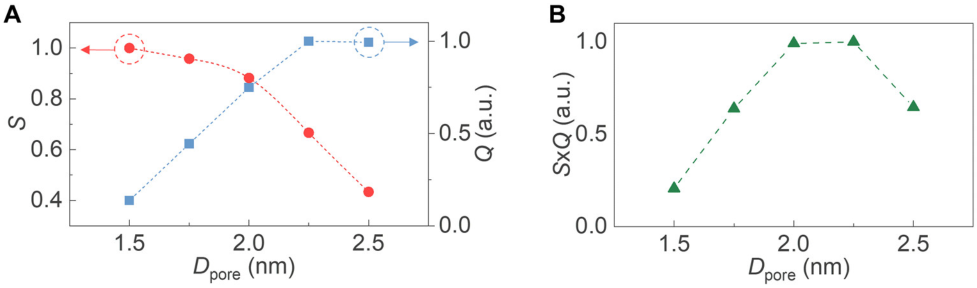

Figure 6.8 The influence of D_{pore} on permselective ion transport and osmotic power generation. (**A**) S and Q as a function of D_{pore} ($\theta_{Cl} = 1.3$ and $\theta_{Na} = 0.8$). (**B**) Power output of the membrane (S × Q) as a function of D_{pore} ($\theta_{Cl} = 1.3$ and $\theta_{Na} = 0.8$).

In addition to S (which is proportional to the generated osmotic potential), the simulated N' is used to calculate Q, the net number of permeated charges (representing osmotic current). Studying how they change with D_{pore} or θ_{Cl} will quantify these parameters' effects on the osmotic power performance (proportional to $S \times Q$). First, our simulations show that, as θ_{Cl} is gradually reduced from 1.4 to 1.2, both S and Q decrease rapidly leading to vanishing osmotic power generation (Fig. 6.7). This demonstrates the dominant role of the short-range -OH-Cl^- interaction for high power generation. Second, as D_{pore}, increases from 1.5nm to 2.5nm, S continuously decreases (red points, Fig. 6.8A). Q, on the other hand, initially increases but saturates at larger D_{pore} (blue points, Fig. 6.8A), even though individual fluxes of Na^+ and Cl^- continue to go up (see more data in Fig. 6.9 simulated with different theta values). This shows that there exists a narrow range for D_{pore} where both S and Q remain high for osmotic power generation, as confirmed by the plot of $S \times Q$ in Fig. 6.8B. Below this range, D_{pore} is too small and

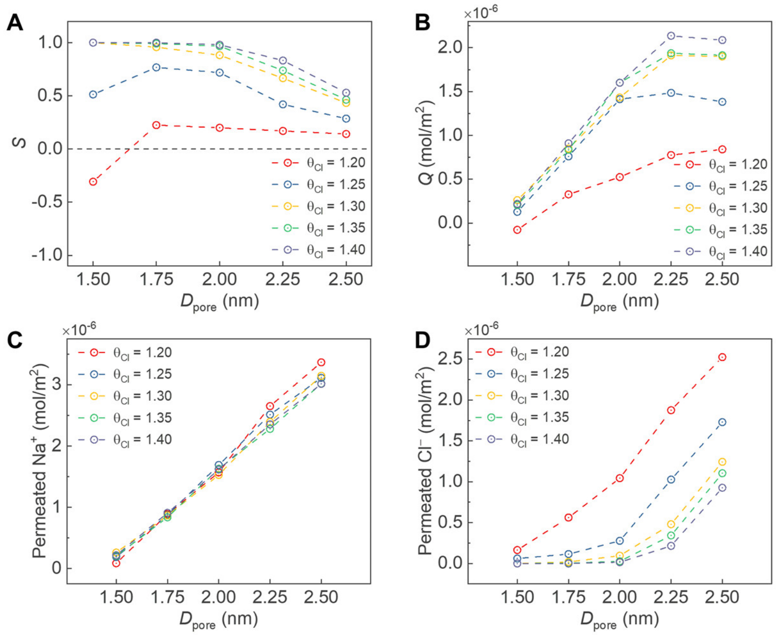

Figure 6.9 Simulated NaCl transport as a function of D_{pore}. (**A**) S, (**B**) Q, (**C**) permeated Na^+, and (**D**) permeated Cl^- as a function of D_{pore} with different θ_{Cl}.

the steric hindrance of the pore significantly blocks ionic transport leading to a small *Q* (Fig. 6.10B, bottom); above this range, the short-range effect of -OH-Cl⁻ binding is too much diluted leading to a small *S* (Fig. 6.10B, top).

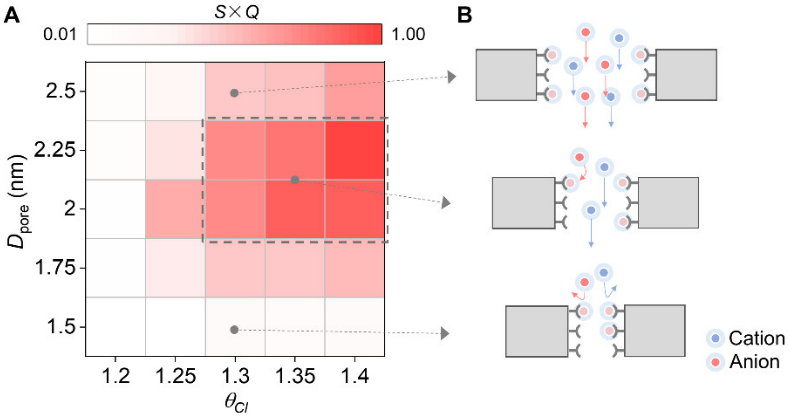

Figure 6.10 Goldilocks membrane parameters. (**A**) Heatmap of S × Q for various combinations of θ_{Cl} and D_{pore}. (**B**) Schematics for ion transport at different pore sizes.

To maximize the osmotic power output from a membrane, it is essential to find a molecular design by employing an approach that systematically balances the steric hindrance and the short-range interactions. Our CG-MD simulations provide a powerful tool for identifying such designs. Fig. 6.10A shows a 2D map of $S{\times}Q$ simulated as a function of θ_{Cl} (x-axis) and D_{pore} (y-axis), where we find the maximum $D_{\mathrm{pore}} = 2.25$ nm, $\theta_{\mathrm{Cl}} = 1.4$. In addition, it identifies a region of parameters (dashed boundary) with high expected power (> 70% of maximum), which can be considered a “Goldilocks zone”. The power generation is efficient only for a very narrow range (~ 0.5 nm) of D_{pore} and for θ_{Cl} larger than 1.2. While larger θ_{Cl} is preferred in general (Fig. 6.7), the optimal value of D_{pore} slightly changes for each θ_{Cl}. Our simulations are consistent with several recent experimental results on membranes of similar structures[17,30,31], and confirm that the parameters for our 2DNP membranes are found within the Goldilocks zone, which explains the giant osmotic power shown in Fig. 5.21. Significant permselectivity and osmotic power

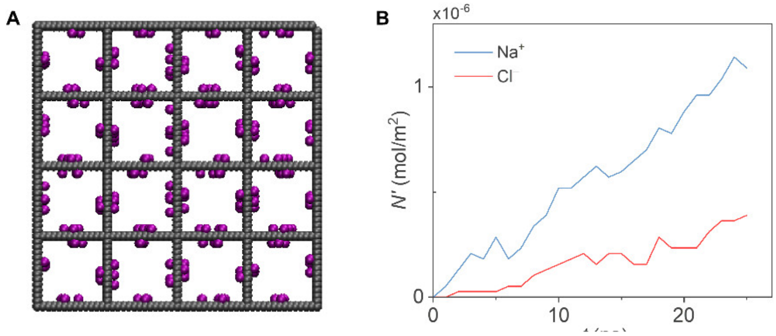

Figure 6.11 Simulated NaCl transport across a membrane with randomized -OH groups. (**A**) Top view of the simulated 4-layer membrane. D_{pore} of the membrane is 2 nm. (**B**) Permeation of Na^+ and Cl^- across the membrane from simulation.

generation were also observed in our simulations from a membrane with randomly positioned -OH groups (producing less long-range order), which indicates the generality of the short-range permselectivity (Fig. 6.11).

Although our MD simulation and experimental realization are based on specific -OH-ion (K^+, Na^+, and Cl^-) interactions, the same paradigm can be applied to different functional groups (such as $-NH_2$ and >C=O) and ionic species to realize desired permselective ion transport in a wide range of systems (e.g., halogen salts, nitrate salts, and sulfate salts). This signifies the critical role of precise molecular design for high performance osmotic power generation as well as other membrane applications based on effective short-range interactions.

6.4 Ion-Specific Selectivity and Gated Osmotic Power Generation

A fundamental difference between short-range interaction-based permselectivity and Coulomb screening is that the pairwise short-range interaction selects ions (as well as other permeates) through the relative binding strength instead of charge polarity. While this may not necessarily beneficial to osmotic power generation, it opens opportunities to realize on-demand permeate selection through materials engineering. Furthermore, it allows the same membrane to achieve distinct functions in different application scenarios. For example, if we replace the monovalent cations (Li^+, Na^+, K^+) with other ions that interact with -OH more strongly than (or as equally as) Cl^-, the same 2DNP membrane could become anion-selective (or non-selective).

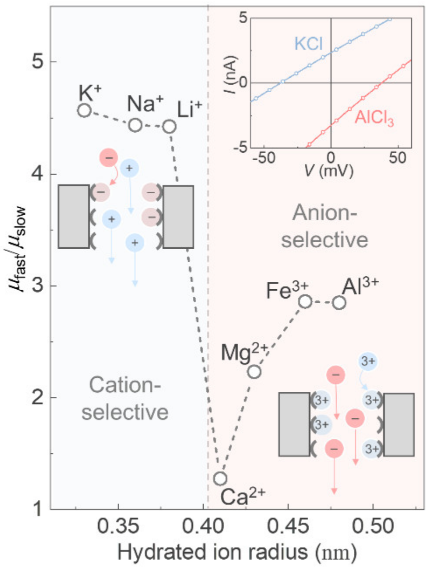

Figure 6.12 Mobility ratio μ_{fast}/μ_{slow} for different metal chloride salt solutions with monovalent and multivalent cations. Inset: schematic diagrams for cation- (left) and anion- (right) selective transport and representative I−V characteristics (top) for KCl and $AlCl_3$.

Such ion-specific selectivity is demonstrated in Fig. 6.12 using different metal chloride salts with cations of different elements, sizes, and charge states. First, the *I-V* curve taken from our 2DNP membrane with $AlCl_3$ (upper inset, Fig. 6.12; red curve) shows high osmotic power generation, but the polarity of the current and potential is reversed compared to that seen with KCl (blue), confirming the anion-selectivity when $AlCl_3$ is the permeate. This opposite permselectivity indicates stronger interaction between Al^{3+} and -OH than Cl^- and -OH. Figure 6.12 plots the ratio of ionic mobilities for the faster ions (μ_{fast}) and slower ions (μ_{slow}) in different metal chloride salts. The high cation-selectivity observed for monovalent cations (K^+, Na^+ and Li^+) flips to high anion (Cl^-) selectivity for multivalent cations (Mg^{2+}, Fe^{3+}, Al^{3+}), with Ca^{2+} producing nearly no selectivity. The polarity switching and the ambipolar operation are consistent with the increased binding energy expected between polar -OH and multivalent ions. This makes Mg^{2+}, Fe^{3+}, or Al^{3+} (not Cl^-) bind more strongly to -OH, freeing Cl^- to move faster for anion-selectivity (see schematics, Fig. 6.12).

Moreover, preferential binding to certain cations enables gated switching of osmotic current, where a small number of ions that strongly bind to -OH drastically alters the transport of other

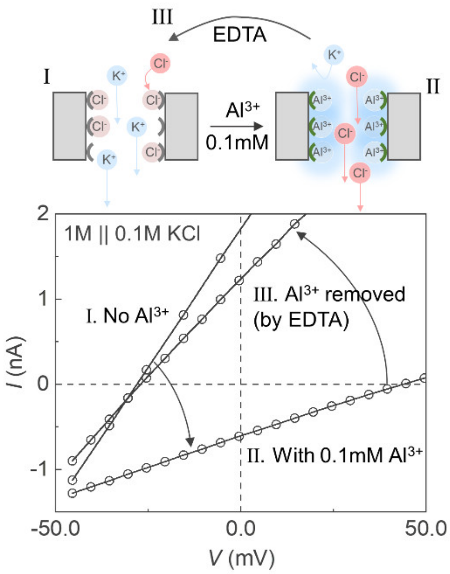

Figure 6.13 Al^{3+}-gated osmotic power generation. Schematics (top) and I−V characteristics (bottom) of Al^{3+}-gated transport for KCl across the 2DNP membrane.

ionic species, through the combination of steric and electrostatic interactions (see schematic in Fig. 6.13). For example, adding Al^{3+} at a low concentration to KCl solution can saturate the binding sites of the nanopores. While this enables both K^+ and Cl^- move freely without binding to -OH, the transport of Cl^- is preferred thanks to the Coulomb attraction between Cl^- and Al^{3+}. As a result, addition of 0.1 mM Al^{3+} to KCl solutions (1M || 0.1M) across a 2DNP membrane completely reverses the osmotic current and potential (I → II) even though KCl remains the predominant permeate. Moreover, the original *I-V* curve can be recovered if Al^{3+} is removed from the membrane. This is achieved by regenerating the membrane with EDTA, a strong multi-dentate binding agent that removes Al^{3+} from the membrane (II → III). As shown in Fig. 6.13, after soaking the membrane in EDTA solution for 30min, the *I-V* curve was almost recovered to that before the Al^{3+} exposure. This series of experiments demonstrate that our 2DNP membranes operating with short-range interactions can generate giant gateable osmotic power, which can be used for ionic logic devices and sensitive ion detection.

One major obstacle to studying and utilizing short-range interaction for permselective ion transport is that it is hard to isolate a specific short-range interaction from others. In our 2DNP, the porphyrin ring could also interact with metal ions in addition to the -OH group, which may influence the ion transport behavior. However, both previous reports and our experimental results suggest that the observed ion transport phenomena with multivalent cations in our 2DNP

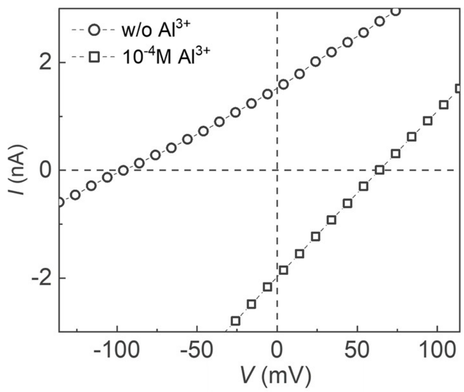

Figure 6.14 Al^{3+}-gated ion transport of KCl across the Ni(II)-TAPP-based 2DNP. The KCl concentration is 1M || 1mM.

is from the -OH – ion interaction rather than the porphyrin – ion interaction. According to previous reports, the metalation and demetallation of porphyrins usually occur at much harsher conditions (e.g., heat, strong acid/base, microwave, mechanical milling, etc.)[32–34] than our experimental conditions which were done at ambient temperature for relatively short time scale (~hrs). For instance, for porphyrin metalation with Al^{3+} ions, organoaluminium (III) reagents, water-free environment, and prolonged reaction time (hours to days) is usually required[32]. In contrast, the gating experiments in our Fig. 6.13 show that very small amount of Al^{3+} ions can have a significant effect on the ion transport in a relatively short time frame (~10 min). Moreover, the effect of Al^{3+} can be reversed by using EDTA. If the Al^{3+} were inserted into the porphyrin, the effect should be irreversible unless much harsher conditions were applied.

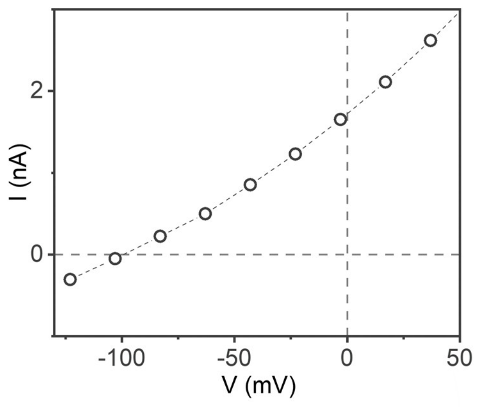

Figure 6.15 Osmotic power generation using KCl (Δ=1000) from a Co(III)-TAPP-based 2DNP membrane. The membrane diameter is ~370nm.

In addition, to investigate the effect of porphyrin metalation on the ion transport across our 2DNP membrane, we conduct two sets of experiments with 2DNPs based on Ni(II)-TAPP monomer and Co(III)-TAPP monomer, respectively. Figure 6.14 shows that the membrane synthesized with Ni(II)-TAPP displays similar gating behavior upon the addition of Al^{3+} despite the occupied porphyrin center. This suggests that the origin of the gating effect is independent of the presence of an open porphyrin center. Fig. 6.15 shows that Co(III)-TAPP membrane, where Co(III) has the same valency as Al^{3+}, displays a cation-selectivity – the same as that of the 2H-TAPP membrane. This indicates that insertion of multivalent ions into porphyrin rings does not induce the selectivity reversal observed with Al^{3+} gating experiment in Fig. 6.13.

Therefore, our experimental results strongly suggest that the observed ion-specific selectivity and gated osmotic power generation in the 2DNP are direct results of the -OH – ion interaction as intended by the molecular design. The successful isolation of the dominant interaction in our system allows us to systematically investigate the mechanism of short-range interaction-based permselectivity and form a systematic understanding that provides guidance for future membrane design.

6.5 Summary

In this chapter, we used CG-MD simulations to investigate the mechanism of the short-range interaction-based permselective ion transport, and experimentally demonstrated its unique applications in ion-specific selection and gated osmotic power generation. Using CG-MD simulation, we were able to capture the structural and chemical characteristics of our 2DNP with relatively small amount of computation power. We investigated a large range of parameters that interplay with each other to influence the ion transport. In our simulation, θ_{ion} was identified as an important parameter that determines the permselectivity of the membrane. In addition to θ_{ion}, the structural features of the membrane, such as pore size and thickness, also influence the transport behavior. The interplay between θ_{ion} and the structural parameters of the membrane defines a "Goldilocks zone" for optimal membrane performance, which should provide guidance for future membrane design. Thanks to the short-range interaction-based permselectivity, the 2DNP demonstrated ion-specific selectivity, whereas Coulomb screening only shows charge-specific selectivity. The chemical specificity allows the 2DNP membrane to achieve different polarities of permselectivity with different permeate, which is determined by the relative binding strength of the ionic species to -OH. Moreover, the strong binding between multivalent cations and the membrane also leads to gated osmotic power generation, where the extra charges introduced by the multivalent cations reverse the permselectivity and osmotic current. Such behavior is unique to short-range interaction-based permselective membranes and can be potentially applied to ionic logic devices and ion detections.

6.6 References

1. Aoki, T. Macromolecular design of permselective membranes. *Progress in Polymer Science (Oxford)* vol. 24 951–993 (1999).
2. Castro-Muñoz, R., Agrawal, K. V. & Coronas, J. Ultrathin permselective membranes: the latent way for efficient gas separation. *RSC Adv.* **10**, 12653–12670 (2020).
3. Sahu, S. & Zwolak, M. Colloquium : Ionic phenomena in nanoscale pores through 2D materials. *Rev. Mod. Phys.* **91**, 021004 (2019).
4. Liu, G., Jin, W. & Xu, N. Two-Dimensional-Material Membranes: A New Family of High-Performance Separation Membranes. *Angew. Chemie Int. Ed.* **55**, 13384–13397 (2016).
5. Siria, A. *et al.* Giant osmotic energy conversion measured in a single transmembrane boron nitride nanotube. *Nature* **494**, 455–458 (2013).
6. Feng, J. *et al.* Single-layer MoS2 nanopores as nanopower generators. *Nature* **536**, 197–200 (2016).
7. Wang, L., Wang, Z., Patel, S. K., Lin, S. & Elimelech, M. Nanopore-Based Power Generation from Salinity Gradient: Why It Is Not Viable. *ACS Nano* **15**, 4093–4107 (2021).
8. Li, H., Francisco, J. S. & Zeng, X. C. Unraveling the mechanism of selective ion transport in hydrophobic subnanometer channels. *Proc. Natl. Acad. Sci. U. S. A.* **112**, 10851–10856 (2015).
9. He, Z., Zhou, J., Lu, X. & Corry, B. Bioinspired Graphene Nanopores with Voltage-

Tunable Ion Selectivity for Na + and K +. *ACS Nano* **7**, 10148–10157 (2013).

10. Yu, T., Xu, Z., Liu, S., Liu, H. & Yang, X. Enhanced hydrophilicity and water-permeating of functionalized graphene-oxide nanopores: Molecular dynamics simulations. *J. Memb. Sci.* **550**, 510–517 (2018).

11. Zhu, Y. *et al.* Mg2+-Channel-Inspired Nanopores for Mg2+/Li+ Separation: The Effect of Coordination on the Ionic Hydration Microstructures. *Langmuir* **33**, 9201–9210 (2017).

12. Wang, Y., He, Z., Gupta, K. M., Shi, Q. & Lu, R. Molecular dynamics study on water desalination through functionalized nanoporous graphene. *Carbon N. Y.* **116**, 120–127 (2017).

13. Sint, K., Wang, B. & Král, P. Selective ion passage through functionalized graphene nanopores. *J. Am. Chem. Soc.* **130**, 16448–16449 (2008).

14. Shinde, D. B. *et al.* Crystalline 2D Covalent Organic Framework Membranes for High-Flux Organic Solvent Nanofiltration. *J. Am. Chem. Soc.* **140**, 14342–14349 (2018).

15. Corry, B. Mechanisms of selective ion transport and salt rejection in carbon nanostructures. *MRS Bull.* **42**, 306–310 (2017).

16. Liu, X. *et al.* Power generation by reverse electrodialysis in a single-layer nanoporous membrane made from core–rim polycyclic aromatic hydrocarbons. *Nat. Nanotechnol.* **15**, 307–312 (2020).

17. Yang, J. *et al.* Advancing osmotic power generation by covalent organic framework monolayer. *Nat. Nanotechnol.* **17**, 622–628 (2022).

18. Wang, H. *et al.* Blue Energy Conversion from Holey-Graphene-like Membranes with a High Density of Subnanometer Pores. *Nano Lett.* **20**, 8634–8639 (2020).

19. Secchi, E., Niguès, A., Jubin, L., Siria, A. & Bocquet, L. Scaling Behavior for Ionic Transport and its Fluctuations in Individual Carbon Nanotubes. *Phys. Rev. Lett.* **116**, 154501 (2016).

20. Cao, L. *et al.* On the Origin of Ion Selectivity in Ultrathin Nanopores: Insights for Membrane-Scale Osmotic Energy Conversion. *Adv. Funct. Mater.* **28**, 1804189 (2018).

21. Hille, B., Armstrong, C. M. & MacKinnon, R. Ion channels: From idea to reality. *Nature Medicine* vol. 5 1105–1109 (1999).

22. MacKinnon, R. Potassium channels and the atomic basis of selective ion conduction (nobel lecture). *Angewandte Chemie - International Edition* vol. 43 4265–4277 (2004).

23. Demille, R. C. & Molinero, V. Coarse-grained ions without charges: Reproducing the solvation structure of NaCl in water using short-ranged potentials. *J. Chem. Phys.* **131**, 034107 (2009).

24. Molinero, V. & Moore, E. B. Water modeled as an intermediate element between carbon and silicon. *J. Phys. Chem. B* **113**, 4008–4016 (2009).

25. Plimpton, S. Fast parallel algorithms for short-range molecular dynamics. *J. Comput. Phys.* **117**, 1–19 (1995).

26. Jorgensen, W. L., Madura, J. D. & Swenson, C. J. Optimized Intermolecular Potential Functions for Liquid Hydrocarbons. *J. Am. Chem. Soc.* **106**, 6638–6646 (1984).

27. Qiu, Y. & Molinero, V. Morphology of Liquid-Liquid Phase Separated Aerosols. *J. Am. Chem. Soc.* **137**, 10642–10651 (2015).

28. Yamdagni, R. & Kebarle, P. Hydrogen-bonding energies to negative ions from gas-phase measurements of ionic equilibriums. *J. Am. Chem. Soc.* **93**, 7139–7143 (1971).

29. Dunbar, R. C. Metal cation binding to phenol: DFT comparison of the competing sites. *J. Phys. Chem. A* **106**, 7328–7337 (2002).

30. Zhang, Z. *et al.* Cation-selective two-dimensional polyimine membranes for high-performance osmotic energy conversion. *Nat. Commun.* **13**, 1–9 (2022).

31. Huang, Z. *et al.* Essence of the Enhanced Osmotic Energy Conversion in a Covalent Organic Framework Monolayer. *ACS Nano* **18**, 16 (2022).

32. Zarrabi, N. & Poddutoori, P. K. Aluminum(III) porphyrin: A unique building block for artificial photosynthetic systems. *Coord. Chem. Rev.* **429**, 213561 (2021).

33. Harriman, A. & Osborne, A. D. Luminescence of porphrins and metalloporphyrins. Part 6.—Luminescence of aluminium(III) tetraphenylporphine and its μ-oxo dimer. *J. Chem. Soc. Faraday Trans. 1 Phys. Chem. Condens. Phases* **79**, 765–772 (1983).

34. Wang, J. *et al.* Morphology-Controlled Synthesis and Metalation of Porphyrin Nanoparticles with Enhanced Photocatalytic Performance. *Nano Lett.* **16**, 6523–6528 (2016).

Chapter 7: Ongoing Experiments and Future Directions

7.1 Introduction

So far in this dissertation, we have demonstrated the wafer-scale synthesis of monolayer 2DPs using a novel interfacial method – LAP, the layer-by-layer integration of 2DP/MoS_2 superlattices and their device application, and finally the design and application of 2DNP for osmotic power generation through short-range interactions. While all those are exciting progresses in the field of 2DP synthesis and application, our methods still have some limitations raised in the beginning of this dissertation. Specifically, the chemical stability and crystallinity of 2DPs synthesized using LAP are limited by the room-temperature condition, and the full potential of chemical tunability of 2DP has not been demonstrate in our osmotic power generation experiments.

In this chapter, we will present our preliminary data on our attempts to solve the aforementioned problems and share our vision for the future development of 2DP synthesis and application.

7.2 Room temperature synthesis of chemically stable 2DPs

In 2DP synthesis, the linkage bonds usually follow the rule of "easy to form, easy to break", and formation of stable chemical bonds usually requires harsh synthetic conditions. While certain stable bonds can be formed at relatively mild conditions, such reactions usually lead to amorphous products due to the irreversibility of the bond formation. In 2017, Farha and coworkers developed a method to synthesize Zr-based MOFs at room temperature[1]. In this method, Zr acetate cluster is first synthesized at elevated temperature of 130°C, and then the Zr

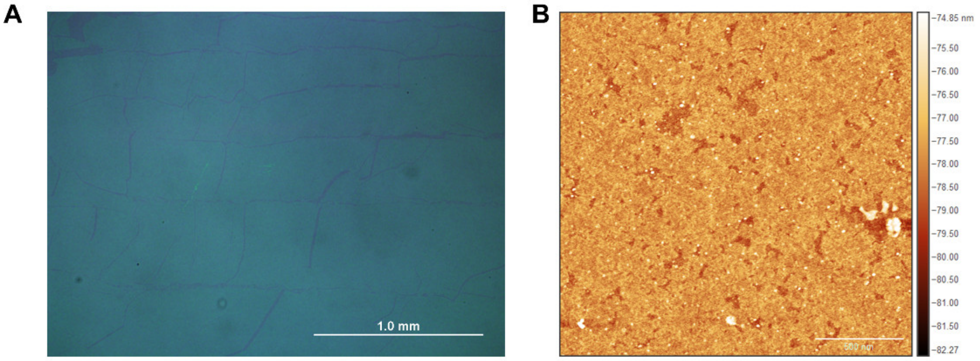

Figure 7.1 Inhomogeneity in LAP synthesized Zr-2DPs. (**A**) Optical image and (**B**) AFM image of transferred Zr-2DP on SiO_2/Si substrate.

MOF is synthesized at room temperature using the as-synthesized Zr acetate clusters and carboxylic organic linkers. Due to the defined coordination geometry of the Zr acetate cluster, the synthesized Zr-MOF demonstrates decent crystallinity despite the room temperature reaction condition.

Inspired by this method, we modified our LAP method and used it for the synthesis of chemically stable Zr-based 2DP. First, we use the reported method to synthesize the Zr acetate cluster using zirconium n-propoxide, $Zr(n\text{-}OPr)_4$ (70 wt% in n-propanol), in a DMF/acetic mixture (7:4 v/v). After heating at the 130°C for 2hrs, the solution changes from colorless to light yellow. For a typical LAP process, the amphiphilic monomer is spread at the pentane water interface, and the water-soluble linker is either pre-dissolved in the bottom phase or introduced to the water after the amphiphilic monomer assembly. However, Zr-based 2DP obtained with pre-dissolved Zr acetate cluster shows microscopic holes/cracks in the film, leading to inhomogeneity in the film (Fig. 7.1). This is likely due to the fast reaction kinetics between the Zr acetate cluster and the carboxylic monomer, as flakes/islands of Zr-based 2DP forming rapidly at the pentane-water interface would prevent the self-assembly of the fluidic amphiphilic carboxylic monomers.

To solve this problem, we lower the temperature by introducing ice in the bottom phase, and introduce the Zr acetate cluster after the monomer assembly. Since the Zr acetate is dissolved in DMF/acetic mixture, direct injection of the solution into the water phase would disturb the pentane interface as DMF and acetic acid have lower density than water and tend to float upwards. To prevent the disturbance of the interface, an inert barrier is placed above the bottom injection port and very slow injection of Zr acetate cluster solution is adopted (Fig. 7.2A). As shown in Fig. 7.2B, the quality of the Zr-based 2DP is greatly improved with the modifications.

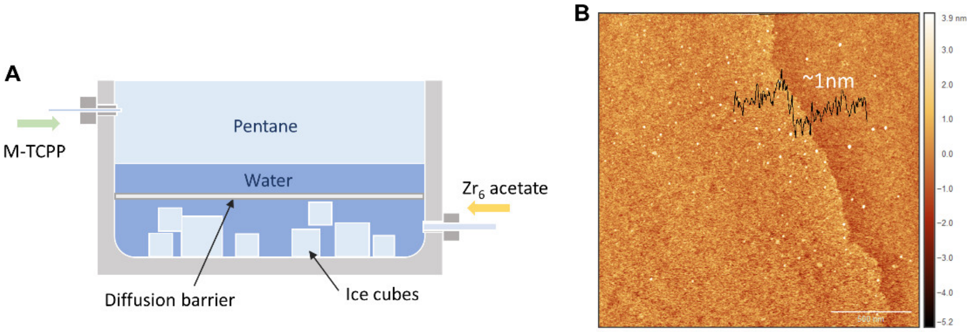

Figure 7.2 Modified LAP for Zr-2DP synthesis. (**A**) Schematic of the modified LAP process. (**B**) AFM image of Zr-2DP on SiO_2/Si substrate from the modified method.

The synthesis of chemically stable 2DP is necessary to take a full advantage of the chemical versatility of 2DPs. For instance, many catalysis and sensing processes need to take place in a relatively harsh chemical environment such as acidic/basic or high temperature. Therefore, making chemically stable 2DPs with LAP is a significant step towards the practical application of 2DPs in chemically complex/harsh environments.

7.3 Chemical vapor deposition of crystalline 2DPs

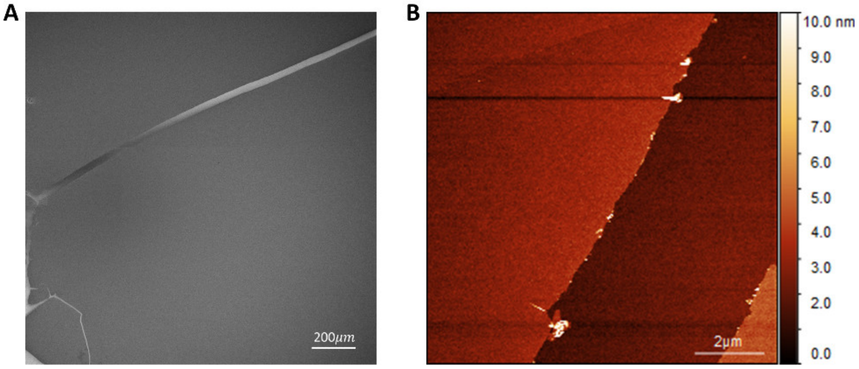

Figure 7.3 Morphology of Zr methacrylate cluster films. (**A**) SEM image and (**B**) AFM image of the Zr methacrylate cluster film on SiO_2/Si substrate.

While various techniques can be used to form chemically stable 2DPs with nanoscale or microscale crystallinity[1–3], so far, no methods can produce 2DPs with the same high quality as inorganic 2D materials synthesized using CVD techniques. Various research groups have attempted to use CVD or other gas phase deposition techniques to synthesize 2DPs[4–6]. However, due to the low thermal stability of the monomer and the products, the results from those methods are not satisfying.

We recently developed a method to synthesize monolayer 2DPs using a combination of a surface assembly and CVD, in the hopes for achieving better crystallinity for chemically stable 2DPs.

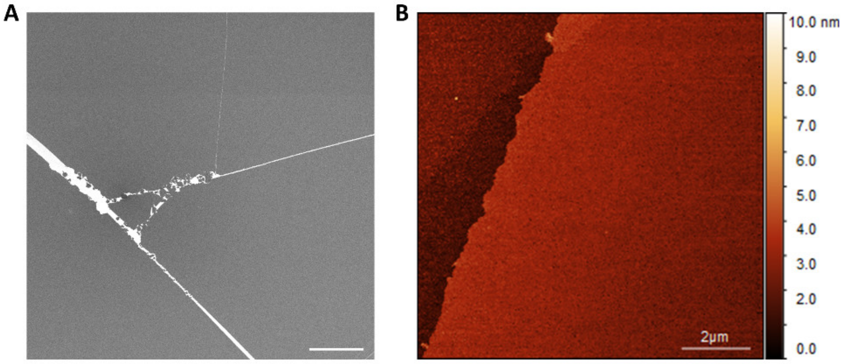

Figure 7.4 Morphology of CVD-synthesized Zr-2DPs. (**A**) SEM image and (**B**) AFM image of the Zr-2DP film on SiO_2/Si substrate.

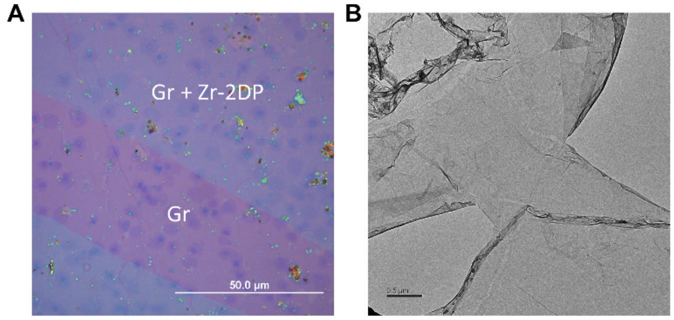

Figure 7.5 Zr-2DP grown on monolayer graphene through CVD. (**A**) Optical image of a Zr-2DP/graphene bilayer on SiO_2/Si substrate. (**B**) TEM image of suspended Zr-2DP/graphene bilayer.

The stable 2DP we choose to work on is Zr-based coordination 2DP as bulk Zr-based MOFs are among the most chemically stable organic framework materials. First, $Zr_6O_4(OH)_4(methacrylate)_{12}$ cluster is synthesized using Zr propoxide and methacrylic acid in n-propanol. Second, the hydrophobic cluster is then spread onto a water surface to form a densely packed monolayer. Finally, the cluster monolayer is transferred onto a substrate and placed in a CVD chamber with carboxylic monomer under vacuum.

The cluster film is uniform and shows a thickness of <2nm (Fig. 7.3), which provides a template for the CVD of the final 2DP. This method can be used to grow ultrathin 2DPs on various substrates including inorganic 2D materials such as graphene (Fig. 7.4 and Fig. 7.5), and various carboxylic monomers with different symmetries and wide range of molecular weight can be used for the growth. FTIR spectra of the cluster films and the product 2DP films clearly show signs of chemical reaction (Fig. 7.6). One major advantage of CVD compared to LAP and various solution-based techniques is that it allows a much higher reaction temperature which can potentially improve the crystallinity of the products. Fig. 7.5 shows a TEM

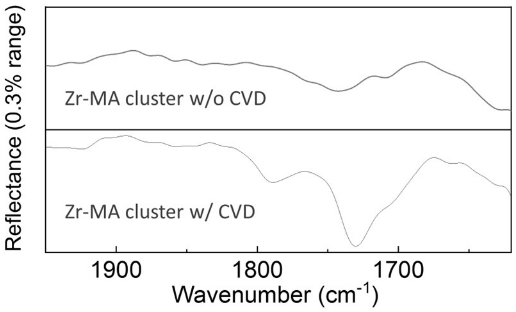

Figure 7.6 FTIR spectra of Zr-methacrylate cluster films and CVD-synthesized Zr-2DPs. The data were collected from samples on Au films using a grazing-incidence reflection geometry.

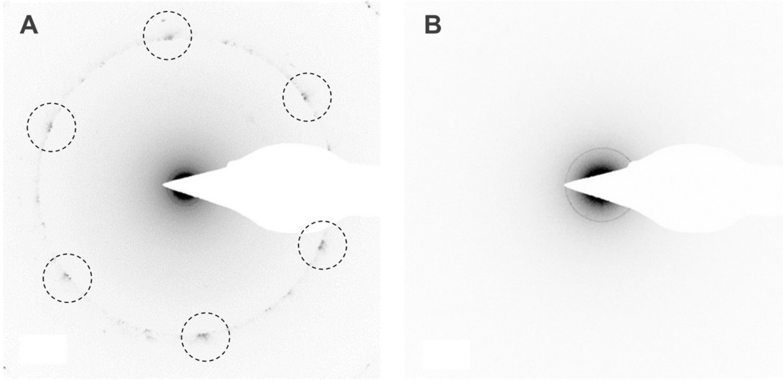

Figure 7.7 SAED patterns of a Zr-2DP/graphene bilayer. (**A**) Low magnification and (**B**) high magnification of the SAED pattern. The circled spots are attributed to the first order diffraction spots of monolayer graphene and are used to calibrate the measurement.

image of a Zr-2DP/graphene bilayer and its SAED pattern is shown in Fig. 7.7. The discrete dots are attributed to graphene, while the polycrystalline rings are consistent with the prediction for the Zr-2DP[7].

While the Zr-2DP synthesized using our current CVD approach only shows nanoscale crystallinity, we expect the combination of pre-assembly and high temperature gas phase synthesis can provide a great opportunity for high quality 2DPs, as it can operate at the thermal limit of all components in the reaction with controlled morphology through the templation.

7.4 Fluorescent 2DPs for sensing and sensitizations

The all-surface 2D structure and the nearly infinite chemical and structural tunability make 2DPs an ideal candidate for on-demand sensing of various chemicals and stimuli. Among all sensing methods, fluorescence sensing is arguably the most straightforward and effective one as it generally requires no complex device structure or readout instruments. Using the modified LAP discussed in

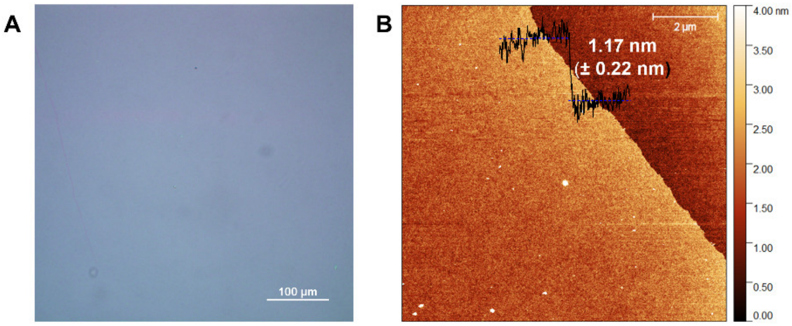

Figure 7.8 Zr-2DP with AIE molecular precursor synthesized through modified LAP. (**A**) Optical image and (**B**) AFM image of the AIE-Zr-2DP film. Inset: AFM line profile across the film edge.

section 7.2, we are able to synthesize Zr-based 2DP with aggregation-induced emission (AIE) monomers. The synthesized 2DP exhibits large-scale homogeneity and monolayer thickness (Fig. 7.8) just as in other 2DPs synthesized using LAP, while it shows a high photoluminescence quantum yield of ~37% (Fig. 7.9). Note that the AIE monomer used here is 4',4''',4''''',4'''''''-(Ethene-1,1,2,2-tetrayl)tetrakis(([1,1'-biphenyl]-4-carboxylic acid)) (TBPE), which does not self-assemble well at the pentane water interface by itself, likely due to the reduced hydrophobicity of the core. However, by increasing the acidity of the water phase, which inhibits the protonation of the carboxylic acid, the TBPE can be successfully spread at the pentane water interface. This produces a large-scale homogeneous film without comprising its quality.

The synthesized film shows a broad photoluminescence peak centered at ~525 nm with 350 nm excitation (Fig. 7.9), which is similar to that of the monomer TBPE. Fig. 7.10 shows that the fluorescence of the 2DP film decreases with increased water content in DMF. After the water is fully removed by vacuum annealing, the fluorescence of the 2DP film completely recovers, indicating its stability.

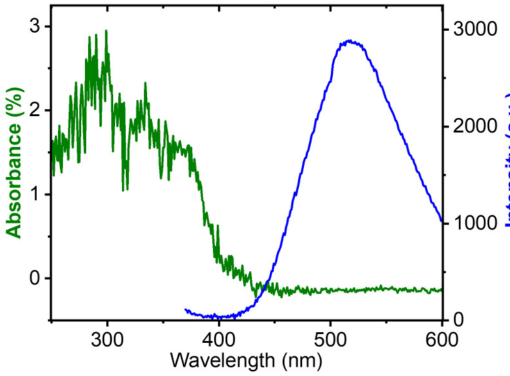

Figure 7.9 Absorption and emission of the AIE-Zr-2DP. Green: UV-Vis absorbance (%) of the AIE-Zr-2DP film on fused silica. Blue: Photoluminescence spectrum of the AIE-Zr-2DP film on fused silica. The film was excited at 350 nm.

While it is not clear why and how the 2DP fluorescence responds to the water content at this point, it suggests that the fluorescence response of the 2DP can be tuned by its chemical composition and structure. With systematic investigation of the parameters contributing to the fluorescence response in 2DP, we should eventually develop a detailed understanding of the response mechanism and realize on-demand sensing for target stimuli through rational molecular design. In addition to fluorescence sensing, the charge separation and exitonic process in fluorescent 2DPs can be utilized to sensitize otherwise inert electronic channels, such as MoS_2 and graphene, leading to responsive smart circuits.

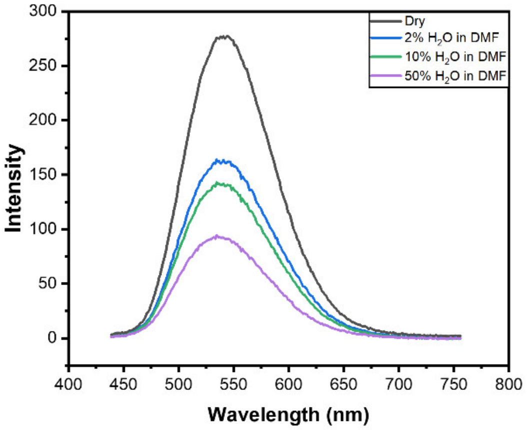

Figure 7.10 Fluorescence response of AIE-Zr-2DP to water content in DMF.

7.5 Summary

This is the last chapter of this dissertation, and we shift our discussion from achieved results to ongoing and future endeavors. Despite many progresses, both from us and others in the 2DP field, the quality of synthesized 2DPs still have great room for improvement and most of their applications are still at the proof-of-concept stage. In this chapter, we first introduced our ongoing efforts towards the synthesis of chemically stable 2DP with mild conditions using LAP. This greatly broadens the accessible applications with 2DPs, with one important example being fluorescence sensing with AIE Zr-2DPs. We also proposed a novel growth method for highly crystalline 2DPs, which combines surface pre-assembly and conventional CVD. Although current results are not to our satisfaction yet, they may introduce a new strategy to everyone in the field. The field of 2DP has been rapidly growing for almost 20 years, and we believe it still has much to grow in the future with the collective efforts from many brilliant minds.

7.6 References

1. DeStefano, M. R., Islamoglu, T., Garibay, S. J., Hupp, J. T. & Farha, O. K. Room-Temperature Synthesis of UiO-66 and Thermal Modulation of Densities of Defect Sites.

Chem. Mater. **29**, 1357–1361 (2017).

2. Murray, D. J. *et al.* Large Area Synthesis of a Nanoporous Two-Dimensional Polymer at the Air/Water Interface. *J. Am. Chem. Soc.* **137**, 3450–3453 (2015).
3. Liu, K. *et al.* On-water surface synthesis of crystalline, few-layer two-dimensional polymers assisted by surfactant monolayers. *Nat. Chem.* **11**, 994–1000 (2019).
4. Giusto, P. *et al.* Shine Bright Like a Diamond: New Light on an Old Polymeric Semiconductor. *Adv. Mater.* **32**, 1908140 (2020).
5. Liu, R. *et al.* Chemical Vapor Deposition Growth of Linked Carbon Monolayers with Acetylenic Scaffoldings on Silver Foil. *Adv. Mater.* **29**, 1604665 (2017).
6. Toh, C. T. *et al.* Synthesis and properties of free-standing monolayer amorphous carbon. *Nature* **577**, 199–203 (2020).
7. Cao, L. *et al.* Self-Supporting Metal-Organic Layers as Single-Site Solid Catalysts. *Angew. Chemie - Int. Ed.* **55**, 4962–4966 (2016).